Title
Nanocrystal Surface Modifications for Catalytic Solar to Fuel Conversion

Author
Grauer, David

Publication Date
2014

Peer reviewed|Thesis/dissertation

Nanocrystal Surface Modifications for Catalytic Solar to Fuel Conversion

By

David Calder Grauer

A dissertation submitted in partial satisfaction of the

requirements for the degree of

Doctor of Philosophy

in

Chemistry

in the

Graduate Division

of the

University of California, Berkeley

Committee in Charge:

Professor A. Paul Alivisatos
Professor Jeffrey R. Long
Professor Andrew M. Minor

Fall 2014

Abstract

Nanocrystal Surface Modifications for Catalytic Solar to Fuel Conversion

By

David Calder Grauer

Doctor of Philosophy in Chemistry

University of California, Berkeley

Professor A. Paul Alivisatos, Chair

With their extremely high surface-to-volume ratios, nanocrystal surface morphologies, structures and compositions can have outsize effects on a nanoparticle's electronic, optical and catalytic properties when compared to their bulk system counterparts. Nanocrystal research has, in recent years, begun focusing on systematic characterization and manipulation of these surfaces for rational control of a nanocrystal's desired physical properties. The work presented in this dissertation provides further investigations of surface structure-function relationships with direct relationship to the catalytic and stability requirements of solar-to-fuel conversion systems.

In the first chapter, a brief and general review of quantum dot structure-function relationships in solar energy conversion schemes will be presented with an emphasis on photoelectrochemical devices. A discussion of general methods in nanoparticle synthesis and surface modification will be followed by a more in-depth analysis of the key physical principles of quantum dot (QD) photoelectrochemical and photocatalytic device architectures. Much of that discussion will concentrate on controlling the kinetics of a series of interfacial electron transfers. Finally, a review of methods in solar-to-fuel conversion chemistry will be presented with an emphasis on integrated water splitting devices, architectures employing an intimate semiconductor-catalyst-liquid or a semiconductor-metal oxide-liquid junction. This discussion will focus on the protection methods developed in the past four decades to combat destructive photocorrosion reactions.

The second chapter will present research directed at catalytic modifications to and structural characterizations of colloidal QDs. The goal of this project was to photocatalytically reduce protons from water using a nanocrystal light harvester and a surface bound, proton-reducing electrocatalyst. While we found that a covalently linked, homogeneous molybdenum-oxo electrocatalyst was photocatalytically inert, the decomposition product, identified as a structural relative of amorphous molybdenum trisulfide, was found to be highly active for photocatalytic proton reduction. X-ray absorption and photoemission structural characterizations of the amorphous catalyst before and after photocatalysis have been included. We found that the parent MoS_3 structure identified before catalysis evolves into a relatively undercoordinated Mo-S bonding geometry: bridging disulfide linkages are converted into dative sulfides. This structure

opens up the sulfide for ready protonation as a possible intermediate during catalysis. Such protonation is not available to the disulfide-containing derivative. The morphological conversion to an undercoordinated metal-ligand center is often invoked in catalyst activities, but rarely structurally identified.

The third chapter presents a study of ligand effects on charge transfer kinetics in a model system, $W_{18}O_{49}$ ($WO_{2.72}$) nanoparticles. Tungsten oxide phases derived from WO_3 are numerous due to the stability of the system even with high concentrations of oxygen vacancies. These vacancies result in significant electron density in the material's conduction band with the material class undergoing a metal-semiconductor transition at stoichiometries around $WO_{2.8}$. These nanoparticles were synthesized with a moderately strongly bound ligand shell based on alkylamines. We found that when exposed to a sphectrophotometric redox indicator, namely an iron(III) tris-phenanthroline derivative, we could track the oxidation of electrons out of the nanoparticle conduction band, and into solution via the visible signal from the reduced iron complex. With that tag, we sought to investigate how the ligand affects the charge transfer rates. Hypothesizing that one of two mechanisms were in effect – outer sphere (tunneling) and inner sphere (dissociative) – we synthesized nanoparticles with varying ligand lengths in their shells and ran ligand concentration dependence studies. We found no correlation between ligand length and charge transfer rate, but a strong dependence of the rate on the concentration of free alkylamines in solution appeared. From this observation, we conclude that charge transfer occurs through uncoordinated surface sites whose concentration is dictated by parameters in surface binding isotherms, i.e. ligand binding coefficients, temperature and ligand-ligand interactions.

The fourth and final chapter will focus on photoelectrochemical water splitting employing a QD sensitized mesoporous titania thin film. To protect these light absorbers, a crosslinkable ligand was synthesized to passivate the vast majority of surface sites, thereby restricting the loci of charge transfer to accessible unbound sites. At these unbound sites, a water oxidation catalyst was deposited as a hole acceptor. Crosslinking was hypothesized to serve to reduce the native ligand's fluxionality on, off and over the surface of the QD by the chelate effect. In this hypothesis, ligand movement liberates new semiconductor surface sites to the corrosive aqueous environment. This can be tested by employing a ligand designed to react with nearest neighbors, suppressing ligand motion and desorption. Key characterization of the proposed architecture is presented via NMR, XPS and photoluminescent quenching studies. Photoelectrochemical testing indicates that the system does, in fact, produce oxygen, though at low current densities (~5 $\mu A/cm^2$) and less than 100% Faradaic efficiency. While eventually unstable, we make the argument that many of this system's benefits warrant further investigations – namely the solution processability of their production and the rationality of their protection. Such prospects are discussed in a brief outlook section in the concluding section of this final chapter.

Table of Contents

Chapter One – Semiconductor Nanocrystal Syntheses, Structure-Function Relationships and Photoelectrochemistry

1.1.1 Dimensional Confinement of Bulk Materials

Semiconductor nanocrystals are a material class that straddles the border between clusters and extended bulk solids. Importantly, they assume some, but not all of the features of their neighboring classes: like clusters they have a significant fraction of their atoms on their surface, and like extended solids, their internal atoms maintain a periodic, crystalline structure.[1,2] In addition, many of their electronic properties mirror both extended bulk electronic properties, such as band formation, as well as molecular hallmarks, such as discrete bonding and non-bonding orbitals near the conduction and valence band edges. Beginning in the early 1980's, these materials began attracting attention as a result of their size dependent optoelectronic properties. Perhaps the most apparent of these size effects was the apparent blue shifting of the optical band gap with decreasing particle size.

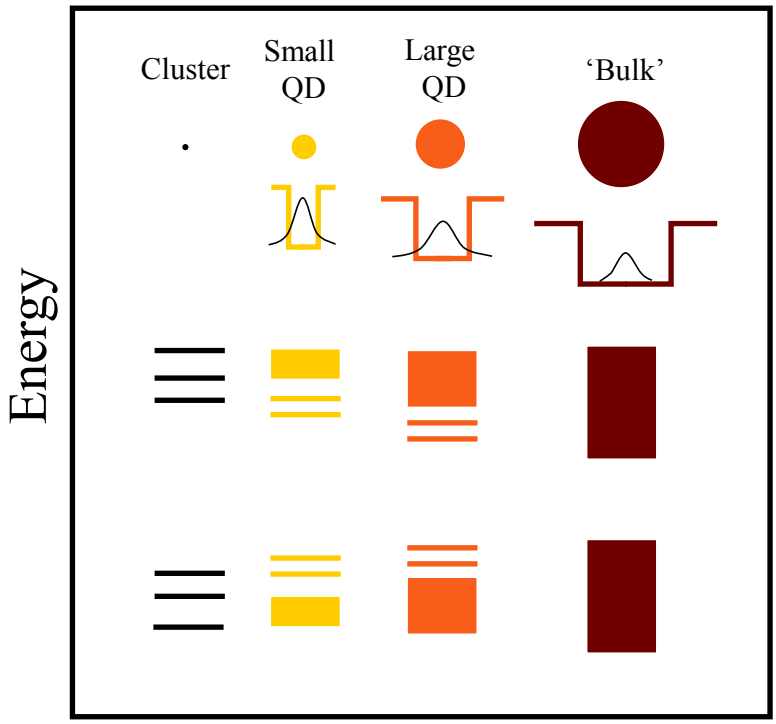

Figure 1.1 – Clusters exhibit electronic structures with discrete states. QDs show both discrete states at the band edges, which through coupling have come closer in energy and continuous bands. Additionally, since the bulk excitonic radii in these materials are larger than the QD radii, confinement increases the exciton wavefunction energies and extends their probabilities beyond into the particle boundary (shown schematically below the particles). In the bulk, the excitonic radius is much smaller than the material so the surface has no influence on the wavefunction's energy or probability density. Both confinement and orbital de-mixing contribute the observed blueshift in bandgap energy with decreasing particle size.

While some size-effects can be explained from a bonding perspective, such as orbital de-mixing, the most intriguing effects arise from particle spatial confinement.[3] As a particle's size approaches the same length scale as its exciton wavefunction (typically between 1 and 10 nm), the surface begins imposing itself on the state's probability density distribution and energy. This imposition can be described as the non-infinite potential barrier of the canonical particle-in-a-box model (**Figure 1.1**) One can qualitatively think of a particle's shrinking size as a decrease in the width of the 'box' that the particle's excitons see. As a result, the exciton states increase in energy when the box width decreases, and thus the bandgap widens.[4,5,6] Additionally, as the surface behaves as a non-infinite potential barrier, electronic states have significant portions of their probability density extending beyond the wall. This wavefunction extension increases with decreasing particle size ('box' narrowing) and surface energy lowering through different surface passivation types (barrier lowering). Such optoelectronic size-effects have garnered enormous interest in the past three decades.[3,7,8] These quantum mechanically induced size effects have generated the colloquial name for semiconductor nanocrystals, quantum dots, or QDs.

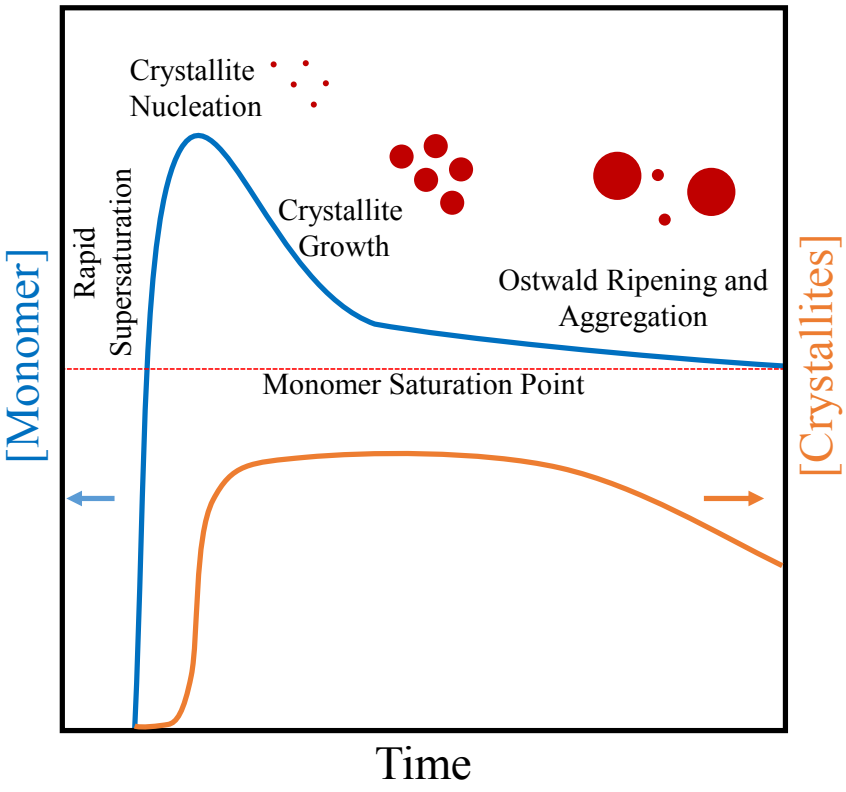

Figure 1.2 – Crystallite nucleation and growth as described by Dinegar and La Mer. A solution becomes rapidly supersaturated in monomer and nucleation of clusters begins. These clusters begin to grow isotropically and consume monomer from solution, depleting the solution. As the solution monomer concentration approaches the saturation point, crystallites begin ripening and aggregating in order to lower their surface energies. Aggregation will lead to a decrease in the number of crystallites

1.1.2 General Principles of Semiconductor Nanoparticle Synthesis

Current methods for the preparation of colloidal QDs have grown out of Michael Steigerwald's work on organically passivated CdSe nanocrystal clusters.[9] His work built off arrested precipitation methods which could yield poorly crystalline, nanoscaled colloids whose sizes and distributions were predicted by Dinnegar and La Mer Theory (**Figure 1.2**).[3,10] Steigerwald made the important step of chemically derivatizing the particle surface with strongly bound ligands as opposed to the weaker surface interactions which had been used previously. Due to their strong surface interactions, these strongly bound ligands, such as alkylphosphonates, alkylcarboxylates, thiolates and alkylamines, provided a route to far better crystallinity as they could kinetically slow down the growth of the nanocrystals by blocking addition sites and sterically hindering aggregation, thus allowing growth temperatures to increase.[11] With these strongly coordinated surface ligands, solvent temperatures during QD growth could be increased above 350°C without runaway growth or aggregation of the precipitating crystallites. These high temperatures allowed far greater crystallinity with fewer defects; this crystallinity directly resulted in much longer excited state lifetimes which visibly manifested themselves as room temperature fluorescence in direct gap materials.

Most controlled QD syntheses still rely on the principles of arrested precipitation and have achieved monodisperse examples of numerous main group and transition metal semiconductor materials.[8] In arrested precipitation, the growth solvent is rapidly supersaturated with a species, for example CdSe clusters formed by reaction of Cd and Se precursor compounds, which nucleate into small crystallites and begin growing into larger crystals by addition of monomer CdSe clusters from solution. Growth is stopped by monomer dilution. In QD growth, rapid cooling both slows the monomer creation reaction, lowering solution monomer concentration and increases the surface binding coefficient of the ligand, slowing monomer addition. Arresting growth is necessary to achieve narrow nanoparticle size distributions, which would widen close to the monomer saturation point as the nanoparticles undergo Ostwald ripening and aggregation to reduce surface energies. Because it is the most developed and relevant to the work presented later in this dissertation, this chapter will focus on CdSe QDs.

1.1.3 Core-Shell Nanoparticle Heterostructures for Charge Carrier Recombination Control

While increasing growth temperatures and ligand binding energies increased CdSe QD fluorescence by decreasing internal defect densities, surface defects were still limiting fluorescence quantum yields to roughly 10% by acting as sites for non-radiative recombination. The late 1990's saw the advent of 'shelling' reactions where wide bandgap semiconductors, such as ZnS and CdS, were used as surface coatings on CdSe QDs to passivate core surface defects and confine the core exciton wavefunction to the internal structure, thus limiting its interaction with surface defects on the exterior shell.[12–14] By choosing appropriate shelling materials with crystal lattice parameters and structures that were similar to the cores', the shell could interface nearly epitaxially with the core QD. As they contain two or more materials, these structures have been called heterostructures. This epitaxial interface drastically reduced the number of the core's original surface defects by forming strong bonds with the shelling material. Again invoking the particle-in-a-box framework, the wide gap materials functioned as non-infinite potential wells, intermediate in height between the ligand/solvent and the core. The core exciton

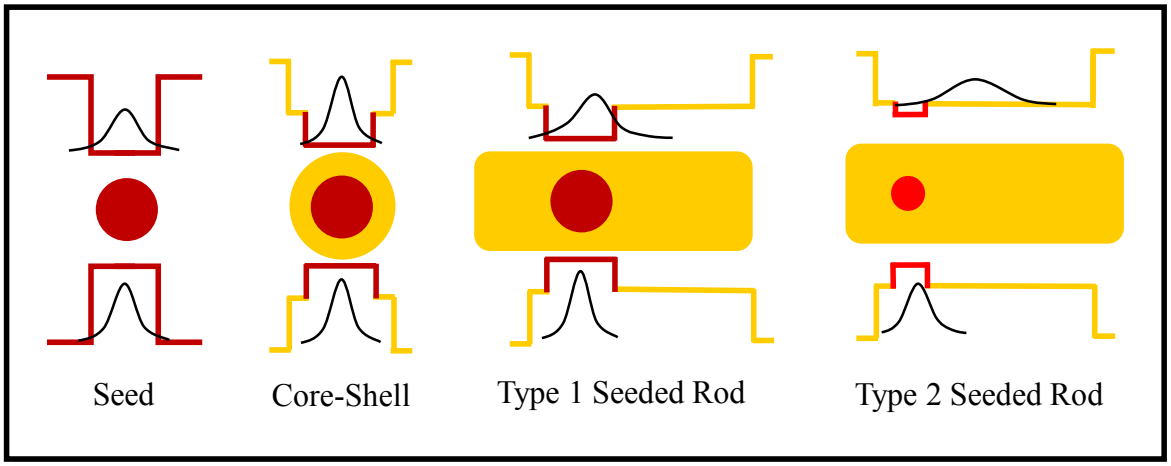

was therefore confined internally, interacting slightly with the shell and negligibly with the surface (**Figure 1.3**). Using such methods, researchers can now achieve core-shell QD heterostructures with near unity fluorescent quantum yields.[15] This extremely high quantum yield is the direct result of a minimization of internal defects and shell-based exciton isolation from surface defects, which in tandem produce long-lived excited states.

Figure 1.3 – Electron (above) and hole (below) wavefunctions in various CdSe QD structures and heterostructures. Without a CdS shell, the CdSe seed's wavefunction "sees" a large amount of the surface. By shelling the seed with a wide gap material, like CdS, the exciton's wavefunction becomes more confined to the internal structure and sees less of the surface defects. In a seeded rod, growth of the shell is directed axially with a phosphonic acid. In a type 1 structure, the seed is large, and its exciton's wavefunction is more localized to the seed. When the seed is smaller, the conduction band energy approaches the conduction band energy of the rod, and the electron begins to delocalize more over the rod. The valence band energy shift is less affected by quantum confinement and therefore the energy gap remains between the CdSe and CdS. As a result, the hole remains more localized to the seed. With the two charges in two materials, the structure is considered type 2.

1.2.1 Spatial Control of Charge Carriers

In addition to pure confinement, heterostructures also manipulate the individual probability densities of an exciton's two charges, electrons and holes, within a particle (**Figure 1.3**). Such differential probability density arises partially from the effective mass difference between electrons and hole, with holes typically being heavier than electrons.[5] As a result, again from a particle-in-a-box perspective, electrons tend to extend their probability densities further into the shell barrier than holes. In addition, the conduction and valence band (CB and VB) energy alignments of the wide-gap shell and narrow-gap core are not necessarily isotropic in energy. The difference in energy between the two materials' CBs and VBs will influence the probability densities of the electron and hole wavefunctions in a predictable manner; large differences between band energies will prevent extension; small barriers will promote extension. In the case when the electron and hole are localized in the same material, the structure is considered type-1. When the two charges are in two different materials or regions, the structure is considered type-2.

This differential delocalization is relatively small in core-shell particles where the shelling material often has little total volume, the situation is different when the shell becomes larger. Following the development of strongly coordinating ligands for particle growth, it was found that some of these ligands could also influence the different directions of crystal growth.[16] By binding different facets of CdSe or CdS with different energies and favoring certain growth directions, mixtures of alkylphosphonic acids could produce high aspect ratio nanoparticles with rod or tetrapod morphologies, among others. Such morphologies were rationalized by the strong surface binding of the phosphonates to the {110} planes of wurtzite CdSe. Strongly passivated {110} faces allowed for faster growth along the (100) and (001) faces which could produce the nanorod and nanotetrapod shapes. Wurtzite cores produce nanorods with wurtzite CdSe grown off the core's {001} faces, while the {111} faces of zincblende cores produced four arms of wurzite CdSe in the case of tetrapods. Growth off the various facets could be predicted by the symmetry of that plane's surface atoms; for example, the {111} planes of zincblende have hexagonal packing symmetry, like wurtzite's {001} facet. Work by Dimitri Talapin showed that such preferential growth mechanisms could translate to core-shell seeded growth reactions. If the shell was grown in the presence of these strongly coordinating ligand mixtures, the shell would assume the high aspect ratios observed in the un-cored, subsequently called seeded rods (from wurtzite seeds) and tetrapods (from zincblende seeds).[17,18] Interestingly, differential delocalization of the electrons and holes, i.e. type-II structures, could be readily observed in systems where the CdSe seed of a CdS nanorod was small enough that the two CB energies were similar.[19,20]

1.2.1 Photocatalysis and Photoelectrochemistry at Quantum Dot Interfaces

In photocatalysis (PC) and photoelectrochemistry (PEC), efficient light absorption and charge generation as well as rapid charge separation and transfer are critical to efficient energy conversion. QDs offer tantalizing possibilities in addressing many of these requirements. Their tunable bandgaps are quite suitable for broad spectrum light harvesting. More intriguingly, QD heterostructures such as core-shells and seeded nanorods can be engineered for lengthened exciton lifetimes and exciton wavefunction manipulation. Such engineering can enable spatial control of charge transfer.[21,22] Control of both electron and hole transfer is necessary if QDs are to be used in realistic fuel forming reactions so that corrosion reactions can be averted and fuel forming reactions targeted.

1.2.2 Foundations of Charge Transfer in Nanoparticle Systems

QD interfaces involved in PEC and PC are complex and dynamic semiconductor-ligand-solution/redox mediator interfaces. When charges pass through them, each part influences the observed rates. At their hearts, though, these processes are still charge transfer reactions between donors and acceptors, and traditional electron transfer theory, or Marcus Theory, provides a powerful foundation for understanding them.[23] The relevant derivations are given elsewhere, but the fundamental relation (**Eq. 1**) between activation energy, $\Delta G^{\ddagger}$, to the reaction free energy, ΔG_{rxn}, and the reorganization energy, λ_o, the energy required for all the reaction's nuclei to move from their initial to final coordinates without charge transfer occurring, is shown below:

$$\textbf{Eq. 1} \quad \Delta G^{\ddagger} = \frac{(\lambda_o + \Delta G^{\circ})^2}{4\lambda_o}$$

When combined with the Arrhenius equation and a donor (*A*) acceptor (*B*) electronic coupling integral, H_{AB}, one arrives at the famous Marcus equation (**Eq. 2**) governing the rate of electron transfer, k_{et}:

$$\textbf{Eq. 2} \quad k_{et} = \frac{2\pi}{\hbar} |H_{AB}|^2 \frac{1}{\sqrt{4\pi\lambda_o k_b T}} \mathrm{e}^{-\left(\frac{(\lambda_o + \Delta G^{\circ})^2}{4\lambda_o k_b T}\right)}$$

The Marcus equation correctly explains the observed increases in rate constants with increasing ΔG° in the normal regime and, importantly, predicts an 'inverted' regime when ΔG° becomes large enough to overwhelm the reorganization energy of the system, resulting in a decrease in rate constant with further increasing ΔG°.[24] Importantly, one can model electrochemical kinetics, or Faradaic current, at electrode interfaces by extending the Marcus equation with Butler-Vollmer kinetics.[25,26]

In QDs, the surface ligand affects charge transfer as it forms a barrier between the donor and acceptor. This ligand enforced separation appears in the Marcus equation as the electronic coupling integral, H_{AB}, and has been carefully studied electrochemically using self-assembled-monolayer electrodes and spectroscopically using rigidly linked donor-acceptor dyads during and since the 1980's. [27,28] This distance dependence (**Eq. 3**), as predicted by the tunneling probability density inside a non-infinite potential barrier, has an exponential dependence on spacer distance, *d*, with a transfer coefficient, β being a reflection of the chemical nature of that spacer or, in other words, the barrier height.

$$\textbf{Eq. 3} \quad k'_{et} = k^{o}_{et} e^{-\beta d}$$

1.2.3 QD Photocatalysis

In QD based photocatalysis, a QD photosensitizes one or two catalysts by providing electrons and or holes for reduction and oxidation reactions respectively.[29] The QD splits its exciton via separate, rapid electron and hole transfers to the catalyst(s) or some other solvated redox species, **Figure 1.4**. Typically, QDs are used in reductive photocatalysis, as they are not particularly oxidatively stable themselves. The QD-catalyst conjugations can have direct surface-catalyst interfaces, intermediate covalent or electrostatic linkages between the photosensitizing QD and the active site.[21,30,31] As one would expect from Marcus theory, the linkage has enormous effects on the observed charge transfer rates.[32] Direct interfaces provide far more rapid charge transfers than indirect linkages, such as covalent ligands. It is notable, however, the few QD photocatalysis studies isolate the ligand effects on the overall system's efficiency.[33] Work in Chapter 3 will seek to address some of the influences and will review the known effects in more detail.

With few exceptions, the QD photocatalysis literature has focused on proton reduction from water.[29] QD-photocatalyzed H_2 production has, to date, relied on sacrificial reductants to rapidly extract the photogenerated hole from the nanoparticle. Such an agent is necessary to avert both

energetically favorable aqueous photocorrosion reactions (described in more detail in section 1.3.4) and recombination with the electron in the particle or on the catalyst. With this sacrificial reagent, it is possible to isolate the forward electron transfer and study exciton splitting dynamics as well as catalyst structures. Research presented in Chapter 2 will use such an agent to isolate the MoS_3-like catalyst for structural characterization. A more comprehensive review of the QD photocatalysis literature can be found there.

If QDs are to find application in solar powered fuel production via water oxidation, or artificial photosynthesis, methods must be developed to avert photocorrosion reactions in renewable,

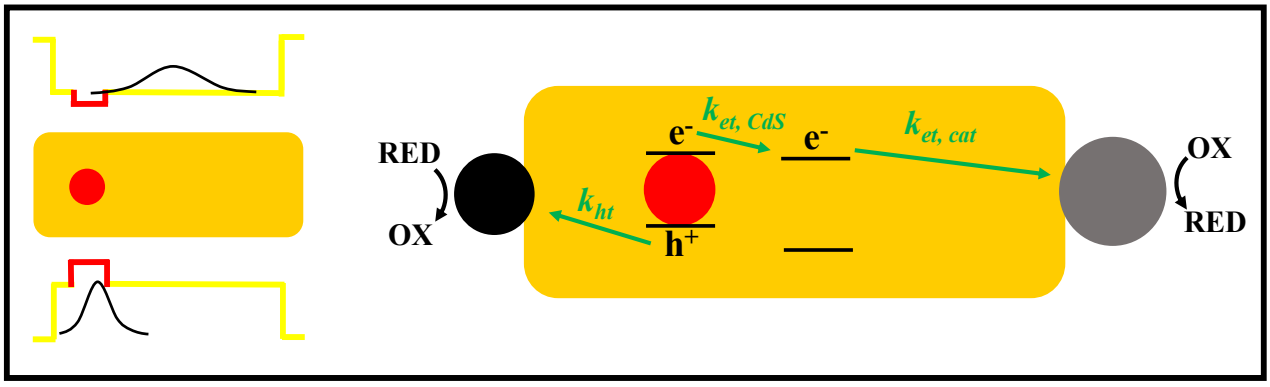

Figure 1.4 – A type 2 seeded rod in a photocatalysis architecture. A reduction catalyst has been placed near the electron wavefunction (left) and an oxidation catalyst near the hole's wavefunction. The design takes advantage of a nanoparticle's ability to preferentially localize and delocalize charges to catalyst areas. The electron delocalizes to the CdS rod following excitation very rapidly, ~1ps, then transfers to the reduction catalyst with k_{et}. The hole preferentially localizes to the seed, and transfers to the oxidation catalyst (black dot) with rate constant k_{ht}. Ideally, electron delocalization, electron transfer and hole transfers are all much faster than recombination.

energy storing methods. Few, if any, sacrificial, irreversible reductants satisfy this condition.

1.2.4 Basic Principles of Solution Junction Photoelectrochemistry

Solution junctions in photoelectrochemistry are broadly defined in the literature as semiconductor solution interfaces which impose a charge separating force on electrons and holes in the underlying semiconductor. **Figure 5** schematically walks through the concepts relevant to charge separation
and voltage creation in an open circuit (no net current) condition. An *n*-type semiconductor in the dark will have essentially flat band energies throughout the material. If the material is immersed into a solution with an equilibrium redox potential, E_{sol}, more negative than this, then the semiconductor will equilibrate its Fermi energy, E_f, with the solution.[34] To accomplish this, there is a net transfer of negative charge to the intimate solution-semiconductor interface creating a negative surface potential. This surface charge repels electrons, creating an upward band bending within the space charge region, W_D, or majority carrier depletion width. Upon illumination, holes generated in this region migrate to the surface while electrons are repelled from the surface. Conventionally, the E_f is then split into what are called quasi-Fermi energies,

which reflect the average potentials of the holes E_{f,h^+}, and electrons, E_{f,e^-}. The splitting between

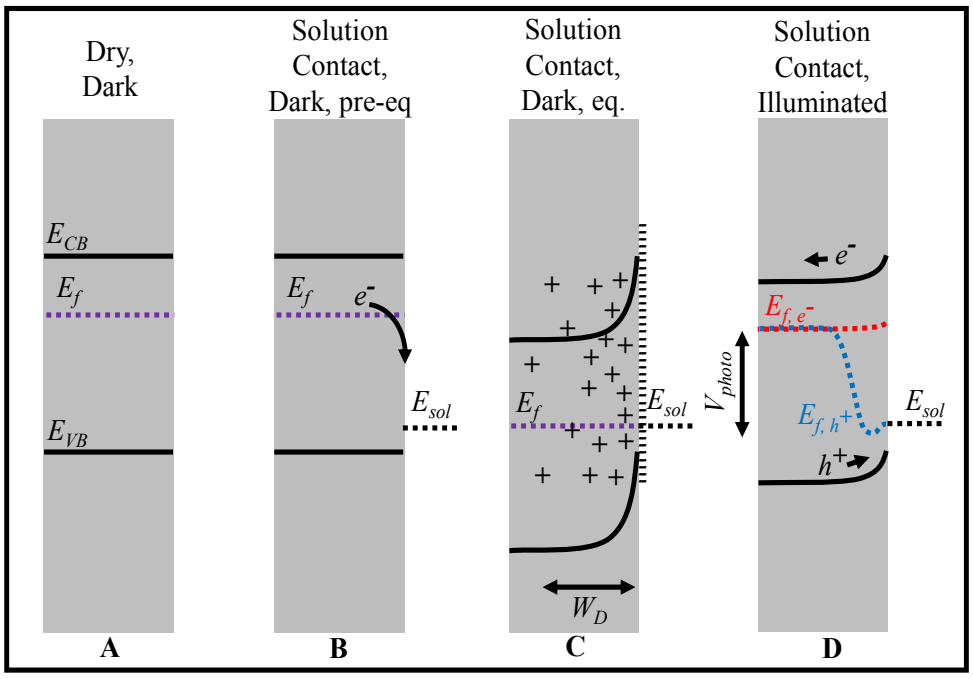

Figure 1.5 – Panel **A** shows a bare n-type semiconductor (grey), in the dark. **B** brings the semiconductor into solution contact and shows the energy alignment before charge equilibration. **C** shows the creation of a space charge region with net electron transfer to the interface, depleting charge within the semiconductor depletion width, W_D. Upon illumination, in **D**, the electron and hole quasi Fermi energies split, creating photovoltage, V_{photo}.

the E_{f,h^+} and E_{f,e^-} measured relative to the solution potential define the solar cell's photovoltage. This electrode configuration would function as a photoanode, oxidizing a redox species at E_{sol}. Reviews of *p*-type interfaces and far more in-depth descriptions of this field are presented elsewhere.[34]

1.2.5 QD Based Photoelectrochemistry – QD Sensitized Solar Cells

In a dye-sensitized solar cell (DSSC), a relative of the bulk solution junction solar cell described above, a molecular dye adsorbs onto a 10-20 μm electron transporting matrix, most often mesoporous TiO_2.[35] This titania contacts a dense transparent conductive oxide (TCO). The TCO runs to the load on the cell, then to a counter electrode on the other side of the cell. That counter electrode is typically 25-50 μm from the anode. The dye-TiO_2-TCO assembly, is immersed in a non-aqueous redox electrolyte, traditionally, iodide/triiodide (I^-/I_3^-) in acetonitrile.

When properly functioning, the dye absorbs a photon and, in its excited state, injects an electron rapidly (~1 ps) into the TiO_2 conduction band. The remaining hole in the HOMO of the dye oxidizes the I^- in solution to I_3^- on the μs timescale. The triiodide begins diffusing out of the mesoporous TiO_2 and over to the counter electrode on the other side of the cell. The injected electron diffuses through the TiO_2 back to the TCO; this is the current produced by the cell. Photovoltage is generated by the increase in Fermi energy in the TiO_2, E_f, produced from electron injection. In a DSSC, voltage is measured as the difference between the semiconductor

E_f and the equilibrium solution redox potential. On the other side of the cell is the cathode counter electrode, most often Pt, which reduces the oxidized I_3^- back to I^- with the electron from the photoanode, completing the circuit.[36] An important note: charge separation in DSSCs is not a product of a space charge region as the mesoporous TiO_2 has a crystallite size, ~25 nm, which is less than the material's depletion width, ~150 nm. Thus electron transport is considered diffusion, not drift as occurs within a space charge region.

Graetzel's development of the original DSSC can been likened to Edison's development of the carbonized filament for the incandescent light bulb; a combination of inspiration, iteration and sheer brute force struck a balance to find a set of conditions to produce a useful construct. This comparison reflects the delicate balance in charge transfer rates required to have a functioning device. As an example, recombination of injected electrons in the TiO_2 conduction band with oxidized redox shuttle in solution, must be extremely slow for a DSSC to work. Most redox

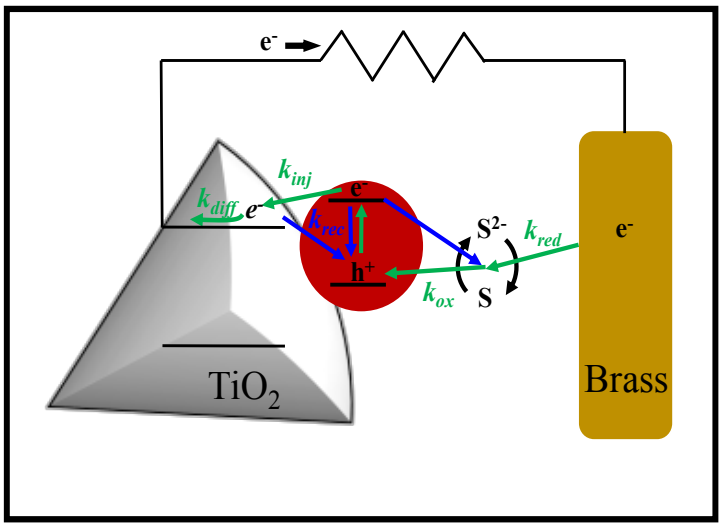

shuttles are reversible one electron shuttles, making this recombination pathway extremely prevalent. The iodide/triiodide system, however, is a two electron couple, and TiO_2 happens to be a terrible catalyst for that reduction. When developing new sensitized devices, which rely on mesoporous TiO_2, controlling the various recombination rates is a major task.

Figure 1.6 – Standard architecture of a QDSSC. A DSSC is nearly the same architecture – a dye replaces the QD and different redox mediators are used. The desirable forward electron transfers are in green (injection, diffusion, reduction and oxidation). Parasitic recombination losses are shown in blue. Interfacial recombination across the TiO_2 solution interface is perhaps the most competitive and detrimental on account of the mesoporous TiO_2's high surface area.

A QD sensitized solar cell (QDSSC, **Figure 1.6**) operates on the same principles and delicate balance as a DSSC but with a few notable differences.[37] Instead of a non-aqueous, I^-/I_3^- redox electrolyte, QDSSCs employ an aqueous polysulfide electrolyte, $S_n^{n-}/S_n^{(n-1)-}$. This electrolyte system saw its development during the 1970s and 1980s as a stabilizing electrolyte for bulk, solution junction solar cells.[34] It functions well as a similarly quasi-reversible redox couple like

I^-/I_3^- and also forms a thin sulfur interfacial barrier to passivate the underlying semiconductor from corrosion reactions involved with contacting water. Such an electrolyte also necessitates different counter electrodes, most often brass, that can withstand sulfur poisoning. The difficulty of S reduction can often pose a problem, k_{red}, both from a kinetics problem as well as long term poisoning phenomenon. As in a DSSC, the principles of Marcus Theory govern the various charge transfer steps. Increasing the injection energy ($\Delta G_{rxn} = E_{TiO2\ CB} - E_{QD\ LUMO}$), decreasing the distance between the QD or dye and TiO_2, and decreasing the barrier height, all increase the injection rate.[38,32] Importantly, it has become apparent that hole transfer, k_{ox} in **Figure 1.6**, to solution is often the kinetically limiting step in most QDSSCs.[39] This is a product of both the smaller driving force for oxidation than for injection as well as the moderately difficult kinetics associated with the two electron oxidation of the polysulfide electrolyte. As with QD based photocatalysis, the hole's extended residence on the QD creates an additional recombination route for the electron in the TiO_2 conduction band.

1.3.1 – General Approaches to Artificial Photosynthesis

As discussed in Chapter One, artificial photosynthesis is the human-made process by which solar energy is converted to chemical energy. Such a conversion may be accomplished employing a variety of methods and may target a wide array of fuels. The most fundamental chemical reaction involved is water oxidation. This electrochemical half reaction provides the protons and electrons for the bond formations involved in the fuel forming reaction. Equally important, however, is the production of O_2. During terrestrial fuel combustion, O_2 is the terminal electron acceptor, so to complete the 'circuit', oxygen must be produced during overall photosynthesis. This is shown schematically below, in **Figure 1.7**.

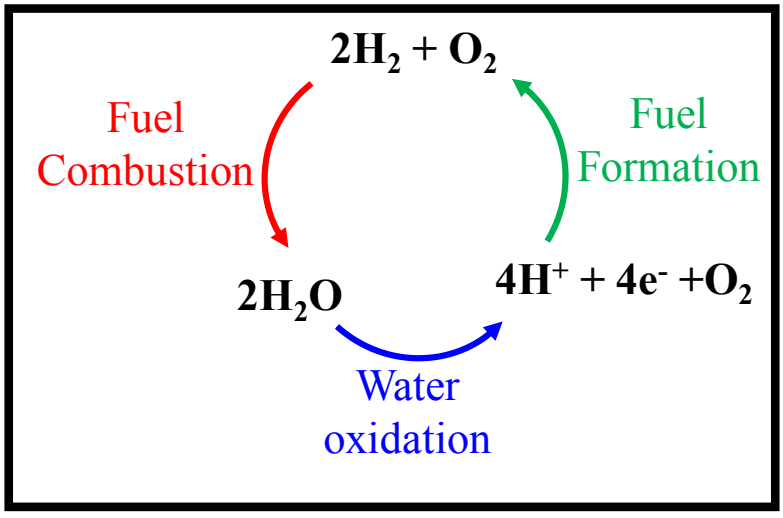

Figure 1.7 – A complete fuel forming and fuel combustion cycle emphasizing the importance of water oxidation to artificial photosynthesis.

The most straightforward method to accomplish the water oxidation and proton reduction necessary for the fuel formation step above is to provide voltage and current to an electrolyzer

with a separate photovoltaic module, **Figure 1.8**. This approach has the fewest unknowns given its reliance on existing technologies. In addition, it can operate at a very high efficiency with the efficiencies of the two processes being essentially multiplicative. Some disadvantages to this approach revolve around the possibly higher balance of systems costs that would arise from having two separate processes operating in tandem.

It may be possible to reduce these balance of systems costs by integrating the photovoltaic and the electrolytic processes. This approach is shown in **Figure 1.8** as integrated photoelectrochemical water splitting. In such an architecture, the electrocatalysts have been deposited directly onto the semiconductor interfaces, thus eliminating the need for an ex-situ electrolyzer. Such a system will be described in Chapter 4. While the balance of systems problems may be reduced, there are a number of other problems that arise with an aqueous

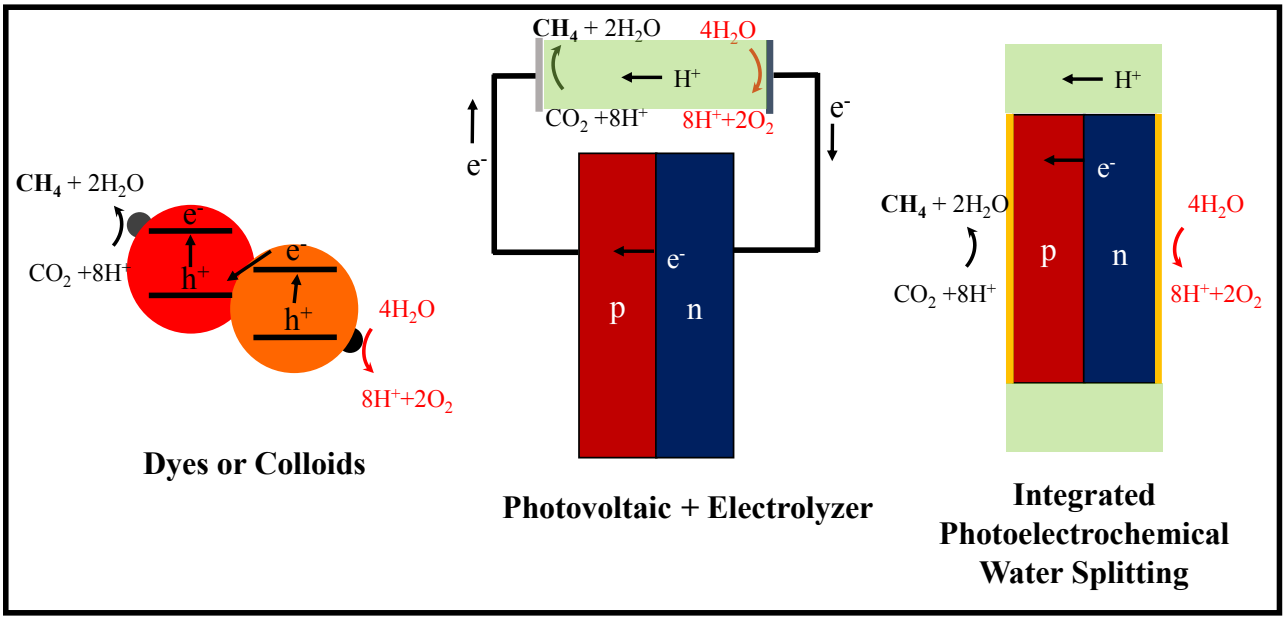

Figure 1.8 – General methods for artificial photosynthesis. On the left is a colloidal or molecular scheme. Two separate materials absorb a photon, generate an excited state, and transfer their charges to either a fuel reduction or a water oxidation electrocatalyst. Charge transfer between the two absorbers may be directly interfacial, or it may be mediated by a redox couple (not shown). In the center, a photovoltaic - electrolyzer pair is shown. The photovoltaic provides voltage and current to an ex-situ electrolyzer. This architecture has the fewest unknowns. Integrated photoelectrochemical water splitting is shown at right. Interfacial electrocatalysts have been deposited on the photovoltaic's surface, mitigating the need for an ex-situ electrolyzer. This architecture engenders a wide array of challenges, most important of which is aqueous stability of the photoanode (blue box) in the corrosive conditions

semiconductor contact. These issues will be discussed more extensively later in Section 1.3.3.

Finally, dyes or light absorbing colloids may be used in place of a photovoltaic architecture. In both cases, a catalyst must be present to mediate the fuel forming reduction and water oxidation steps. These catalysts may be interfacially adsorbed or bonded to the light absorber, or they may be free floating species. Charge transfer to complete the circuit between the two absorbers may

be similarly interfacial, or it may occur via a soluble redox mediator. These three systems have been studied extensively in the literature and have been reviewed elsewhere.[40–43]

1.3.2 Photoelectrochemical Approaches to Artificial Photosynthesis

Artificial photosynthesis (AP) is the process by which a device converts solar energy to chemical energy. At its core, it can be broken into three major pieces – light harvesting, charge separation and catalysis. Natural photosynthesis relies on two light absorbing centers, photosystems I and II, which transfer charges using three elegant electron cascades to direct the electrons between the two light absorbing centers and to the two catalytic centers. These two, spatially separated catalysts oxidize water to O_2 (photosystem II) and reduce $NADP^+$ to NADPH (photosystem I).[44,45] AP can employ a variety of methods including colloidal, molecular, photovoltaic-electrolyzer tandems and photoelectrochemical, but all rely on the same spatial control of charge transfer between light absorbing centers and their respective catalysts.[40,46,41,47] This section will focus on the methods and stability issues associated with photoelectrochemical approaches to artificial photosynthesis

1.3.3 Thermodynamic and Kinetic Requirements for Electrocatalyzed Water Splitting

The water oxidation half reaction, below, requires the bulk of the free energy necessary for AP. Fuel forming reactions, the reductive half reactions, relevant to AP, proton reduction to H_2 and CO_2 reduction to CH_4, e.g., require no or little extra free energy:

$$\begin{aligned} 2H_2O \rightarrow O_2 + 4H^+ + 4e^- \quad & 1.23\ eV \\ 2H^+ + 2e^- \rightarrow H_2 \quad & 0\ eV \\ CO_2 + 8H^+ + 8e^- \rightarrow CH_4 + 2H_2O \quad & -0.24\ eV \end{aligned}$$

The thermodynamics, however, do not include kinetic considerations for any of these reactions. The observed kinetics are a result of the energy landscape the reactants and intermediates see during the overall reaction. Complex reactions with multiple steps and high energy intermediates, such as CO_2 reduction, may have little change in free energy but can be extremely kinetically challenging.[48] Additional energy is therefore required to surmount this activation barrier and run the reaction at a reasonable rate. In electrochemistry, this value is known as overpotential. Practically speaking, if one applies 1.23 V to an iridium oxide electrode in water at pH 0, the scientist will not observe any water oxidation current. It is not until he or she applies sufficient overpotential to the electrode, another 200 to 300 mV for the very best water oxidation catalysts, that he or she observes any water oxidation current. This is a powerful extension of Marcus theory, electrochemical overpotential is fundamentally equivalent to the activation energy, $\Delta G^{\ddagger}$.[25,26] Consequently, to surmount the thermodynamics and overpotential for the two half reactions involved in H_2 production, at least 1.7 V are required, while if the target fuel is methane, more than 2.5 V will be required to accommodate the >1V overpotentials typically required by electrochemical CO_2 activation.[43]

1.3.4 Photoelectrochemical Water Splitting

In PEC based AP, the most basic requirement for the system builds out of the thermodynamics imposed by the water splitting reaction. For proton reducing cells, the underlying photoelectrochemical cell must produce at least 1.7 *V* in photovoltage. Most often, two photoelectrodes, a photoanode (*n*-type) and a (p-type) photocathode, produce that voltage: this architecture is called a tandem cell. Single absorbers would necessitate a bandgap >2.5 *eV* to provide sufficient voltage to drive both water oxidation and proton reduction. Such a wide gap severely limits maximum efficiency.[49] The photoanode oxidizes water, while the photocathode consumes the electrons and protons from the photoanode to produce the fuel (**Figure 1.9**). If there is a solution junction, there is an additional requirement that the semiconductor's flat band potential, E_{CB} or E_{VB}, have enough energy to accommodate the thermodynamics and kinetics of

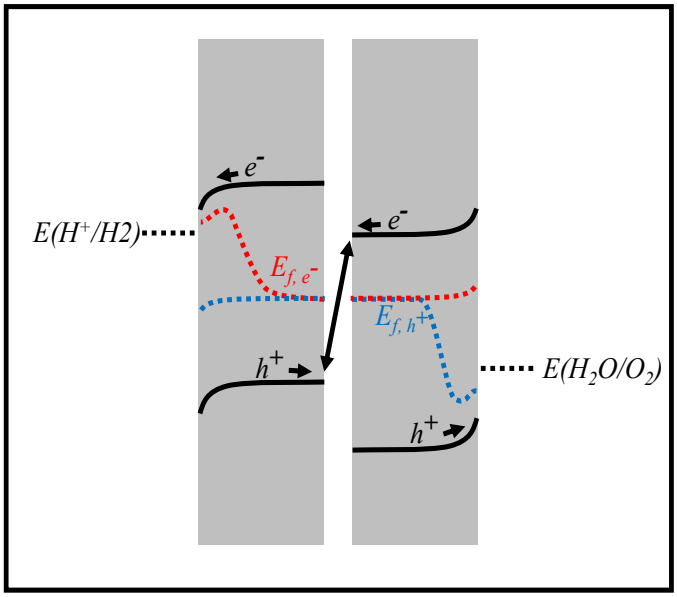

Figure 1.9 – A tandem photoelectrochemical water splitting cell. The *p*-type photocathode on the left accumulates electrons at the interface upon illumination raising the E_{f,e^-}. On the right, the n-type photoanode accumulates holes at the interface, lowering the energy of the E_{f,h^+}. Catalysts have been omitted for clarity, but they would function at energies intermediate to the thermodynamic potentials and quasi Fermi energies to promote charge transfer and accommodate overpotential. The splitting between the two surface quasi Fermi energies at the two interfaces must produce the necessary 1.7 *V* described

reducing or oxidizing their intended substrates. That redox process, in the vast majority of cases, is catalyzed, typically by a metal. Thus charge transfers first to the catalyst, then subsequently to the desired water oxidation or proton reduction reaction. Architectures in which an overlying material separates and screens the semiconductor from the solution potential is referred to as a buried junction. This architecture relaxes the flat band potential condition.[43] A Schottky or *p-n* junction(s) usually provides the necessary voltage to the electrocatalyst in this case.

1.3.4 Semiconductor Photocorrosion

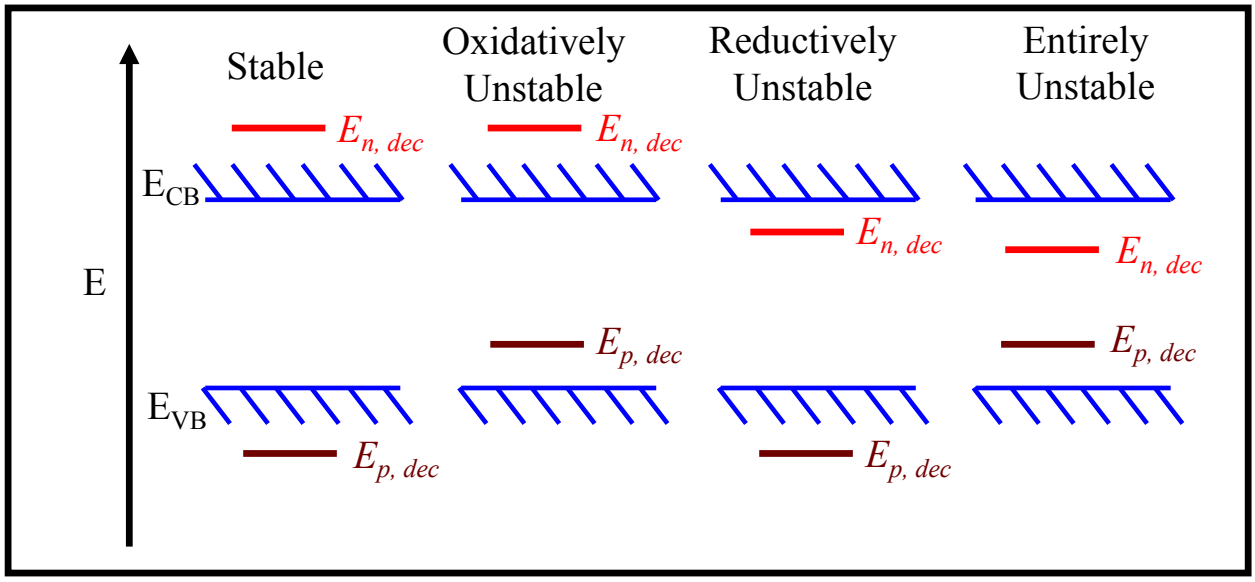

Figure 1.10 – A semiconductor will be stable in water if the aqueous decomposition potentials, $E_{n,dec}$ and $E_{p,dec}$, are outside of the bandgap (shown at left). If either or both the reductive $E_{n,dec}$ or the oxidative $E_{p,dec}$ lie within the material's bandgap, the material will have sufficient potential to oxidize its bands and will eventually corrode (all others). A common misconception is that the decomposition potentials must only be more stable that water oxidation or proton reduction. If the potentials are within the gap, both reactions (water oxidation and semiconductor corrosion) will occur, with the relative rates being determined by the $\Delta G^{\ddagger}$ of the two processes.

An unfortunate reality became apparent early on in developing PEC approaches to artificial photosynthesis – the high quality semiconductors, such as GaAs, InP and CdSe, with visible bandgaps, high carrier mobilities, controlled carrier concentrations and long lifetimes were all unstable in water. Instead of oxidizing water, the semiconductors would oxidize the bonds in their own lattices and subsequently dissolve or react terminally with water to produce an inactive oxide.[50] The energy at which that decomposition reaction occurs is known as the decomposition potential. Shown, schematically in **Figure 1.10**, if either reductive or oxidative decomposition potentials, $E_{p,dec}$ or $E_{n,dec}$, of a material lay within the band gap, the material could corrode its own bonds under illumination. Even if the decomposition potentials are more stable than water oxidation or reduction, they are still thermodynamically accessible to electrons and holes within the bands, and the material will eventually corrode. This is a common misconception within the community.[50,51] Pourbaix diagrams constructed for every non-oxide material show this feature: corrosion reactions occurred at potentials that were either less positive than the water oxidation potential or were within the material's bandgap.[52,53] As a result, none can be used in direct solution junctions for artificial photosynthesis. While oxide materials, such as TiO_2 and WO_3, were sufficiently stable and were shown as the first examples of photoanodes for water splitting, their wide band gaps limit photocurrents to ~2 mA/cm^2.[54,55] New oxide materials with smaller bandgaps, like bismuth vanadate or doped and disordered TiO_2, are the focus of a large amount of new research.[56,57]

1.3.5 Surface Protection Strategies for Semiconductors

As photocorrosion is a water mediated process, the reaction can be slowed or totally averted by using a barrier layer on the semiconductor surface to exclude water.[58] This barrier must have several critical features: it must be perfectly conformal, moderately transparent, moderately conductive and stable in water. Several strategies have been shown to achieve this end. The most common can be considered a buried junction. A thick (>100 nm) conformal, conductive metal oxide film is deposited on a planar photovoltaic surface. The metal oxide must be judiciously chosen so as not to introduce excessive defects at the semiconductor surface while still being capable of conducting sufficient charge.[59–61] While simple in design, realization is extremely challenging. The vast majority of metal oxides are *n*-type and the underlying PV device for the photoanode must have an *n*-type absorber layer contacting the metal oxide, since the photoanode must accumulate holes at the surface.[62] If two *n*-type materials contact and equilibrate their Fermi energies, a large barrier will form and impose a giant resistor in the system's equivalent circuit.[5] Thus, these thick conductive layers must be *p*-type, of which there are relatively few oxide examples. A sub-type of this design relies on conductive polymer coatings to bulk electrodes. Moderately conductive, the polymers passivate well, but still allow partial penetration by water and function as incomplete barriers.[63] A relative of this concept is presented in Chapter 4 as a protection scheme for semiconductor QDs and will be discussed more in that chapter. Extremely thin oxides can also be used as tunneling barriers. To support moderate current densities, these layers must be <5 nm with the same requirements of conformality.[64,65] Very few examples of this design exist on account of the difficult fabrication.

1.4 Concluding Remarks

Quantum dot size, shape, and composition can be manipulated to control their underlying electronic structure. As a result, they have become the focus of a great deal of research related to solar energy conversion. Many of the challenges of solar fuel production, specifically, center on charge separation and stability. QDs can readily be designed to separate charges, but they suffer from the same instability that plagues their parent, bulk counterparts. Chapters 2 will present research that focuses on both the charge separating capabilities of QDs and their facile interfacing with catalysts. Chapters 3 and 4 will develop a new approach to QD photocorrosion protection to address semiconductor photocorrosion in sensitized photoelectrochemical water splitting.

Chapter Two – Structural and Electronic Study of an Amorphous MoS_3 Hydrogen-Generation Catalyst on a Quantum-Controlled Photosensitizer[66]

2.1 –Molybdenum Sulfide Catalysts

The design and synthesis of practical photocatalysts for the production of solar fuels, such as H_2, is a major challenge in developing sources of renewable energy.[42,67] Catalyst development requires an understanding of the mechanism(s) involved and the nature of the active site.[43,47] While platinum group metals have unrivalled activity for both hydrogen and oxygen evolution, they are scarce and expensive. [68,69] Photocatalytic systems relying on earth-abundant materials are therefore desirable for large scale energy production.[70,71] Herein, we examine the structure and electronic properties of anamorphous molybdenum sulfide species and its possible use for photocatalytic hydrogen evolution. The catalyst was grown on a seeded quantum-rod sensitizer, a model system for investigating the photophysics of solar fuel generation. This catalyst's activity is shown experimentally to be associated with under-coordinated molybdenum centers, and we document that a reduced form of MoS_3 is an active catalyst for hydrogen generation.

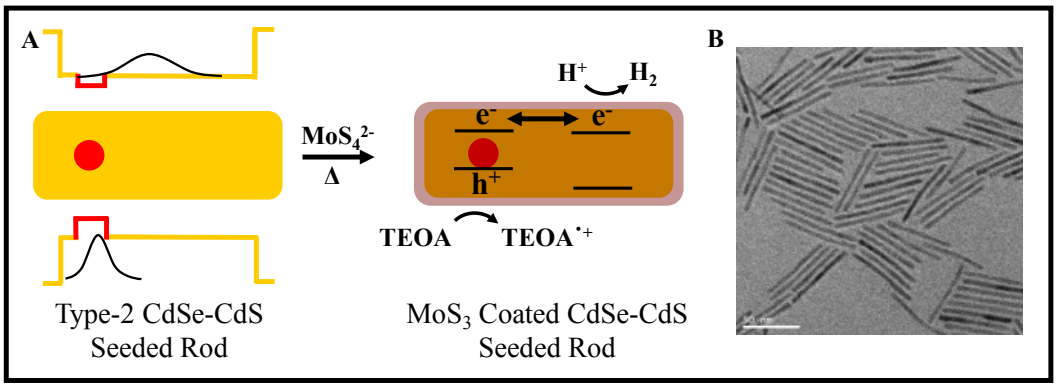

Figure 2.1 – **A** MoS_3 deposition on a CdSe-seeded CdS nanorod, with photocatalytic hydrogen production in the visible using triethanolamine (TEOA) as a sacrificial reductant. **B** Bright field TEM image of 60 nm CdSe seeded CdS nanorods. The scale bar is 50 nm.

Molybdenum sulfide containing active sites are prevalent in both biological enzymes and industrial catalysts. Mo metalloenzymes are involved in carbon, nitrogen, and sulfur metabolism, while synthetic molybdenum sulfides serve as industrial hydrotreating catalysts and are proven electrocatalysts for the hydrogen evolution reaction (HER).[72–75] MoS_2, incomplete cubane $[Mo_3S_4]^{4+}$ clusters, molecular molybdenum catalysts, and amorphous MoS_2 made by an electrochemical reduction of MoS_3 have been shown to be active HER catalysts.[76–80] Highly active HER catalysts, including Pt, have a Gibbs free energy of H adsorption (ΔG_H) close to zero.[81] Density functional theory calculations propose that the equatorial sulfur atoms in Fe–Mo cofactors in nitrogenase enzymes as well as the bridging S atom on the edge sites of MoS_2 bind H atoms with $\Delta G_H \approx 0$. These calculations, coupled with scanning tunneling microscopy (STM) studies, have indicated that molybdenum sulfide based hydrodesulfurization and HER catalysts derive their activities from under-coordinated atoms at their edges. Recent investigations of MoS_2 nanoparticles using STM combined with electrochemical measurements have revealed that HER activity scales with the number of edge sites, rather than nanoparticle area, adding substantial evidence that undercoordination is critical to activity.[76]

There is also substantial current interest in molecularly thick and structurally disordered metal oxide and sulfide layers supported on electrodes, surfaces, and nanoparticles as potential catalysts for the HER and oxygen evolution reaction (OER). [80,82] Such ultrathin films can support a variety of unusual and possibly favorable bonding geometries and may retain flexibility in healing and recovering.[83] Despite their potential, such systems remain very difficult to characterize because they are amorphous with significant structural heterogeneity. Mechanisms are difficult to pin down when structural and electronic characterization is lacking.

In this work, we use X-ray absorption techniques to obtain structural information on a catalytically active disordered molybdenum chalcogenide species that was grown on a well-controlled seeded quantum rod photosensitizer system with very high surface area. The high surface area of the colloidal system enables us to employ a variety of X-ray characterization techniques. Yet the system is also well-defined: Amorphous layers of MoS_3 are deposited on quantum controlled photosensitizers. We take advantage of recent work showing that cadmium chalcogenide nanocrystals can be engineered to systematically control the separation of photogenerated holes and electrons, thus allowing us to modulate the photochemical yield of hydrogen.[8,17,19,21,84]

2.2 MoS_3 Deposition on CdSe seeded CdS Nanorods

CdS nanorods grown on CdSe seeds with varying diameters and pure CdS nanorods of differing length were synthesized by a seeded-growth method previously reported.[17] These particles have been the subject of research interest as a model system for investigating photochemical HER because their bandgaps and band offsets are appropriate for driving proton reduction from water, and the ability to control the pathways of charge migration could offer additional means for making more oxidatively stable photocatalysts.[8] A sampling of these nanorods is shown in **Figure 2.1B**. The pseudo-type II heterojunction in the CdSe/CdS nanorod heterostructure results in a photogenerated hole that is spatially confined to the core and an electron that can delocalize over the entire structure. This inhomogeneous spatial distribution, a result of the staggered band

alignments from CdSe and CdS that are controlled with the seed and rod diameters, decreases electron-hole overlap, and increases the exciton lifetime as the rod length increases, or the seed

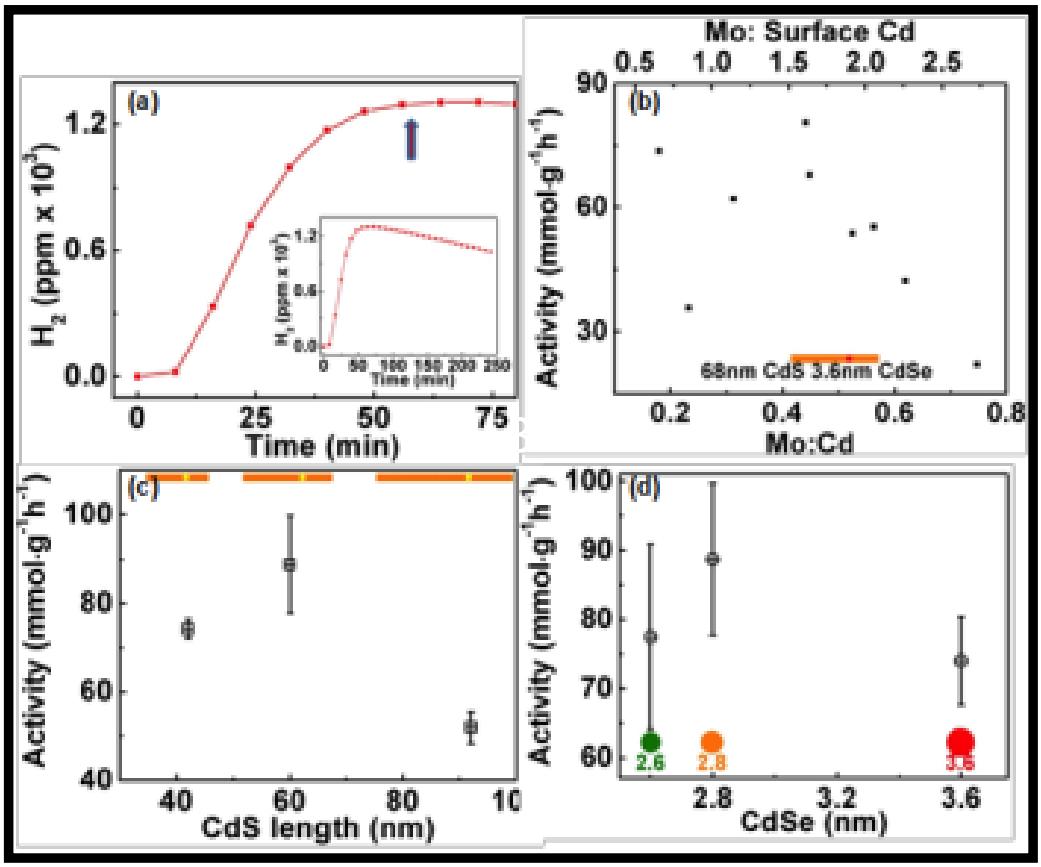

Figure 2.2 – (a) A typical H_2 production analysis for a MoS_3 coated CdS/CdSe nanorod using 450nm light with an induction period of ~ 50min. 0.07nmol of rods were used with 5.0ml [0.1] pH 7.0 tris buffer and 0.20ml TEOA. The activities are derived from the maximum rate of H_2 produced, as indicated by the arrow. The inset shows the four hour measurement. (b) Maximum photocatalytic activity (mmol H_2•g-1h-1) correlated with surface MoS_3 coverage for 68-nm CdS/3.6-nm CdSe. (c) Activity correlated with CdS nanorod length for 2.8-nm CdSe seed. (d) Activity for different CdSe seed sizes in a 65-nm CdS nanorod. (c) and (d) show an average of 3 data points.

diameter decreases.[19]

A one-step thermal decomposition of $(NH_4)_2MoS_4$ was used to deposit an amorphous molybdenum sulfide film on the nanorods. In comparison, previous work involving cadmium chalcogenide photosensitizers decorated with MoS_2 co-catalysts involved either bulk CdS modified by high temperature calcinations under H_2S, or quantum confined CdSe structures functionalized by high-power ultrasonication.[85,86] Following the seeded rod synthesis, the octadecylphosphonic acid (ODPA) coated nanorods were dissolved in toluene and mixed with o-dichlorobenzene and an aliquot of $(NH_4)_2MoS_4$ dissolved in N-methylpyrrolidone, as shown

schematically in **Figure 2.1A**. The mixture was then subjected to microwave-based heating at 90°C for 50 min (details are provided in Table S2.1 in the Appendix), after which the initially hydrophobic yellow-orange nanorod solution acquired a brown color and a marked solubility in water. UV-Vis absorption of the as-synthesized rods and those modified by this thermal deposition exhibit the same excitonic transitions and energies (Figure S2.1), indicating that no etching of the CdS rods, nor deposition of MoS_2, which has an absorption associated with its bandgap of ca. 1040 nm, has occurred, though some aggregation is apparent from the scattering background. These results taken together are consistent with the thermal deposition of a surface coating on the rods. Deposition of this thin film results in a photochemically active system for hydrogen generation. The MoS_3 coated nanocrystals have from 1 to 4 Mo atoms deposited for every Cd on the surface of the nanorod, as measured by induction coupled plasma-optical emission spectroscopy (ICP-OES). The volume and surface area of each nanorod was estimated from TEM images (for length) and UV-Vis spectra (for diameter)—details are in the SI. The amorphous nature of this coating can be seen in Figure S2.2a; following deposition, the powder X-ray diffraction (XRD) pattern shows no additional reflections, while high resolution TEM (Figure S2.2b) gives only lattice fringes arising from CdS planes.

2.3 – Photocatalysis of MoS_3 Coated CdSe Seeded CdS Nanorods

After thermal deposition, the rods were precipitated and resuspended in acetonitrile to remove any excess dissolved Mo species not physically attached to the rod. This step was repeated again, after which 0.05-0.10 nmol of rods were suspended in a 5.0 mL solution of 0.1 M pH 7.0 tris base buffer and 0.2 mL of the sacrificial reagent, triethanolamine (TEOA) at RT. Control experiments with as-synthesized CdSe/CdS nanorods show negligible rates of H_2 production under the photocatalytic conditions employed here. Irradiation of a solution of $(NH_4)_2MoS_4$ or MoS_3 in water under the same conditions gave no hydrogen either. Therefore we conclude that intimate contact between the MoS_3 surface layer and the nanorods is vital for efficient charge transfer. Pure CdS dots and rods have activities that are, at best, a half of the seeded rods, highlighting the importance of the lengthened exciton lifetime in improving catalytic activity. A maximum activity of 100 $mmol H_2 \bullet h^{-1} g^{-1}$ isobtained using MoS_3-coated 60 nm CdS rods containing 2.8 nm CdSe seeds, with an apparent quantum efficiency (AQE) of 10% at λ=450 nm. This efficiency is comparable to a similar system with Pt co-catalysts on the tips of the same rods, which display an AQE of 20% under the same illumination conditions.[21] This system (100 $mmol H_2 \bullet h^{-1} g^{-1}$) has a far higher activity than previous studies of photocatalytic H_2 from crystalline MoS_2 photosensitized by cadmium chalcogenides. The activity of bulk CdS/MoS_2 was 5.3 $mmol H_2 \bullet h^{-1} g^{-1}$ and nanoribbons of CdSe/MoS_2 were 0.89 $mmol H_2 \bullet h^{-1} g^{-1}$.[85,86]

Figure 2.2B plots the overall activity for 68 nm long CdS rods incorporating a 3.6 nm CdSe seed versus Mo:Cd surface coverage and absolute Mo:Cd ratio. Surface Mo composition correlations with activity for all other heterostructure dimensions are given in Figure S2.3. The activities are extracted from the maximum rate of production of hydrogen, as given by the gas chromatogram (**Figure 2.2A**). For all the heterostructures, the optimum Mo: surface Cd ratio ranges from 0.7-2.0. When the Mo:Cd ratio is too high, light absorption by the CdS nanorod is inhibited by the coating itself. To extract the dependence on seed size, a series of rods approximately 65 nm in length were grown with 2.6-, 2.8- and 3.6-nm CdSe seeds; for the dependence on rod length, 42,

60 and 92 nm long rods were synthesized with a 2.8-nm CdSe seed. The TEM images and UV-Vis spectra of these rods are shown in Figure S2.4.

Photocatalytic H_2 production depends strongly upon nanorod length. As shown in **Figure 2.2C**, for rods of different length with the same 2.8-nm CdSe seed, the highest activity is observed for 60-nm rods, followed by the 42-nm rods and then the 92-nm rods. We can understand these results by recognizing that the presence of the seed acts to separate photo-generated electron-hole pairs, with the hole remaining localized in the seed, while the electron is largely delocalized. The effect of the seed only extends over a finite length, however. While the longest rods may absorb more light, there is an increased probability of absorption in the CdS only region, and the photo-generated electron-hole pair may recombine without splitting. Excitons generated too far from the seed will not be subject to the staggered band alignments at the interface of the CdSe seed and CdS, and hence will not experience the added splitting pathway to the other recombination pathways. In shorter rods, the excited electron may not delocalize into as large a volume as possible and will have more wavefunction overlap with the localized hole, resulting in a truncated excitonic lifetime. This argument implies an ideal length, which we observe at 60 nm. This optimum length also appears in some of our previous work, where Pt tips were used as the H_2 producing cocatalyst with the same seeded rods.[21]

Comparing seeds of different size with rods of approximately the same length (~65 nm) in **Figure 2.2D**, we see that large seeds of 3.6 nm perform relatively poorly. This is because large (>3.5 nm) CdSe seeds only weakly confine photogenerated electrons, so their conduction band energy approaches the bulk value, which lies significantly below the quantum confined CdS conduction band energy. With this band offset between the two materials, the electron cannot delocalize significantly into the CdS portion of the rod. This results in the electron and hole wavefunctions overlapping substantially to produce a shortlived exciton.

The decrease in H_2 production over time is attributed to the gradual dissolution of MoS_3 from the surface of the rods. Even in the absence of light, 2-20% of the starting Mo content is found in solution after 5 h. This dissolution is also seen in the incomplete cubane $[Mo_3S_4]^{4+}$ clusters.[77,81] ICP-OES measurements conducted on the supernatant and a pellet of the MoS3-coated nanorods exposed to photocatalytic conditions revealed only Mo, with no Cd in solution. This decomposition is not accelerated by light. The unstable nature of this surface coating of MoS_3 is consistent with an incoherent interface between the trigonal prismatic MoS_3 and wurtzite CdS nanorod. Work towards a self-healing catalyst is being pursued.[82]

2.4 – Structural and Electronic Characterization of the MoS_3 Catalyst

Figure 2.3A shows X-ray photoelectron spectroscopy (XPS) data of the Mo coated rods before and after catalysis. The binding energy of the Mo $3d_{5/2}$ (Mo $3d_{3/2}$) feature at 229.9 eV (233.0 eV) suggests that the oxidation state of the precatalyst is Mo(V) before photocatalysis. Upon photocatalysis, the Mo $3d_{5/2}$ (Mo $3d_{3/2}$) peak is shifted to lower energy at 228.6 eV (231.8 eV), indicating the reduction of Mo(V) to Mo(IV). This Mo(IV) state was also observed in the amorphous MoS_3 precatalyst as well as the actual MoS_2 electrocatalysts reported by Merki et al.[80]

The Mo K-edge X-ray absorption near edge structure (XANES) and Fourier transformed extended X-ray absorption fine structure (FT-EXAFS) spectra of the Mo coated rods before and after catalysis are shown in **Figure 2B,C**. In the XANES spectrum, the rising edge energy is shifted to higher energies (+1.0 eV) after catalysis, accompanied by a change in shape. Although the XANES energy is often used as an indicator of the metal oxidation state, it is difficult to interpret spectra particularly when the reaction is accompanied by changes in ligand environment. For the formal oxidation state of Mo, we therefore rely on the XPS result, which is a direct indicator of the metal binding energy. The XANES and FT-EXAFS of the Mo coated rods are compared with spectra of crystalline MoS_2, MoS_3, $(NH_4)_2MoS_4$ model compounds (**Figure 2.4**) and truncated cubane $[Mo_3S_4]^{4+}$ clusters.[87] Based on the differences in Mo-S and Mo-Mo distances, MoS_2, $(NH_4)_2MoS_4$ and $[Mo_3S_4]^{4+}$ can clearly be ruled out as structural analogues for the molybdenum sulfide coating on the nanorods.

On the other hand, the FT-EXAFS spectrum is strikingly similar to that of MoS_3, suggesting that the Mo photocatalyst is analogous to the MoS_3 motif.[88,89] The curve fitting result of the Mo-coated rod before catalysis is shown in **Figure 2.3C** (inset).[90–92] The Mo-S and Mo-Mo distances prior to photocatalysis are 2.44±0.01 Å and 2.78±0.02 Å respectively (Table S2). These distances are identical to those found in bulk MoS_3. After photocatalysis, the Mo-S

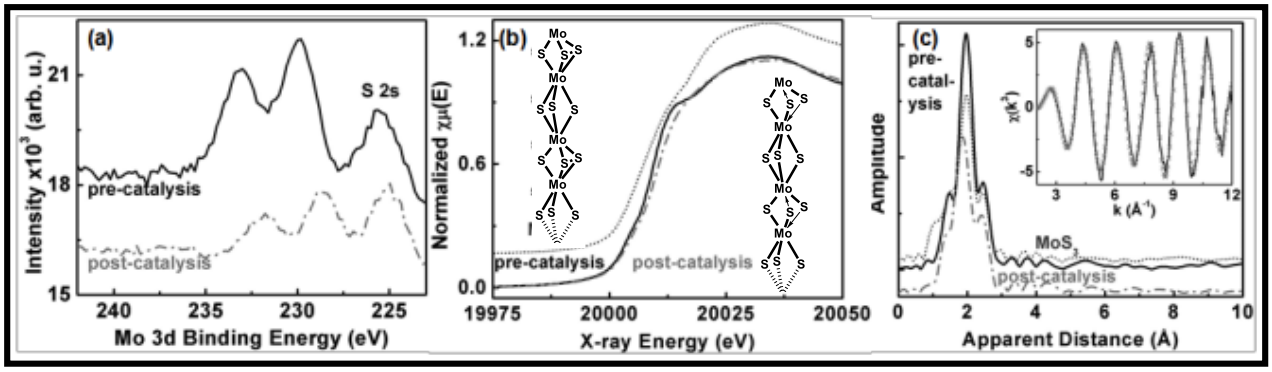

Figure 2.3 – MoS_3 functionalized nanorods before (solid black line) and after catalysis (dotted-dashed grey line). (a) XPS data indicating a reduction of the Mo 3d binding energy during photocatalysis. (b) Mo K-edge XANES spectra for model MoS_3 and MoS_3 functionalized nanorods before and after catalysis. Fitted structures before and the proposed structure after catalysis are shown as insets. (c)Mo FT-EXAFS spectra for MoS_3 and MoS_3 functionalized nanorods before and after catalysis. Inset: fit of MoS_3 (grey crosses) to the pre-catalysis sample (solid line). Note the decrease in Mo-S nearest neighbor distance following catalysis.

distance decreases to 2.35±0.02 Å and the average coordination number (number of sulfur ligands per molybdenum) becomes less than 6. Mo-Mo scattering are seen as a shoulder at R = 2.45 Å in the FT-EXAFS spectra (**Figure 2.3C**), those distances and the number of Mo-Mo scattering partners remain the same before and after catalysis. Alternatively, this peak could be due to the Mo-Cd interactions or a mixture of Mo-Mo and Mo-Cd interactions as we expect Mo to be bridged to Cd by sulfide bonds. However, Mo-Cd interactions may not be observed if distances are long (>4Å) or if there is a large distribution of Mo-Cd distances which can arise from an incoherent interface between wurtzite CdS and the amorphous MoS_3. Neutron

diffraction, XPS and FT-EXAFS data suggest that MoS_3 forms linear chains of face sharing MoS_6 octahedra with the chemical formula of $MoIV(S^{2-})(S_2^{2-})$ or $MoV(S^{2-})_2(S_2^{2-})_{1/2}$ (**Figure 2.3B**, inset).[88,93–95]

The reduction of the Mo centers coupled with a contraction in Mo-S bond length upon catalysis, suggests a modification in the bridging disulfide bond that is proposed for the structure of MoS_3 as the post-catalysis structure inset (**Figure 2.3B**). The bridging disulfide may be altered, each bridging sulfur becoming a terminal thiolate ligand with a dative Mo-S bond. This would account for the lower coordination number determined from fits for post-catalysis samples. A reduction of this bond could donate more electron density into the Mo-S bonding orbitals and result in the shortening of the Mo-S bonds observed in FT-EXAFS, as well as the reduction of

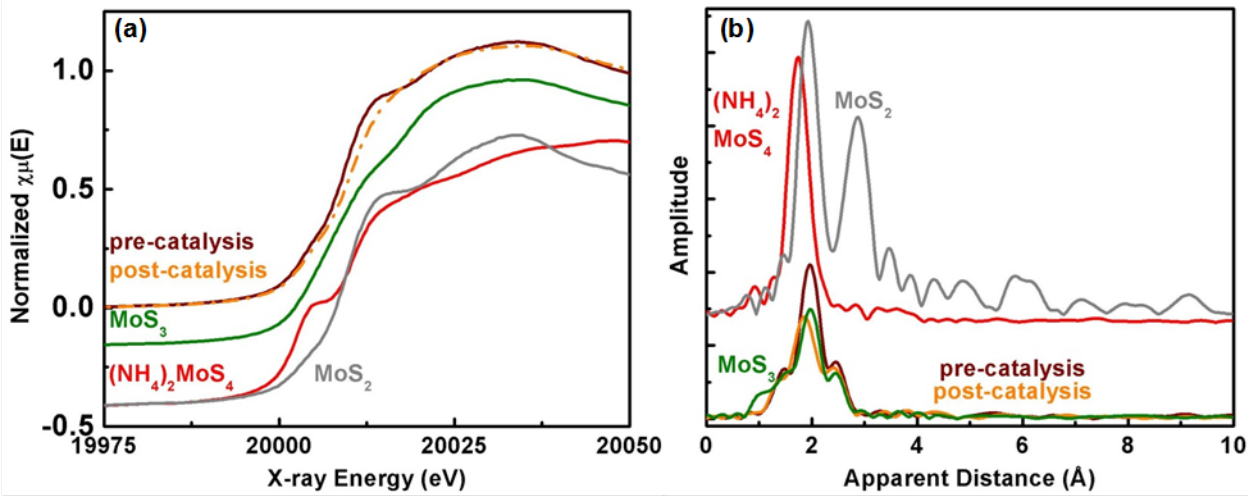

Figure 2.4 – XANES and FT-EXAFS at the Mo K-edge of model compounds: crystalline MoS_2 (grey), $(NH_4)_2[MoS_4]$ (red), MoS_3 (olive) and MoS_3 functionalized nanorods before (burgundy) and after (orange) catalysis.

the Mo center observed by XPS. These structural changes could account for the ~30-50 min induction period observed in all of our samples before hydrogen generation peaks (**Figure 2.2A**). That our catalyst is an amorphous molybdenum sulfide, which undergoes a photo-reduction prior to catalysis marks a similarity to work by Merki et al.[80] They report an electrochemical reduction of MoS_3 to form MoS_2 as the active species. Both crystalline and amorphous MoS_2 have a Mo-Mo interaction at 3.2 Å.[95] We do not observe this scattering feature at 3.2 Å in the FT-EXAFS of any of our samples. However, both the pre-catalyst and catalyst forms here structurally resemble MoS_3. A reduced form of MoS_3 appears to be the active catalyst in our system.

2.5 - Conclusion

To close, our system consists of an amorphous MoS_3 surface coating on semiconductor nanocrystals that is photocatalytically active for H_2 evolution. Comprised of colloidally synthesized, earth abundant and inexpensive materials, it produces H_2 with visible light, with a maximum activity of 100 mmol $H_2 \bullet h^{-1} \bullet g^{-1}$, and AQE of 10% at λ = 450 nm. During the

induction period, the initial MoS^3 precatalyst is photo-reduced to form an under-coordinated species structurally similar to MoS_3, distinct from MoS_2. Further work could be directed into this activation process, whether there is a pH effect would be an indication of the bonding structure between a terminal thiol with a dative bond or a thiolate. Importantly, the high surface area of our active system allowed for the interrogation of a catalyst structure in which most sites were active sites. This is a distinct advantage to many bulk studies where internal structures make discerning surface structural effects difficult. Such an architecture could prove useful in identifying structural changes in other catalyst systems that rely on transition metal sulfide thin films as well as other thin films.

Chapter Three - Ligand Dissociation Mediated Charge Transfer Observed at Colloidal $W_{18}O_{49}$ Nanoparticle Interfaces[96]

3.1 – Charge Transfer at Colloidal Nanoparticles

Colloidal nanoparticles have been a subject of intense interest over the past several decades owing to their possible applications in numerous fields, particularly solar energy conversion.[8,97] This interest stems partly from the optical and optoelectronic properties of these straightforwardly prepared and manipulated, high quality crystalline semiconductor and metallic core materials. To achieve and maintain crystalline and interfacial quality, the nanoparticle core surface is typically passivated by a organic ligand or inorganic interface, providing both

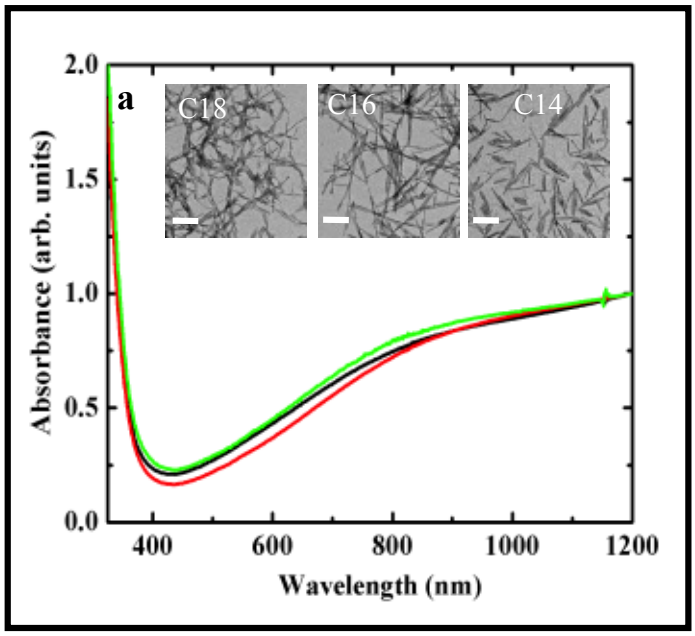

Figure 3.1- Absorbance spectra of $WO_{2.72}$ nanoparticles passivated with different chain length amines (C18 – green, C16 – red, C14 – black). Representative TEM images are shown in insets (Scale bars are 100 nm).

chemical stability and preventing nanoparticle aggregation and fusion. In addition to controlling crystal growth, the ligand shell forms a critical junction that can mediate or limit charge recombination and conversion efficiencies.[98,99] A balance must be struck between each of these qualities as they are inevitably inversely related efficiencies; for instance, while a wide-bandgap shell coating on a semiconductor quantum dot (QD) increases excited state lifetimes with

increasing thickness, it exponentially inhibits interfacial charge transfer kinetics.[100] As a result, the influence of this interface over charge transfer kinetics in electrochemical, photoelectrochemical and photovoltaic devices has been interrogated zealously.[30,101–104]

The vast majority of ligand mediated charge transfer studies has been devoted to an essentially static ligand interface between the donor and acceptor, e.g. QD sensitized or QD film solar cells and gold nanoparticle electrochemical interfaces. In these studies, the ligand forms a tunneling barrier with beta coefficients very similar to those measured in the self-assembled monolayer electrode interface literature. In dispersed colloidal suspensions, the ligand shell, however, is not static, as there is a dynamic equilibrium of surface bound and free ligands in fast exchange.[105–108]

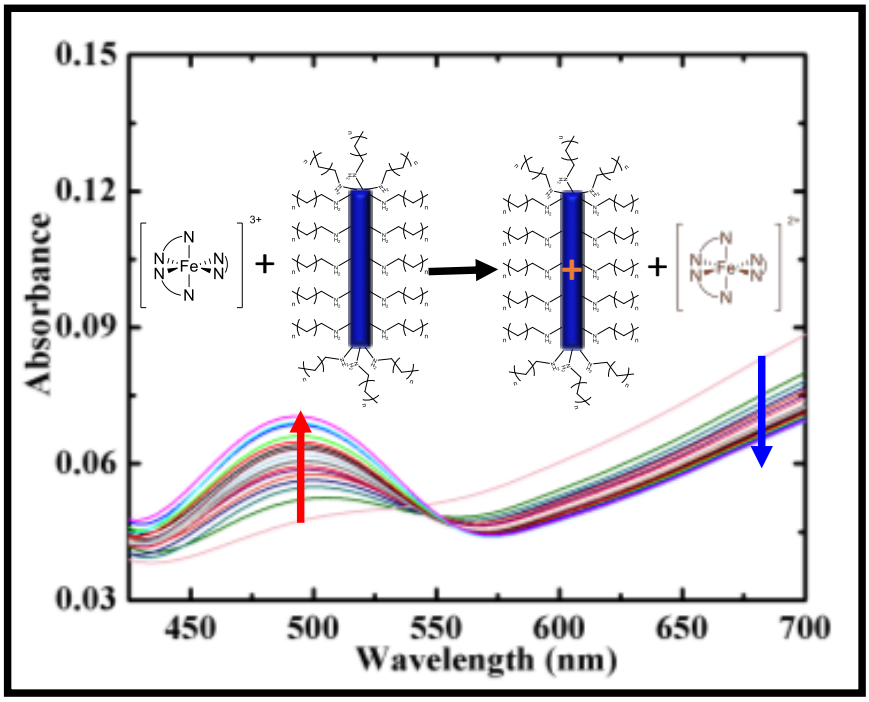

Figure 3.2 – Typical spectra obtained at 15 second intervals following a 20µl injection of $WO_{2.72}$ colloid into a solution of 130µM $Fe^{III}(tm\text{-}phen)_3$, 100mM TBA-$PF_6$ in chloroform are shown above. The increasing absorbance at 510 nm (red arrow) is reduced $Fe^{II}(tm\text{-}phen)_3$. The isosbestic point shifts between 530 and 550 nm over the course of the reaction as the $WO_{2.72}$ plasmon extinction decreases (blue arrow) and redshifts in response to the oxidation. A schematic of the charge transfer reaction is shown in the inset.

Direct electrochemical investigations of charge transfer kinetics in colloidal suspensions of nanoparticles have not been possible owing to the slow diffusion coefficients of colloidal nanoparticles. As a result, mass transfer limits electrochemical currents as opposed to charge transfer, which operates on a far faster time scale.[109] In photophysical charge transfer studies, the redox active species is either covalently or electrostatically bound to the nanocrystal surface, eliminating any fluxional effects on the observed charge transfer. Given the current resurgence of interest in colloidal nanoparticle photocatalysis for solar fuel production, careful

investigations of the how ligand shell fluxionality affects charge transfer reactions are desirable.[29]

We have chosen to investigate ligand mediated charge transfer processes in alkyl amine functionalized tungsten oxide nanoparticles. Perovskite-like tungsten oxides, WO_{3-x}, $0<x<0.5$, are a material class of current interest due to their interesting optical and electronic properties. The terminal oxide, WO_3, has an indirect bandgap of 2.8 eV and has been investigated by the photoelectrochemical water oxidation community because of its acidic and oxidative stability. While this series of oxides has relatively wide bandgaps which limit their efficiencies, there are potentially ways to tune the bandgap through suitable lattice manipulations, making this material family a possible target photoanode in artificial photosynthetic systems.[110] An important feature of tungsten oxides for this study is the fact that as one moves away from fully oxidized WO_3, oxygen vacancies create free electrons in the conduction band.[111] These appear as a broad plasmonic absorption feature which moves from the near infrared into the visible with increasing carrier concentration (**Figure 3.1**).

We chose alkyl amines to functionalize the tungsten oxide nanoparticles due to their intermediate binding strengths to metal oxide surfaces as well as the lack of inter-ligand reaction pathways, such as anhydride formation in carboxylic and phosphonic acids. To study the ligand mediated charge transfer processes, we employ a well-known spectrophotometric redox indicator, tris(3,4,7,8-tetramethyl-1,10-phenanthroline) Fe^{III} [Fe^{III}(tm-phen)$_3$] to investigate the oxidation of amine passivated $W_{18}O_{49}$ ($WO_{2.72}$) nanorods.[112] The tetramethylated phenanthroline was necessary to operate in a non-polar, well-behaved solvent. This simple oxidation reaction may be tracked by following the production of reduced Fe^{II}(tm-phen)$_3$, which has a characteristic visible absorbance at 510 nm (ε = 11,000 $M^{-1}cm^{-1}$). Conveniently, this extinction sits in an absorption window of the $WO_{2.72}$ nanorods below the bandgap absorption in the UV and above the plasmonic absorption in the NIR. We find that variations in ligand length produce no measurable changes in charge transfer kinetics, as might have been expected if charges were tunneling through a static ligand shell. We also find that increasing amounts of free ligand in solution retard the reaction kinetics. Such observations are consistent with a ligand dissociation mediated charge transfer reaction.

3.2 –Preparation of $W_{18}O_{49}$ Nanoparticles for Charge Transfer

Solubilized colloidal nanoparticle ligand shells are dynamic systems; there is a population of free ligands in solution, in equilibrium with bound ligands on the nanoparticle surface. Such dynamism has serious effects on nanoparticle optoelectronic processes and catalysis.[113,114] $W_{18}O_{49}$ nanorods with varying amine ligand lengths were synthesized following an adaptation of a literature method.[115] In this work, the oxidation of amine functionalized $WO_{2.72}$ nanoparticles by Fe^{III}(tm-phen)$_3$ ($\Delta E_{rxn}=E_{f,WO2.72}-E_{sol}\approx 0.75V$) is studied to understand how the ligand shell of these nanoparticles in solution affects charge transfer.[116] There is an optical density minimum between the band gap (λ < 400 nm) and the visible tail of a broadband plasmon (λ > 500 nm). Such a window makes tracking Fe^{II}(tm-phen)$_3$ production facile and relatively unconvoluted by residual plasmon absorption. An typical charge transfer experiment is shown in **Figure 3.2** – here, spectra are taken at 15 second intervals following an injection of a 20 µL solution of octadecylamine (ODA) passivated $WO_{2.72}$ nanoparticles. One observes a coupled growth in the

$Fe^{II}(tm\text{-}phen)_3$ signal at 510 nm and decay in the broadband plasmon absorption. A walking isosbestic point is observed between 530 and 550 nm as the plasmon extinction diminishes and redshifts as a result of the oxidation.[111,117] This decay in the plasmon extinction is consistent with an oxidation of conduction band electrons.

We note that this reaction is not a simple one electron oxidation. Rather, over the course of the first 1000 s of the reaction, between 75 and 100 electrons are pulled out of each nanoparticle's conduction band (<5% of conduction band electrons, based on the W oxidation states, W

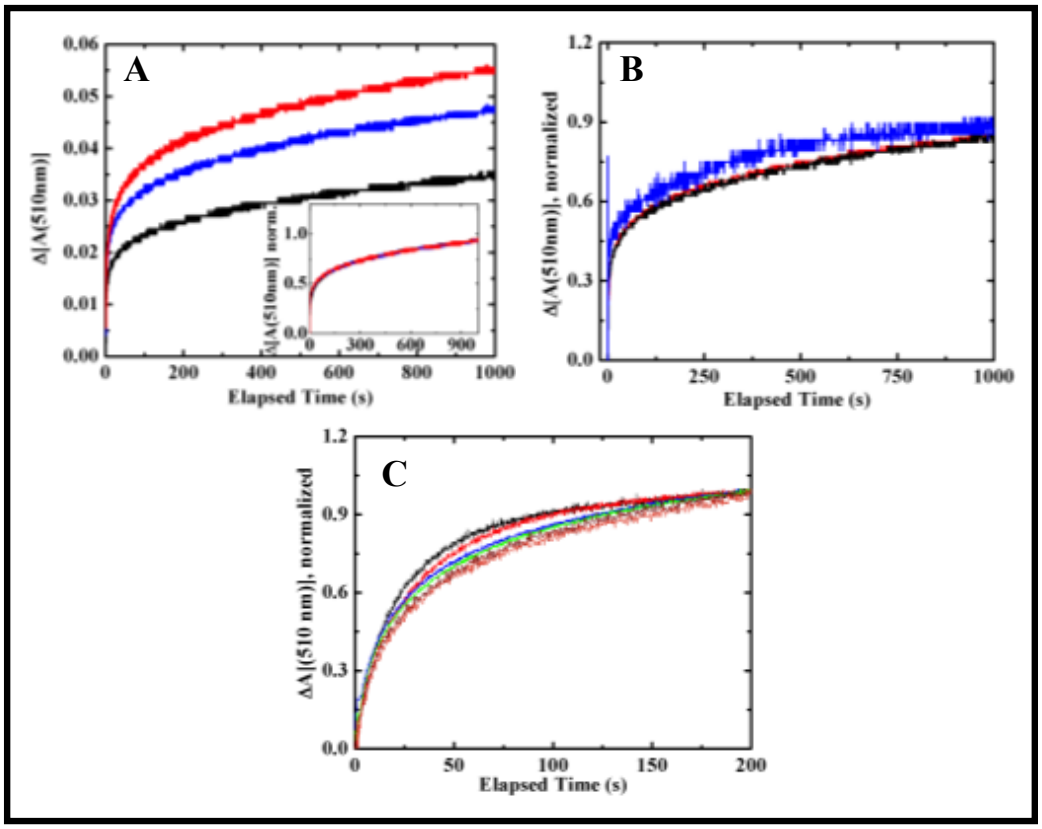

Figure 3.3 - (A) Transients of absorption at 510 nm showing the effects of differing concentrations of $Fe^{III}(tm\text{-}phen)_3$ (red is 100 μM, blue is 150 μM and black is 200 μM). While the number of charges passed changes with concentration, the rate constant does not, as is shown in the inset with transient normalized to 1000 s. Points within the mixing time (0.5 s) have been removed consistently across all samples for clarity. **(B)** Transients of C18 (red) C16 (black) and C14 (blue) alkyl amine passivated $WO_{2.72}$ nanoparticles injected into the standard redox conditions. Transients are normalized to 2000 seconds as a result of differing particle concentrations. One sees no significant dependence of charge transfer rates on ligand length. **(C)** Transients showing the rate dependence on free ligand concentration; standard injection conditions. Black has no added ODA; red, blue, green brown and orange contain 2, 3, 5, 10 and 20 μM ODA, respectively. One sees clearly the retarded rate as a result of added ligand passivating unbound surface sites. Transients have been normalized to

concentrations by ICP-OES and particle dimensions by TEM). The kinetics are complex given the number of electrons – the ΔE_{rxn} is changing as the E_f changes, naturally changing the reaction activation energy and, thus microscopic rate constants. As a result, a quantitative determination of reaction rates is not straightforward as there are both consecutive and parallel reactions proceeding, i.e. there are multiple electrons and the nanoparticles are not exactly the same. The transients do, however, fit well to multiple exponentials with residuals reduced below an acceptable level with >2 exponentials.[23,118] For the present analysis we find it appropriate to observe the qualitative variations in observed reaction rates as functions of ligand variations.

3.3 – Kinetics of Charge Transfer from $W_{18}O_{49}$ Nanoparticles to Solution $Fe^{III}(tm\text{-}phen)_3$

Before interrogating a ligand dependence, it was important to assure that the charge transfer reaction was not limited by $Fe^{III}(tm\text{-}phen)_3$ oxidation kinetics. The $[Fe^{III}(tm\text{-}phen)_3]$ dependence is shown in **Figure 3.3A**. Interestingly, while the number of charges transferred at 1000 s is different across the three concentrations, increasing with increasing starting $[Fe^{III}(tm\text{-}phen)_3]_0$, one sees that upon normalization to 1000 s, the transients overlay. Such an overlay indicates that the same overall rate constant governs these reaction conditions – thus, $Fe^{III}(tm\text{-}phen)_3$ itself does not appear in the rate law, but does however appear in the overall equilibrium constant.

One might hypothesize one of two charge transfer mechanistic regimes – an 'outer sphere', tunneling mechanism as observed in thin film and electrode studies or an 'inner sphere', dissociative mechanism requiring ligand desorption prior to a surface mediated reaction. To test the first hypothesis, a series of $WO_{2.72}$ nanoparticles were made with differing alkyl amine tail lengths (C18, C16, C14 and C12). Were a tunneling mechanism in operation, one would expect

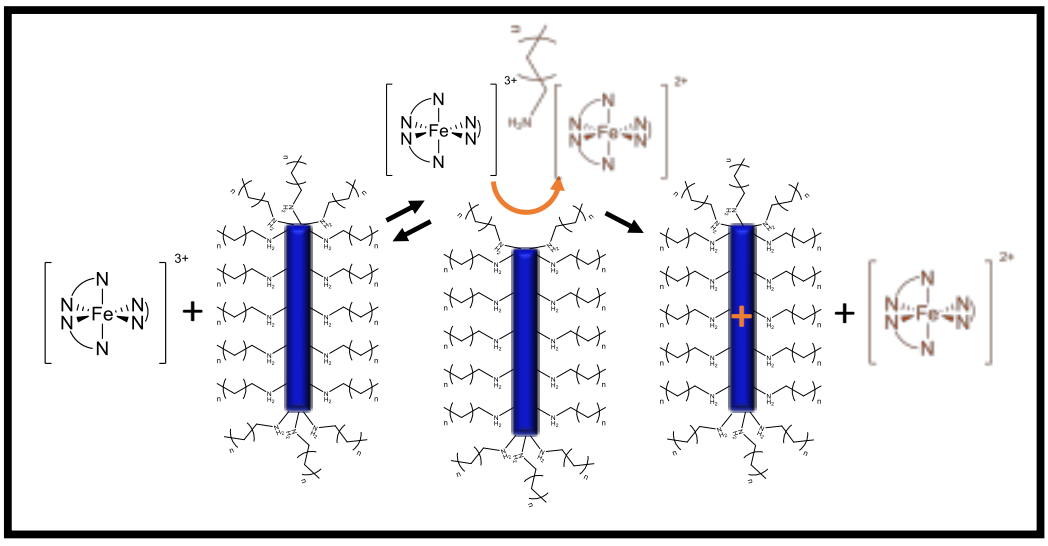

Figure 3.4 – Proposed mechanism of charge transfer at $WO_{2.72}$ nanoparticles. An equilibrium dissociation of amine ligand precedes a rapid oxidation by $Fe^{III}(tm\text{-}phen)_3$ event producing $Fe^{II}(tm\text{-}phen)_3$ and a charged nanoparticle. Addition of excess octadecylamine passivate unbound surface sites, reducing the initial rate of reaction.

an exponential dependence of the observed charge transfer rate constant on ligand length and composition, a ~$1/e^2$ decay in the rate constant per C2 lengthening. As can be observed in the 1000 s - normalized overlay in **Figure 3.3B** (to account for differing concentrations of injected nanoparticle solutions), the transients either overlay, or very nearly do for C18, C16 and C14 amines. C12 and C14 amines were not particularly soluble upon charging, so their transients are either not as clean (C14) or not presented (C12) due to flocculation confounding the absorption spectra. It is apparent that the rate constants are very nearly the same across the series. Such an observation is evidence that a tunneling mechanism is not in effect.

To test for a dissociative, inner sphere mechanism, we titrated in a small amount of ligand to the redox bath solutions. We hypothesized that, if this were the mechanism, there would be an equilibrium number of exposed surface sites through which charge could pass. This number should depend on the free ligand concentration in solution as in a Langmuir or Temkin isotherm.[11] As a result, the initial rate of the reaction should depend on the number of free surface sites, and therefore, on the solution ligand concentration as well. As is shown in **Figure 3.3C**, this is precisely what we observe. With no added ligand, the charge transfer transient is appreciably faster than when small amounts of octadecylamine (ODA) are titrated into the redox bath before the nanoparticle injections. This observation is consistent with the observed oxidation reaction proceeding through uncoordinated surface sites; the more free surface sites, the faster the initial rate of reaction. Addition of excess ligand passivates some free surface sites and slows the initial observed reaction rate.

These results indicate that colloidal nanoparticles pass charge differently than those physically bound to their redox partner – whether an electrode, another quantum dot, nanoparticle or molecule. In systems employing dispersed colloidal nanoparticles for charge transfer reactions, particularly those used in photocatalytic systems, ligand shell fluxionality should be taken into account in attempts to modulate interfacial charge transfer rates (**Figure 3.4**). Such ligand effects have been observed previously in the few examples of colloidal photocatalysis mediated by a homogeneous catalyst, though they have not been rigorously investigated. A recent example is work from Krauss et al. in which dihydrolipoic acid capped CdSe quantum dots showed retarded H_2 production rates with large amounts of excess ligand added during photocatalysis.[30] Given previous observations of ligand coverage obeying a Temkin adsorption model for ligand adsorption, one could envision exploiting ligand binding parameters, such as pK_b, temperature, intermolecular forces and chelate effects, to effectively modulate equilibrium binding coverage at dispersed colloid-solution interfaces.[105,119] Ligand coverage control can then beget control of electron transfer and, in the case of photocatalysis, subsequent catalysis.

3.4 - Conclusion

Employing a redox bath, the diffusion limitations of electrochemical investigations of colloidal charge transfer have been avoided and have allowed for observation of ligand dissociation mediated charge transfer kinetics. While changes in distance between the donor and acceptor via ligand shell modification resulted in no observable changes in charge transfer rates, solution ligand concentrations did. Such an observation implies that the observed oxidations proceeds through a surface interaction rather than the more classically observed tunneling event.

Chapter Four – Quantum Dot Surface Stabilization for Sensitized Water Splitting on TiO_2

4.1 – Methods for Bulk Electrode Corrosion Protection

Photoelectrochemical fuel production relies on efficient oxidation of water to provide electrons and protons for a fuel forming reaction, such as proton reduction to hydrogen or CO_2 reduction to methane.[42,43] When an integrated semiconductor – catalyst photoanode drives the water oxidation, detrimental irreversible photocorrosion reactions on non-oxide semiconductor photoelectrodes compete with water oxidation and threaten device efficiency and lifetime.[50] To avert these corrosion reactions, surface passivation schemes were developed beginning in the 1970's. Because corrosion reactions are thermodynamically favored, semiconductor corrosion protection is a kinetic phenomenon. It relies first and foremost on excluding water contact with a

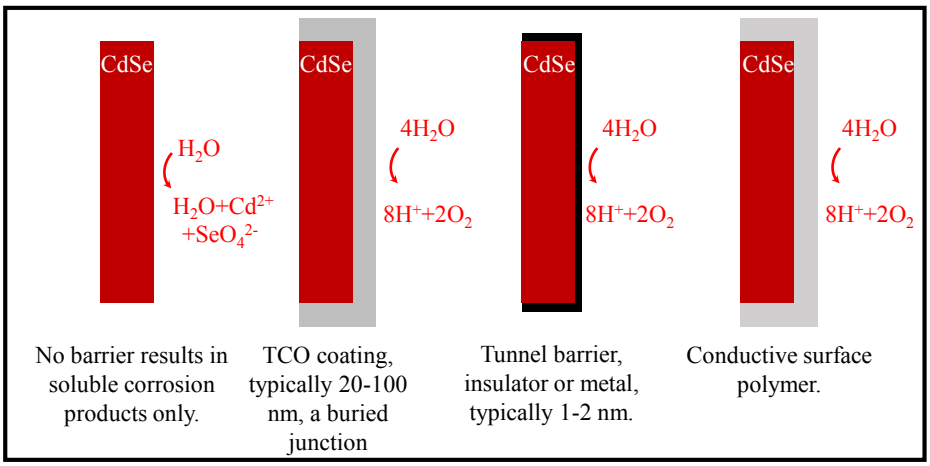

Figure 4.1 – Three general methods for surface protection are shown. Without surface protection, most semiconductors will oxidize their own bonds rather than water. This reaction produces Cd^{2+} and oxidized selenium species. The most common protection scheme uses a dense, conformal and thin transparent conductive oxide (TCO) to block water from the semiconductor surface while allowing light and electrons to transit. Such barriers tend to be 20-100 nm thick. A tunnel barrier uses a conformal insulator layer to block water, allowing charge transfer via a tunneling mechanism. As a result these are extremely thin, these layers are typically only 1-2 nm thick.

device's underlying semiconductor interface to slow the rate of photocorrosion, a process dependent on aqueous dissolution of corrosion products. If such coatings are not conformal and molecularly dense, device corrosion will occur as is shown at left in **Figure 4.1** as large concentrations of surface water will cause the rate of photocorrosion to increase dramatically. In addition to blocking water, this film must also be capable of supporting some amount of interfacial charge transfer between the semiconductor and the electrocatalysts while not completely occluding light. Several general examples of photocorrosion schemes are shown in

Figure 4.1. Dense and thick (20-100 nm) transparent conductive oxide coatings deposited conformally on planar electrodes have been most effective at blocking water while permitting electrons and light to pass through. Such coatings require an ohmic contact to a built in junction as interfacial dipoles are screened by the TCO.[61] These barriers may be deposited using a variety of deposition techniques, but most modern methods rely on RF sputtering or atomic layer deposition. Tunnel junctions relax the requirement for conductivity of the barrier layer, but to pass charge, these barriers must be less than 2 nm. With such processing it is extremely challenging to achieve the necessary conformality at device scales >1 cm^2. A final method relies on a hole conductive polymer coating to passivate and protect the underlying semiconductor surface from water. Most often this layer is a poly-pyrrole surface coating.[120] As these protection methods are designed for bulk, planar electrodes, to be effective they must be perfectly conformal. Any pinholes in the barrier layer will result in corrosion and device loss.

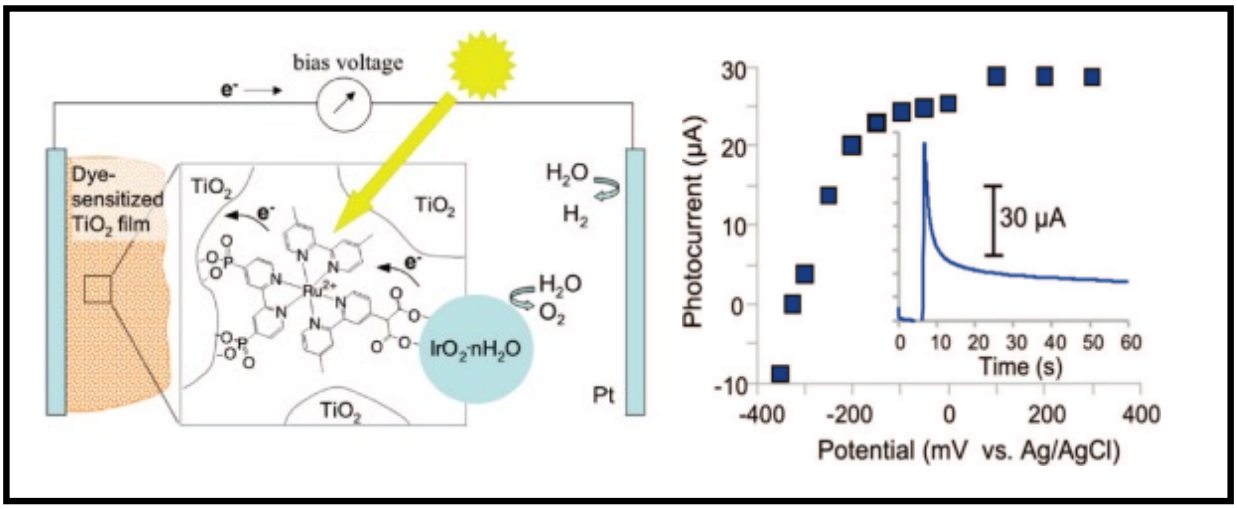

Figure 4.2 – Stepped chronoamperometry (described in detail in **Figure 4.7)** of the dye-sensitized water splitting cell shown at left from Mallouk et al. employing a Ru poly-pyridyl dye and IrO_x nanoparticles.[122] The device shows approximately a 30 μA peak photocurrent along with rapid corrosion.

4.2 – Sensitized Photoelectrochemical Water Splitting

Advances in the surface protection of planar *n*-type photoanodes, such as Si and GaAs, with transparent *p*-type surface coatings, such as transparent conductive oxides or polymers, have enabled impressive and stable photocurrent densities at lab-scale.[59–61,63] Dye-sensitized water splitting devices, on the other hand, have received far less attention.[121] Like dye sensitized solar cells, water splitting devices have a mesoporous TiO_2 electron transporting layer into which an adsorbed dye transfers an excited electron. Instead of transferring the hole to a solution redox couple, the dye oxidizes a nearby water oxidation electrocatalyst, which subsequently oxidizes water, **Figure 4.2**. Sensitized water splitting devices in the literature are typically much less efficient than planar electrodes, **Figure 4.2**. Much of the inefficiency in these devices stems from their high surface areas which enhances the recombination conduction band electrons in TiO_2 with dissolved O_2 as well as dye photoinstability.[122,123]

However, this device architecture presents an extremely appealing advantage to planar electrodes when one considers their corrosion. In bulk devices, protection defects result in device loss; in sensitized architectures, the light absorbers are decoupled such that if one corrodes, its loss does not affect the other absobers. As a result, corrosion does not result in irreversible device loss. In addition, sensitized devices rely on facile solution processing and may be repaired, or 'healed' via resensitization since the underlying $TiO_{2\ is}$ completely stable.

4.3 – QD Sensitized Water Splitting Device Design and Construction

Semiconductor quantum dots (QDs) have been shown as efficient sensitizers in similar constructs to traditional dye sensitized solar cells.[37] In a sensitized construct, QDs offer some intriguing possibilities not readily available to dyes, namely their facile engineering of electron and hole wavefunctions over >5 nm within the particle and straightforward surface chemistry

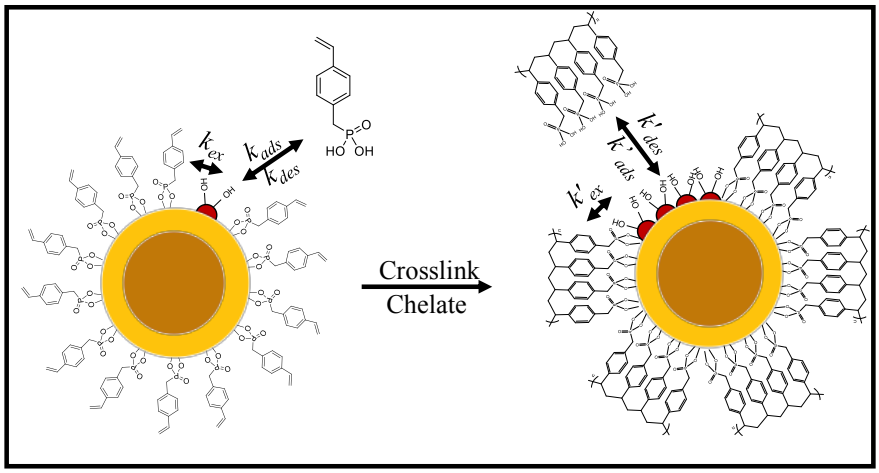

Figure 4.3 – Proposed method of decreasing surface ligand fluxionality by crosslinking ligand tails. As a result of the chelate effect, crosslinked ligands on the right will have far less ligand flux on and off, k'_{ads} and k'_{des}, as well as across the surface, k'_{ex} when compared to their pre-crosslinked rates k_{ads}, k_{des} and k_{ex}. As a result of the decreased fluxionality, surface access to water should be reduced and corrosion reactions should be slowed. Red semicircles represent surface Cd^{2+} sites.

modifications to promote stability.[19,113] Recently, QDs grown by chemical bath deposition have been stabilized with a surface ZnS coating and IrO_x nanoparticles to afford anodic protection and photoelectrolyze water. These results are particularly surprising since ZnS is known to corrode.[51,124] We propose that the surface ligands on a QD can also achieve the main goals of

semiconductor surface protection. As discussed in Chapter 3, ligands bound to surfaces inhibit charge transfer. Since corrosion reactions are charge transfer reactions occurring in the presence of water, surface ligands should be able to limit those corrosion reactions. If one were to design a ligand with an extremely high binding coefficient, those corrosion reactions should be severely

retarded on account of there being very few available surface sites. Furthermore, if one were to crosslink the surface ligands, the number of sites should be further decreased while also limiting the rate of ligand exchange to solution as well as on adjacent sites. Such a systems is shown schematically in **Figure 4.3**. In addition to the surface ligands, one must provide a non-corrosion

charge transfer pathway for the QD's hole. We propose using IrO_x nanoparticles; these are well known water oxidation catalysts and are sufficiently small that they should provide adequate

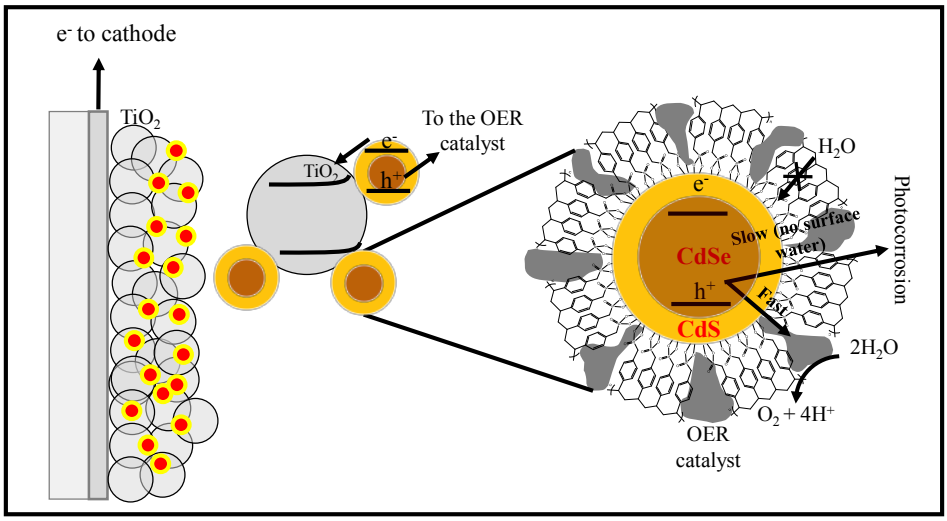

Figure 4.4 – A schematic of the proposed QD sensitized water splitting (QDSWS) device. A core-shell CdSe-CdS QD with a crosslinked ligand shell has been adsorbed on mesoporous TiO_2. Interfacial IrO_x nanoparticles have been adsorbed at exposed QD surface sites to function as water oxidation catalysts. By lowing the surface concentration of water on the QD, charge transfer to the IrO_x catalysts should have an opportunity to compete with corrosion.

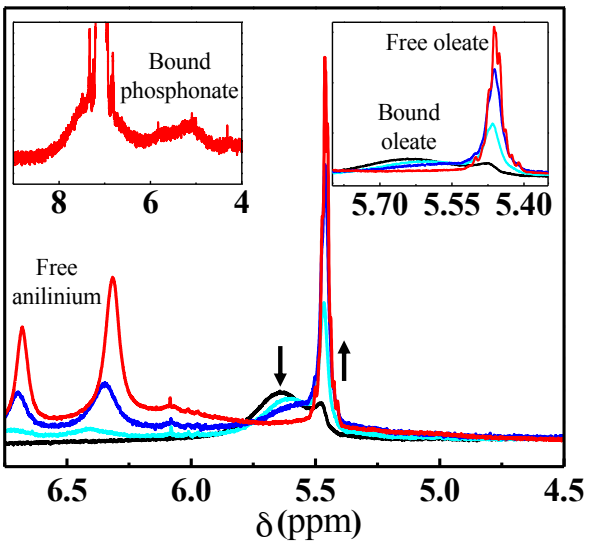

interfacial contact to the quantum dot surfaces.

We present a QDSWS, **Figure 4.4**, that employs a strongly bound, crosslinkable surface ligand, 4-vinyl-benzyl phosphonate in addition to interfacial IrO_x nanoparticle catalysts to combat photocorrosion. By limiting the number of exposed surface sites with a strongly bound, redox inert phosphonate and by putting IrO_x nanoparticles (IrO_x NPs) at exposed, unbound surface sites, we expect photocorrosion reactions to be slower than hole transfer from the CdSe-CdS core-shell QD to the IrO_x NPs.[96,105,107] To achieve this design, we first synthesized the anilinium salt of 4-vinyl-benzyl phosphonic acid **Figure 4.3** using a modified literature preparation.[125,126] Core-shell CdSe-CdS QDs with a pure oleate ligand shell were synthesized using a modified literature prep.[127] Ligand exchange from the oleate to phosphonate proceeded quantitatively at 90°C in toluene-$_{d8}$ as tracked by NMR, **Figure 4.5**.

The typically broad internal olefin resonance from the bound oleate ligands is present in the initial, black spectrum. A small amount of free oleate is still present from cleaning, and appears

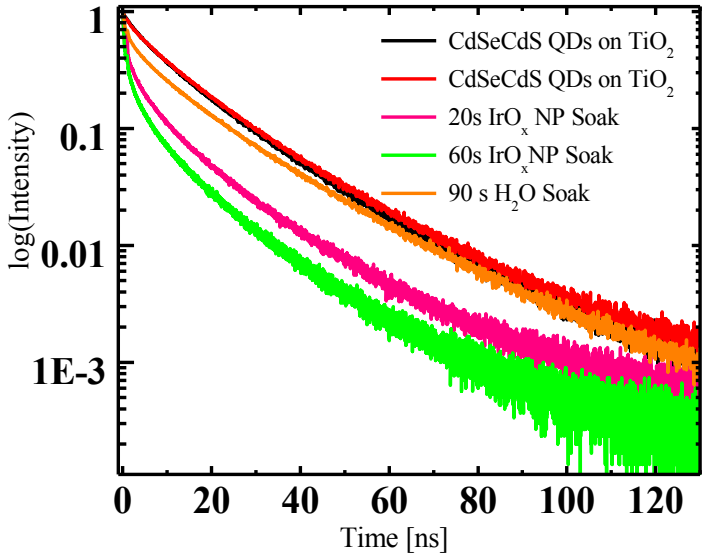

Figure 4.6 – PL lifetime spectroscopy of thickly shelled QD on TiO_2. As the electrodes are soaked in IrO_x NP solutions, the QD photoluminescent lifetimes decrease. IrO_x NP on the QD surface can function as non-radiative traps for electrons and holes generated within the QD. As more IrO_x NPs adsorb on the QD surface, the lifetimes decrease. A simple H_2O soaking control experiment is shown in orange. While some radiative quenching is observed from corrosion induced defects, the effects are not nearly as severe as the IrO_x NP soaking.

styrene phosphonate (red) capped QDs. Note the disappearance of the broad resonance at 5.65 ppm from bound oleate as it collapses into the sharp free oleate at 5.45 ppm as styrene phosphonate is titrated into the sample. A zoomed in spectrum is shown in top right. The top left spectrum shows the effectiveness of the gel permeation column at isolating only phosphonate capped QDs following the ligand exchange. Free anilium is the counterion of the entering phosphonate and departing oleate.

a sharper shoulder at ∂=5.4 ppm. Upon additions of small amounts of phosphonate, the bound

oleate resonance collapses into the free oleate resonance, an indication of exchange, bottom inset.[128,129] After QD purification by gel permeation chromatography, the bound phosphonate appears as extremely broad resonances between 5 and 8 ppm (**Figure 4.5**, top inset) and at 27 ppm in ^{31}P NMR (SI).[130] We attribute the extreme broadness to enhanced spin-spin relaxation

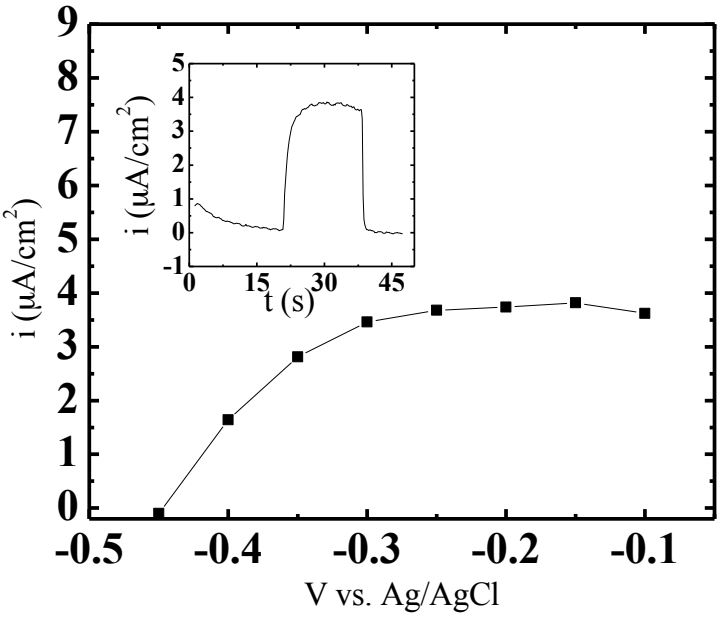

Figure 4.7 – A stepped chronoamperometry experiment similar to that shown in **Figure 4.2**. A QDSWS is stepped out to a voltage, then illuminated and the photocurrent is measured (inset, -0.1 V v. Ag/AgCl). Typical devices exhibit 3-4 μA/cm^2 saturation current densities with -0.45 V v. Ag/AgCl open circuit voltages.

from aromatic ring packing on the QD surface.

We sensitized the mesoporous TiO_2 by a combination of soaking and electrochemical vinyl crosslinking as described previously for vinyl-functionalized Ru(II) polypyridyl dyes.[131] We were unfortunately unable to ascertain the extent of crosslinking of the phosphonates, despite attempts at isolating them via acid digestion and extraction for MALDI-TOF.[113] Because of the degree of surface curvature and the short ligand length, we do not expect a high average M_w. Indeed, there was little to no difference in photoelectrochemical stability between crosslinked and uncrosslinked samples (SI). The observed stabilizing effects simply seem to be a result of the phosphonate's strong surface K_b and redox insensitivity.

IrO_x NP deposition was performed by soaking the sensitized photoelectrodes in a pH 11 NaOH solution of IrO_x NPs for between 1 and 10 minutes. To assess the affinity between the IrO_x NPs and the QD interface, we employed a combination of XPS (SI) and photoluminescent (PL) lifetime spectroscopy (**Figure 4.6**).We synthesized QDs with thick CdS shells so that they maintained some fluorescence upon deposition on TiO_2. Two electrodes were then either soaked in pH 11 water or pH 11 IrO_x NP solutions. Following washing and drying after each soaking

time, PL lifetime spectra were acquired. **Figure 4.6**, shows how IrO_x NPs rapidly quench QD fluorescence. We attribute the slight amount of PL quenching in the water control to aqueous corrosion of the QD surface. This differential quenching implies to us that IrO_x NPs readily deposit at QD interfaces. Developing and maintaining intimate contact between the QD and the IrO_x oxygen evolution catlysts is critical to averting detrimental photocorrosion reactions since hole transfer to the electrocatalysts must be much faster than corrosion. The efficient PL quenching observed for thickly shelled CdSe-CdS QDs demonstrates that hole transfer between the QDs and the IrO_x is indeed quite efficient. In practical devices show in shells are much thinner to support electron injection into TiO_2, typically 1-2 nm as opposed to the 5-6 nm in the quenching study. Full QD characterization and synthesis is presented in the SI.

4.4 – QDSWS Device Characterization and Performance

Because of the high surface area of the mesoporous TiO_2 in these devices, background capacitance currents can occlude much of the small photocurrents in standard cyclic voltammetry. As a result, **Figure 4.7** presents a stepped chronoamperometry experiment for a typical QDSWS photoelectrode. Photocurrent is measured at a variety of potentials between -0.1 and -0.45 V v. Ag/AgCl as individual chronoamperometry experiments. Typical electrodes produce only 3-4 $\mu A/cm^2$ current densities with -0.45 V v. Ag/AgCl V_{OC}. To measure the O_2 produced by these electrodes, we have employed O_2 amperometry. **Figure 4.8** presents a typical

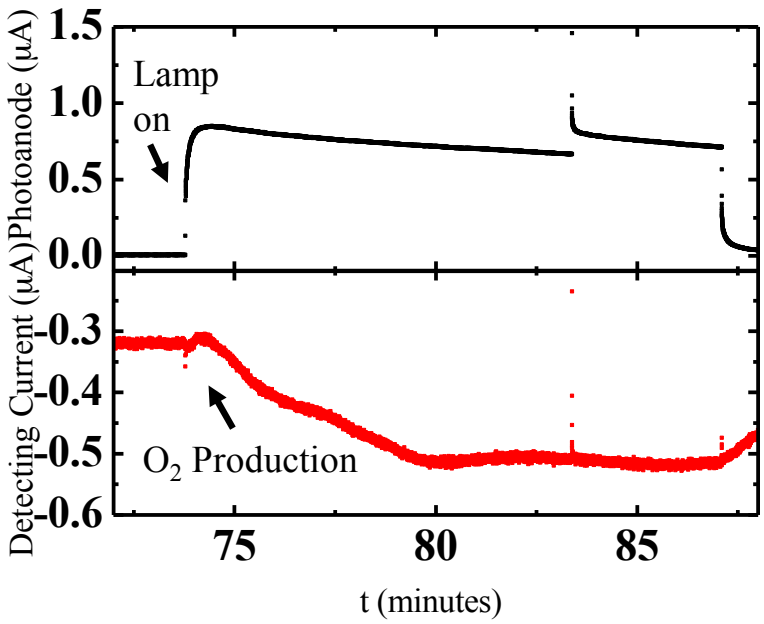

Figure 4.8 – O_2 detection chronoamperometry experiment. Two working electrodes are used, one being the QDSWS photoelectrode and a secone being a Pt on FTO electrode. These two electrodes are placed in a parallel plate geometry with a ~2mm spacing. The Pt detecting electrode is held at -0.4 V vs. Ag/AgCl (pH 13) while the photoelectrodes is held at -0.1V v. Ag/AgCl. Upon illumination after the backrground currents reached steady state, the photoelectrode passes ~1μA current. After about 50 seconds (consistent with H_2O diffusion across 2mm), the Pt cathodic current increases, saturating with a 0.2 μA increase. Such an increase is consistent with O_2 back reduction to H_2O.

chronoamperometry experiment with O_2 detection on a fully functionalized photoanode. In the top panel, a crosslinked QDSWS electrode has been soaked in IrO_x NP as described for 5 minutes. The photoanode is positioned in a parallel plate configuration with a second working Pt electrode for O_2 detection (details in SI).[132] The photoanode is held at open circuit in the dark, while the detecting Pt electrode is held at -0.4V vs. Ag/AgCl. Electrodes were equilibrated under N_2 flow for >1 hr before testing. The detecting electrode (red) has a steady state current of roughly -0.3 $\mu A/cm^2$ from residual backrgound O_2 reduction. Upon illumination (λ>400, 65 mW/cm^2) of the QDSWS, we see approximately 1 $\mu A/cm^2$ current generated at the photoanode (black, this is slightly lower than typical outputs on account of the parafilm wrapping the two electrodes, the current spike at 83 minutes is an artifact due to a voltage step required by the potentiostat programming). O_2 produced on the photoanode must diffuse across the gap between the two electrodes (~2mm) so we see a delay of about one minute between illumination and

detection current onset which is consistent with O_2 diffusion in water.[25] We detect approximately 0.25 μA/cm^2 O_2 reduction current from 0.75 μA/cm^2 photoanodic current. Given the difficulty in assessing precisely the of O_2 detection efficiency (i.e. all the electrode setups have slightly different spacing, angles etc.) the detection serves as a lower bound on O_2 production faradaic efficiency at the photoanode. This experiment indicates that the electrodes operate at >33%

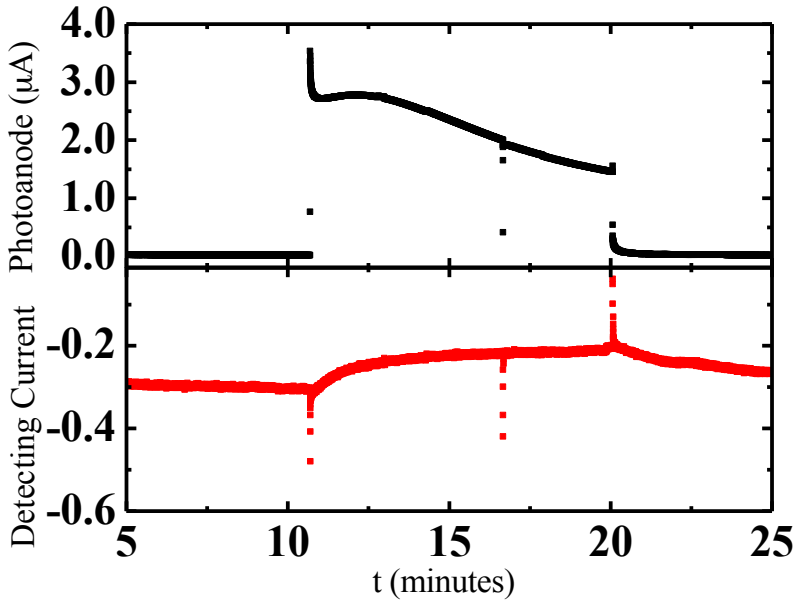

Figure 4.9 – An important control for O_2 detection. In this case, no IrO_x NPs have been deposited on the photoelectrode. As a result, all the observed photocurrent is photocorrosion based. It could be possible that the observed cathodic current increase of the experiment in **Figure 4.6** could be the result of Cd^{2+} or SeO_4^{2-} reduction as opposed to O_2 reduction. Using the same conditions as reported previously, upon illumination, the Pt detecting electrode shows no increase in cathodic current. In fact, there is a significant decrease which may be the result of electrode poisoning by corrosion products.

faradaic efficiency for O_2 production, though the real value is likely higher.

Careful amperometry controls are needed to assure that the observed current increase is a result of O_2 and not some other reaction, such as corrosion product reduction. Full controls are shown in the SI, but **Figure 4.9** shows an important experiment investigating whether corrosion products elicit similar current responses to O_2 reduction. When photoelectrodes without the IrO_x electrocatalysts deposited are illuminated all the current produced on this photoanode will be photocorrosion current yielding the decomposition products of CdSe at pH 13, Cd^{2+} and SeO_4^{2-}.[53] In these experiments, on the detecting Pt electrode, we observe no increased cathodic current. This assures us that the corrosion products are not contributing to the increased faradaic current observed on the O_2 detection Pt electrode during O_2 evolution.

These QDSWS devices do suffer from eventual photocorrosion over the course of several hours, as with other dye sensitized water splitting devices.[122,132] The QDSWS photoanodes may be repaired, however, through simple two step solution processing, re-attaining their initially modest efficiencies along with their O_2 production (SI). In this test, the electrode was partially

corroded over the course of 5 minutes, then re-sensitized as described previously and IrO_x NPs were deposited once again. As one observes, the second iteration once again produces O_2 detection current indicating that 'healing' is indeed possible with these electrodes.

4.5 – Conclusions and Further Optimization

We have reported a QD driven water splitting device that employs strongly bound, ligands to reduce the number of exposed QD surface sites. By adsorbing interfacial IrO_x catalysts on

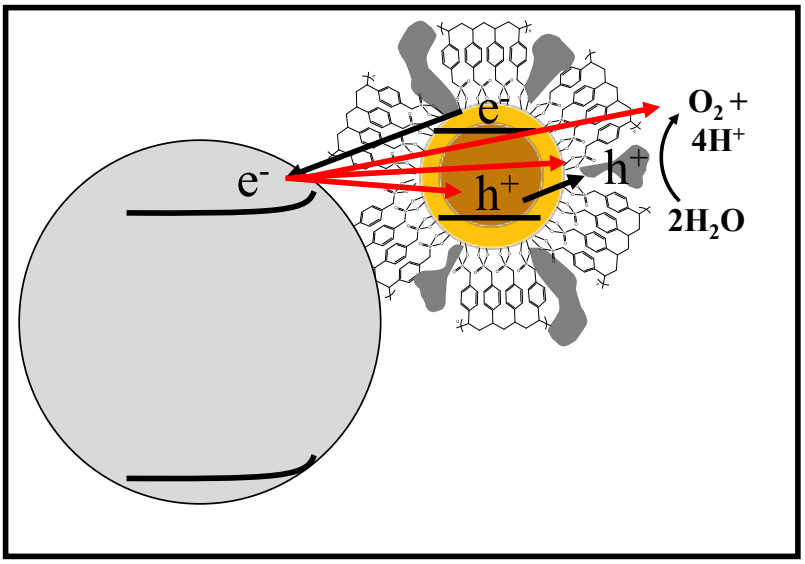

Figure 4.10 – Recombination pathways for an electron in the TiO_2 conduction band. Similar pathways exist for an electron in the QD, but have been omitted for clarity. Decreasing the overlap between the electron and hole wavefunctions through QD heterostructure modifications would decrease these recombination pathways. In addition, faster QD-TiO_2 electron injection via intimate interfacial contact or surface ligand modifications would further serve to decrease electron-hole recombination within the QD.

remaining exposed QD surface sites, these devices successfully avert photocorrosion to produce O_2 from water, the critical step in all solar-to-fuel conversions. We have also demonstrated that , while these devices lose efficiency over time, they may be straightforwardly repaired to re-attain their water splitting capabilities.

Still, these electrodes are not particularly efficient, operating at a small fraction (<1%) of the 10mA/cm^2 necessary to support ~10% solar to hydrogen efficiency. It is likely that the large tunneling barrier imposed by the protecting ligand severely retards electron injection into the TiO_2. While hole transfer to the IrO_x NP may be fast, multiple holes must reside on the catalyst to functionally oxidize water and these provide a rapid recombination pathway for the long lived electrons in the QD and the TiO_2 conduction bands. Building in charge separating heterostructures with more localized OER catalysts would help to mitigate this recombination pathway.[21] In addition, an intimate interface between the light harvesting QD and the TiO_2,

while still accommodating a protecting ligand, could dramatically increase electron injection rates.[32,124]

Appendix – Materials, Methods and Supplementary Information

Chapter 2

Spectroscopic Techniques

UV-Vis emission spectra were taken on an ISA Instruments Triax 320 spectrometer and absorption on an Agilent 8453 spectrometer. ICP-OES was performed on a Perkin Elmer 5300 DV optical emission ICP with an auto sampler. Samples were digested in concentrated HNO3. XPS measurements were taken on an in-house ultra-high vacuum system using an Al Kα 1486.600eV source at 14kV from a Physical Electronics PHI 5000C ESCA high voltage system and a Physical Electronics AMP/DESCRIM CCD detector.

Powder XRD was performed at the Advanced Light Source beamline 12.3.1. Electron microscopy was performed Tecnai G2 200 kV microscope outfitted with a Gatan CCD. HRTEM was performed on the 200kV FEI monochromated F20 UT Technai with a Gatan CCD at the National Center for Electron Microscopy.

X-ray absorption data collection

X-ray absorption data were collected at the Stanford Synchrotron Radiation Lightsource (SSRL) on beamline 7-3 at an electron energy of 3.0 GeV with an average current of 300 mA. The radiation was monochromatized by a Si(220) double-crystal monochromator. The intensity of the incident X-ray was monitored by an Ar-filled ion chamber (I0) in front of the sample. Samples were diluted in boron nitride (1% w/w) and placed in an aluminum sample holder sealed with kapton tape. Data were collected as fluorescence excitation spectra with a Ge 30 element detector (Canberra). Energy was calibrated by the first peak maximum of the first derivative of a molybdenum foil (20003.9 eV), placed between two Ar-filled ionization chambers (I1 and I2) after the sample. All data were collected at room temperature. Model compounds were commercially available: $(NH_4)_2[MoS_4]$ (Aldrich 99.97%), MoS_2 (Cerac Specialty Inorganics 99%) and MoS_3 (Alfa Aesar) were measured (Fig S2.3).

Synthesis

All materials and reagents were purchased from Sigma Aldrich, Alfa-Aesar, PCI Synthesis Inc. or Strem Chemicals and were used as received. Air-sensitive materials were handled in an Ar(g) glovebox and were utilized employing standard air-free Schlenk line techniques. All CdSe seeded and unseeded CdS nanorods were prepared according to the work of Carbone et al.[17] After cleaning, the nanoparticle solutions were stored in toluene in an Ar(g) filled glovebox at roughly micromolar (with respect to number of rods) concentrations. Exact concentrations of each stock solution were determined using a combination of ICP-OES and TEM, specifically by dividing the ICP-OES measured Cd^{2+} content in a given aliquot by the number of Cd ions per rod. UV-vis absorption spectroscopy proved unreliable for determining particle concentration as nanoparticle molar extinction coefficients are shape dependent, making Yu et al.'s[133] work

inapplicable. Furthermore that work reports on single component cadmium chacogenide dots, while this work concerns seeded rods. The number of Cd^{2+} ions per nanorod was calculated using the average size as given by TEM then dividing that by the dimensions of a wurtzite unit cell and multiplied by two. The surface area of a nanorod was calculated from appropriate weights of the unit cell surface areas of the <1100> and <0001> faces of wurtzite CdS depending on rod aspect ratio. To get the number of available surface sites we multiplied the number of surface exposed unit cells by 2 given there are 2 Cd atoms per unit cell that can be exposed.

A typical MoS_3 deposition was conducted by heating a solution of nanorods in toluene, $(NH_4)_2[MoS_4]$ dissolved in *N*-methylpyrrolidone (NMP) and *o*-dichlorobenzene (*o*-DCB) with a CEM Explorer Laboratory Microwave for 50 minutes at 90ºC. The ratios of rods to $(NH_4)_2[MoS_4]$ were varied to obtain increasing surface coverage from A to D as reported in Table 1. This ratio of Mo:Cd depends on the amount of $(NH_4)_2[MoS_4]$ dissolved in the reaction mixture during the thermal deposition, but does not scale linearly with the quantity added, indicating that the deposition of Mo is self-limiting under these conditions. The bright orange solution changes to a brown color characteristic of MoS_3 following the heat treatment. The nanoparticles were then centrifuged from solution at 14,000 RPM for 5 minutes. The supernatant was decanted and the pellet was resuspended in acetonitrile by sonication. The centrifugation and resuspension was repeated once more to remove solution based molybdenum ions as well as displaced phosphonic acid ligands.

Table S2.1. Experimental parameters for the thermal deposition of MoS_3 with microwave heating. Seeded rods in toluene were added to *o*-DCB such that the combined volume was 0.36ml, followed by an aliquot of 25mg/ml $(NH_4)_2[MoS_4]$ in *N*-methylpyrrolidone. From A to D, the amount of $(NH_4)_2[MoS_4]$ increases.

Seeded Rods in Toluene			**Volume of *o*-DCB (µl)**	**25mg/ml (NH4)2[MoS4] in NMP (µl)**			
Seed Diameter (nm)	**Length (nm)**	**Volume (µl)**		**A**	**B**	**C**	**D**
2.6	62	36.3	324	9.3	18.6	27.9	37.2
2.8	60	42.2	318	9.0	18.0	27.0	36.0
2.8	92	44.2	316	13.8	27.6	41.4	55.2
2.8	42	61.8	298	12.6	18.9	25.2	31.5
3.6	68	49.8	310	10.3	20.6	30.8	41.1

Photocatalysis and Gas Chromatography

Gas chromatography was performed on a Varian GC 4900 micro gas chromatograph calibrated to an Ar flow rate of 10 ml/min. The illumination source was a Newport Model 67005 Hg/Xe 50-500 W DC arc lamp outfitted with a (Newport 10BPF70-450) 450 nm bandpass filter. Incoming power at the square-faced quartz cell was held constant at 40 mW·cm-2, on the order of about 1000 photons·rod-1s-1. We assume all incident light is absorbed, since no photon flux was measured at the back of the cell, though some light is lost by scattering. Following cleaning, 0.05-0.1 nmol of MoS_3 functionalized nanoparticles were spun down and resuspended in [0.1] M pH 7.0 Tris-base buffered water (typically 5 mL) for photocatalytic measurements. 0.2 mL

triethanolamine was added to function as a sacrificial reductant. This solution was then added to a custom built, square-faced quartz cell outfitted with Swagelok® fittings connected to the gas chromatograph. The stirring solution was purged with Ar until no N_2 or O_2 were detected in the chromotagrams. The solution was then illuminated with 450±35 nm filtered light and H2 production monitored by analyzing aliquots from a continuous flow of Ar through the photocatalysis cell with a gas chromatograph (typically every 8-10 minutes). Following testing, the precise amount of Mo and Cd present in each sample was determined using ICP-OES by immediately spinning down the reaction mixture and separating the supernatant and pellet.

Data reduction and analysis

Data reduction of the EXAFS spectra was performed using EXAFSPAK (Drs. Graham George and Ingrid Pickering, SSRL). Pre-edge and post-edge backgrounds were subtracted from the XAS spectra, and the results were normalized with respect to edge height. Background removal in k-space was achieved through a four-domain cubic spline. Curve fitting was performed with Artemis software using *ab initio*-calculated phases and amplitudes from the program FEFF 8.2.[90,92] These *ab initio* phases and amplitudes were used in the EXAFS equation:

$$\chi(k) = S_0^2 \sum_j \frac{N_j}{kR_j^2} f_{eff_j}(\pi,k,R_j) e^{-2\sigma_j^2 k^2} e^{-2R_j/\lambda_j(k)} \sin(2kR_j + \phi_{ij}(k)) \quad (1)$$

The neighboring atoms to the central atom(s) are divided into *j* shells, with all atoms with the same atomic number and distance from the central atom grouped into a single shell. Within each shell, the coordination number N_j denotes the number of neighboring atoms in shell *j* at a distance of R_j from the central atom. $f_{eff_j}(\pi,k,R_j)$ is the *ab initio* amplitude function for shell *j*, and the Debye-Waller term $e^{-2}\sigma_j^2 k^2$ accounts for damping due to static and thermal disorder in absorber-backscatterer distances. The mean free path term $e^{-2}R_j/\lambda_j\ (k)$ reflects losses due to inelastic scattering, where $\lambda_j(k)$ is the electron mean free path. The oscillations in the EXAFS spectrum are reflected in the sinusoidal term, $sin(2kR_j + \phi_{ij}(k))$ where $\phi_{ij}(k)$ is the *ab initio* phase function for shell *j*. S_0^2 is an amplitude reduction factor due to shake-up/shake-off processes at the central atom(s). The EXAFS equation was used to fit the experimental data using *N*, *R*, and the EXAFS Debye-Waller factor (σ^2) as variable parameters. For the energy (eV) to wave vector (k, $Å^{-1}$) axis conversion, E_0 was defined as 20010 eV and the S_0^2 value was fixed to 0.84.[88] EXAFS curve-fitting procedures and the estimation of the uncertainty in the parameters from the fits are described in detail below.

Curve Fitting procedure

The curve fitting results for the Mo EXAFS data from MoS_3 and the Mo-rods before and after catalysis are summarized in Table S2. As a goodness-of-fit index, we used the R-factor (the absolute difference between theory and data), which is defined as the sum of the squares of the differences between each experimental point and the fit normalized to the sum of the squares of the experimental points.[91] For the compound MoS_3, the curve fitting was carried out using distances and coordination numbers obtained in previous publications.[88,89] The parameters

obtained for MoS_3 curve fitting are similar to those obtained by Cramer et al.[89] For Mo-functionalized rods before and after catalysis fittings, we proceeded as follow:

- Fit #1: The coordination numbers were fixed to 6 and 1 for Mo-S and Mo-Mo shells, respectively, while the σ^2 values were left free.
- Fit #2: The coordination numbers were left free, while the σ^2 values were set to those determined in the MoS_3 fitting.
- Fit #3: The coordination number of the Mo-S shell and the σ2 values were left free.

Results

For both Mo-coated rods before (BC) and after catalysis (AC), the best R-factors were obtained for fit #3. In the case of Mo-rod BC, the coordination number for the Mo-S shell is close to the theoretical value of 6, and the Mo-S and Mo-Mo distance are almost identical to those observed for MoS3. The first peak intensity of the FT-EXAFS (Fig. S3b) is stronger and the Debye-Waller factors for Mo-S interactions are somewhat smaller than the value obtained for MoS3, suggesting slightly ordered distances on the rods than in the bulk.

In the case of Mo-rod AC, the coordination number for the Mo-S shell tends to be smaller (N=~3) than the value expected for MoS3 (N=6). A decrease in the Mo-S distance of about 0.1 Å is also observed, while the Mo-Mo distance remains identical. The decrease in Mo-S coordination number and distance may suggest the reduction and protonation of the disulfur bridge present in the MoS_3 motif to form a dihydrosulfido bridge between two molybdenum centers.

Table S2: Mo EXAFS fitting results obtained for MoS_3 and the Mo-coated rods before (Mo-rod BC) and after (Mo-rod AC) catalysis.‡*

Sample	Fit #	Shell	N (±)	R/Å (±)	σ2/Å (±)	R-f/%
MoS3	1	Mo-S	**6**	2.42 (0.02)	0.010 (0.002)	14.8
		Mo-Mo	**1**	2.76 (0.02)	0.004 (0.002)	
Mo-rod BC	1	Mo-S	**6**	2.44 (0.01)	0.008 (0.001)	2.0
		Mo-Mo	**1**	2.78 (0.02)	0.003 (0.002)	
	2	Mo-S	6.3 (0.6)	2.44 (0.02)	**0.010**	3.8
		Mo-Mo	1.3 (0.5)	2.78 (0.02)	**0.004**	
	3	Mo-S	5.0 (0.6)	2.44 (0.01)	0.005 (0.001)	1.4
		Mo-Mo	**1**	2.78 (0.02)	0.004 (0.002)	
Mo-rod AC	1	Mo-S	**6**	2.36 (0.04)	0.014 (0.003)	11.0
		Mo-Mo	**1**	2.75 (0.04)	0.003 (0.003)	
	2	Mo-S	4.1 (0.5)	2.35 (0.02)	**0.010**	5.2
		Mo-Mo	1.2 (0.4)	2.75 (0.02)	**0.004**	
	3	Mo-S	3.1 (0.5)	2.35 (0.01)	0.005 (0.002)	2.3
		Mo-Mo	**1**	2.76 (0.02)	0.003 (0.002)	

‡ Bold numbers are set parameters.
* The amplitude reduction factor S_0^2 was set to 0.84.

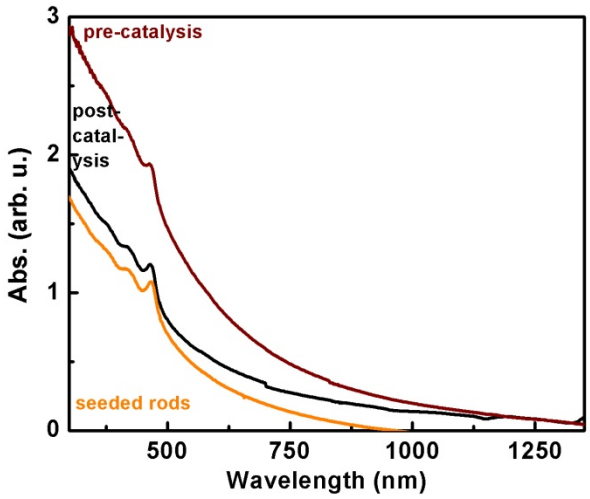

Figure S2.1. UV-Vis spectra of the as-synthesized seeded rods (yellow), rods functionalized with MoS_3 before (burgundy) and after (black) catalysis. All the spectra were taken in water. The excitonic features of the nanocrystals are maintained, indicating no etching of the nanorod during MoS_3 deposition or photocatalysis. No absorption features associated with MoS_2 are seen.

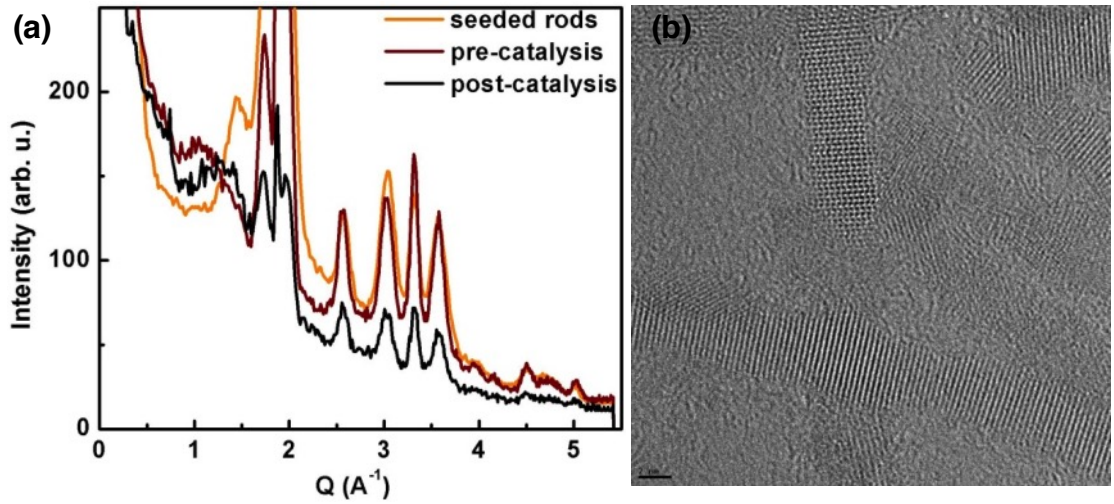

Figure S2.2. (a)Powder XRD of the as synthesized rods (yellow), rods functionalized with MoS_3 (burgundy), and MoS_3 functionalized rods after being subjected to photocatalytic conditions (black). No diffraction peaks associated with a crystalline molybdenum sulfide species are observed. (b) HRTEM of MoS_3 functionalized rods showing lattice fringes only associated with CdS.

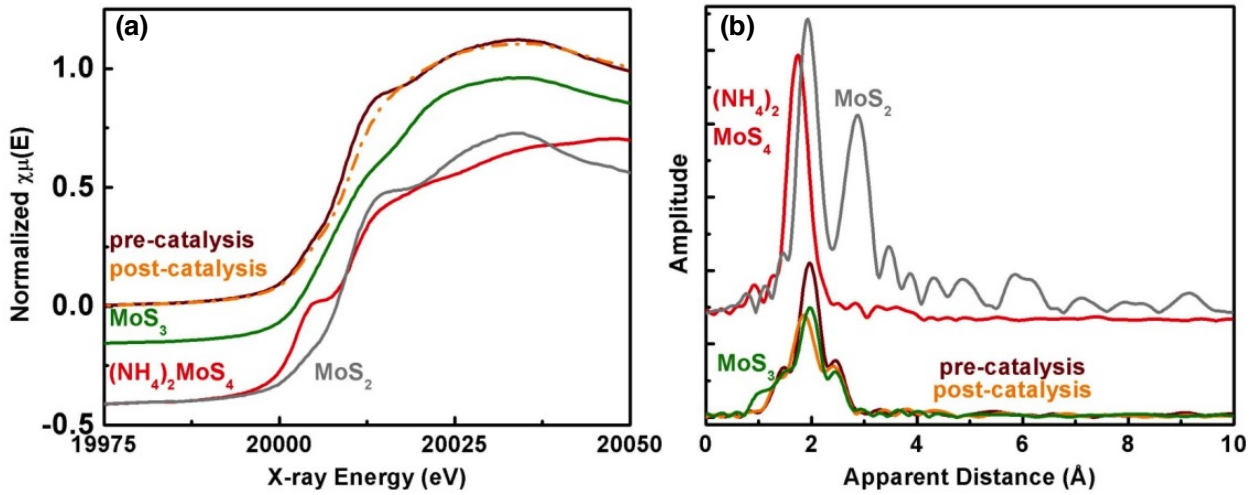

Figure S2.3. XANES and EXAFS at the Mo K-edge with the model compounds, crystalline MoS_2 (grey), $(NH_4)_2[MoS_4]$ (red), MoS_3 (olive) and MoS_3 functionalized nanorods before (burgundy) and after (orange) catalysis.

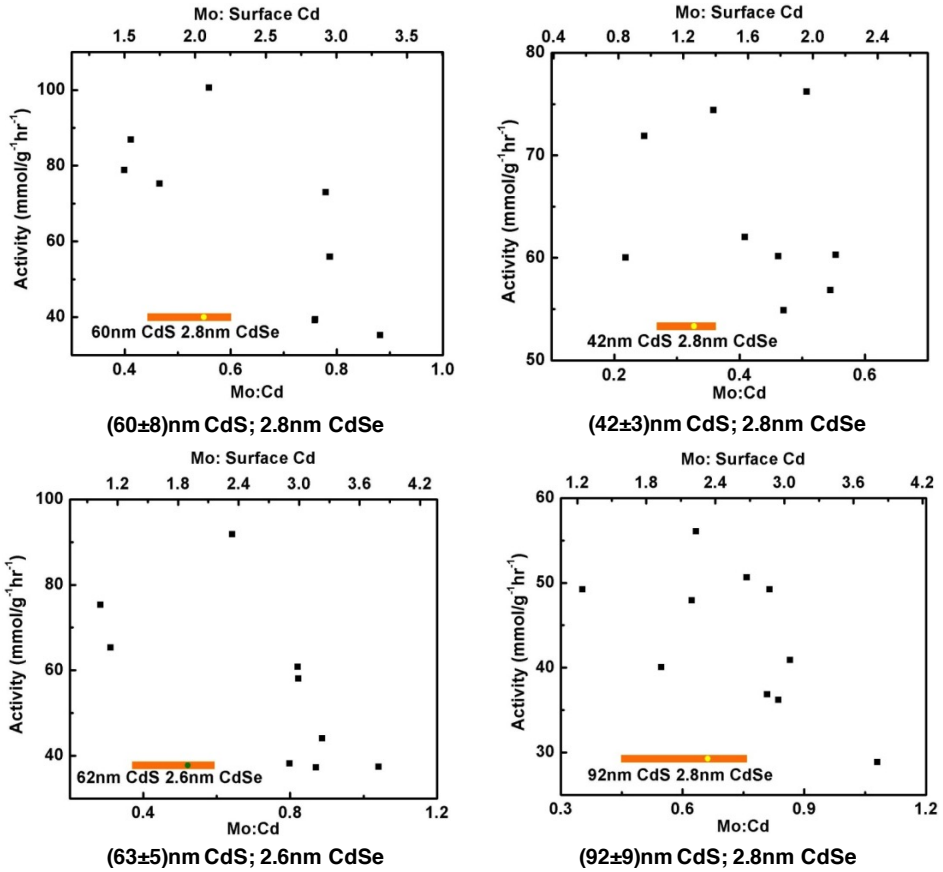

Figure S2.4. Activity vs absolute Mo:Cd ratio (bottom y-axis) and Mo: surface Cd (top y-axis) for all the seeded rods used in the photocatalysis experiments. The highest activity is obtained for Mo: surface Cd ~ 2:1.

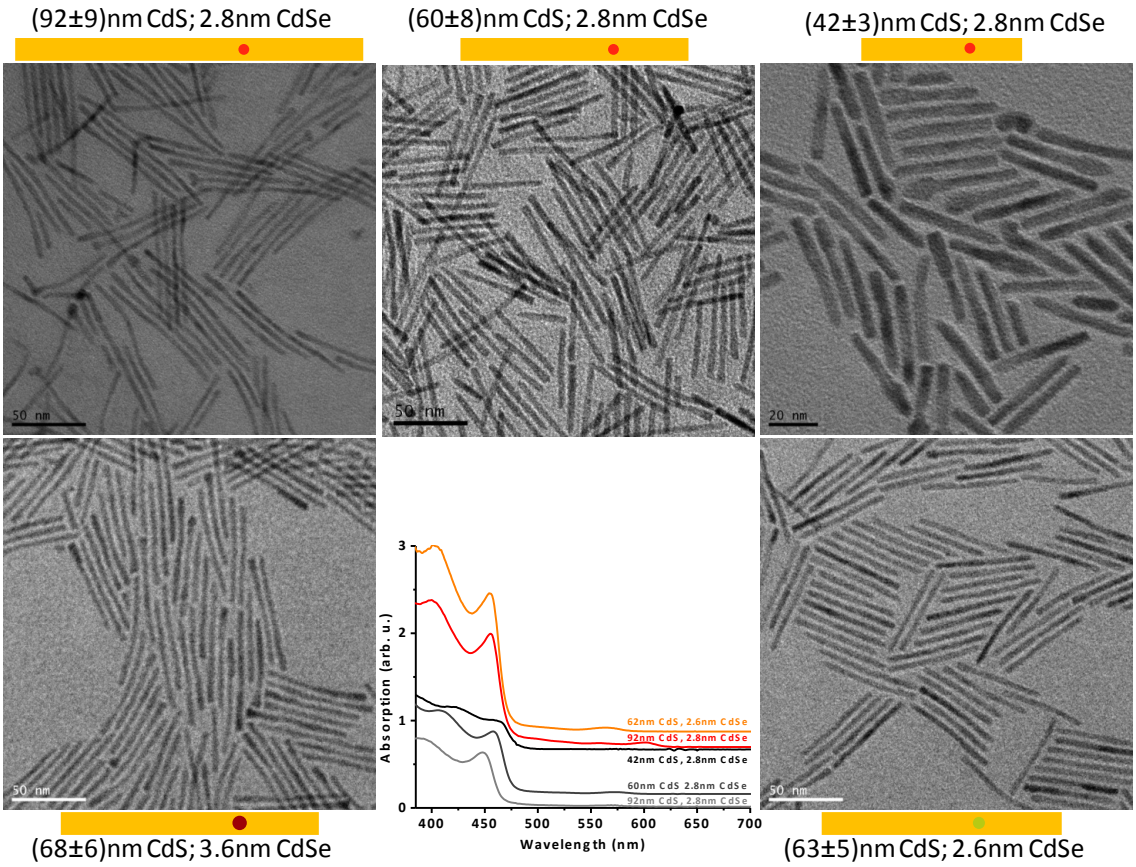

Figure S2.5. TEM and UV-Vis of the seeded rods functionalized with MoS_3 used for the photocatalytic production of hydrogen.

Chapter 3

Materials and Methods - Octadecylamine (97%), hexadecylamine (99%), tetradecylamine (96%), dodecylamine (99%), 1-octadecene (90%), trimethylamine-N-oxide·$2H_2O$ (99%), $FeCl_3 \cdot 6H_2O$ (97%), 3,4,7,8-tetramethyl (1,10-phenanthroline) (99%) and chloroform (spec. grade) were purchased from Sigma Aldrich and used as received. Solvents employed in purification were purchased from Fischer Scientific as HPLC grade. $W(CO)_6$ (97%) was purchased from Alfa Aesar and sublimed. Tetrabutylammonium hexafluorophosphate (TBA-PF_6, 99%) was purchased from Alfa Aesar and used as received.

$W_{18}O_{49}$ nanorods with varying amine ligand lengths were synthesized following an adaptation of a literature method.[115] In a typical synthesis, $W(CO)_6$ (350 mg, 0.99 mmol) trimethylamine-N-oxide (663 mg, 5.97 mmol) and the desired amine (5.97 mmol) were mixed with 10 mL 1-octadecene in a round bottom flask fitted with a distillation column to prevent run-away foaming during decarbonylation. An oil bubbler was fitted to the glassware and, over the course of an

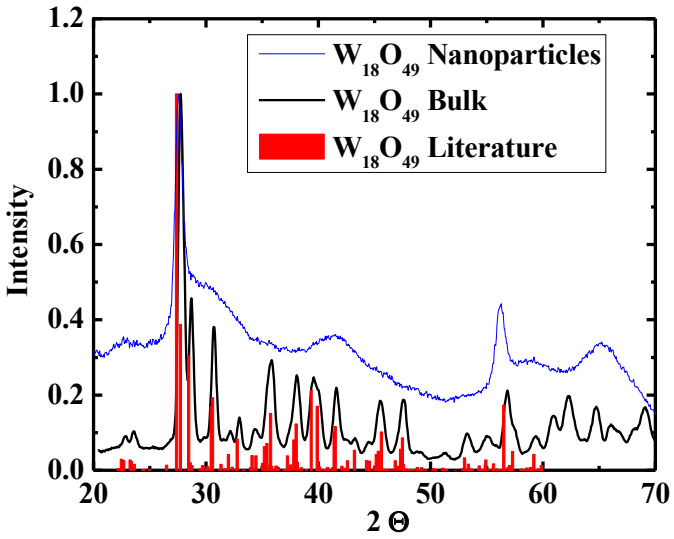

hour, the reaction was slowly brought up to 270°C in an oil bath. During heating, vigorous frothing is observed between 60 and 120°C and the reaction proceeds through a series of color changes before settling on deep blue near the final reaction temperature. The flask is held at 270°C overnight after which it is cooled to room temperature. A mixture of ethanol (200°) and acetone is used to precipitate the particles. After centrifugation, the dull brown supernatant is discarded and the blue particle pellet is resuspended in chloroform, precipitated with methanol and centrifuged at 4000 rpm. This process is repeated until the supernatant maintains a clear, blue color, typically 4-6 cycles. The particles are then stored in spec. grade chloroform. $W_{18}O_{49}$ ($WO_{2.72}$) phase purity was confirmed with x-ray diffraction.

Figure S3.1. Powder XRD of the $WO_{2.72}$ nanoparticles (blue). The nanoparticle XRD shows the expected broadening from the small crystallite sizes. Sharp reflections at 27° and 56° are results of the preferential growth along the rod's <010> direction. Bulk $WO_{2.72}$ was prepared as

described by sintering WO_3 and W in appropriate molar ratio (1 WO_3 : 0.06 W) to produce $W_{18}O_{49}$. The powders were ground to homogenize and charged to an evacuated quartz tube. Purple needles of $W_{18}O_{49}$ were isolated after 40 hours at 950°C.

Redox electrolyte solutions for charge transfer studies consisted of 100 mM TBA-PF_6, 100 μM $Fe^{III}(tm\text{-}phen)_3$. $Fe^{III}(tm\text{-}phen)_3$ was prepared by mixing stoichiometric amounts of $FeCl_3$ and 3,4,7,8-tetramethyl-(1,10-phenanthroline) in spec. grade chloroform with the appropriate amount of supporting electrolyte. Complexation was allowed to come to equilibrium overnight. Solutions were stable over the course of several weeks when stored at room temperature in the dark.

Kinetic traces were acquired on an Ocean Optics USB2000 UV-vis spectrometer at 60 ms intervals. A rapidly stirred cuvette allowed for mixing times to be consistently ~1 s. Detailed UV-vis spectra were acquired on a Shimadzu UV 3600, TEM images were acquired at 200 kV on an FEI G20 20 Tecnai microscope, and ICP-OES data was acquired on a Perkin Elmer Optima 4300 on the W 207.912 nm line with a series of five, one-half dilutions. X-ray diffraction patterns were acquired on a Bruker D8 GADDS Discover diffractometer with Co Kα radiation.

Chapter 4

Materials –
Triethylphosphite (99%, Sigma Aldrich, [SA]), (*β*-chloroethyl)benzene (99%, SA), Zinc chloride (>98%, SA), Paraformaldehyde (Reagent grade, Fisher), Bromotrimethylsilane (97%, SA), Tri-n-octylphosphine oxide (99%, Strem Chemicals), Oleic Acid (Tech. Grade., SA), 1-Octadecene (Tech. Grade. SA), Cadmium Oxide (99.99+%, SA), Selenium powder (99.9 Baker and Adamson), Sulfur (Sublimed, Fisher Scientific), Tri-n-butylphosphine (97%, Strem Chemicals, d8-Toluene (Cambridge Isotopes, 99.5% D), Isopropanol (HPLC Grade, Fisher Sci.), Methanol (HPLC, Fisher Sci.), Hexanes (HPLC, Fisher), Toluene (HPLC, Fisher), Acetone (HPLC, Fisher), Tetrahydrofuran (>99%, Ultra-Dry, Acros Organics), Tetrabutylammonium hexafluorophosphate (>99% Electrochemical Grade, SA), Conc. Nitric Acid (Fisher), Potassium hydroxide (reagent grade, Fisher), Potassium hexachloroiridate (Ir 39% min., Alfa Aesar), Potassium tetrachloroplatinate (99.99%, SA), Titanium isopropoxide (99%, SA), Hydroxypropyl cellulose M_W=80,000 (99%, SA), Glacial Acetic Acid (Fisher), K_2IrCl_6 (Alfa Aesar, min. 39% Ir). d8-toluene was distilled over sodium and benzophenone prior to use. All other materials were used as received.

Instrumentation-
UV-Vis absorption spectra were acquired on an Agilent 8453 Diode Array Spectrometer, emission spectra were acquired on a Fluorolog Triax 320, photoluminescent lifetimes were acquired on a PicoQuant FluoTime 300 single photon counting spectrometer. TEM was performed on a Tecnai G2 at 200kV. SEM and EDS were acquired on an FEI Quanta FEG 250. XPS was acquired on a Kratos Ultra XPS using a monochromated Al anode at 15kV. All NMR spectra were acquired on a Bruker Avance 400 MHz magnet. Three electrode measurements were conducted on a CH Instrument 600E potentiostat, four electrode measurements were conducted on a CH Instruments 760E bipotentiostat.

TiO_2 Electrode Preparation-
FTO coated glass electrodes (SA, 13Ω/cm^2) were sonicated for 20 minutes in isopropanol, another 20 minutes methanol and dried in a 110°C oven. TiO_2 paste was prepared and stored as described elsewhere.[134] 3-5 μm layers were spread using the doctor blade method, dried in air for 1 hr, then calcined at 500°C for 1 hour with 1°C/minute heating and cooling ramps. Copper wire was then contacted to the electrodes with silver paste and sealed with Hysol-1C. TiO_2 electrode areas were cut to 1 cm^2.

Photoelectrochemical Characterization-
All photoelectrochemical measurements were performed in MilliPore Water (>18MΩ/cm) at pH13 (01.M KOH). The illumination source was a 150W Xenon lamp with water and 400 nm long pass filters. Illumination power at the chamber face was 85 mW/cm^2. Three and four electrode measurements were made with a Pt mesh counter electrode and Ag/AgCl (3.5M KCl) reference electrode. Three electrode measurements were conducted on a CH Instrument 600E potentiostat, four electrode measurements were conducted on a CH Instruments 760E bipotentiostat.

The synthesis of anilinium 4-vinyl-benzylphosphonate was performed following a modification of literature preparations.[125,135]

4-*β*-chloroethyl-benzylchloride (1). (*β*-chloroethyl)benzene (100 g, 0.711 moles), ZnCl (14.2 g, 0.104 moles), paraformaldehyde (20.4 g, 0.679 moles), and CS_2 (40 mL) were added to a 250 mL round bottom flask equipped with a reflux condenser. In a separate 250 mL round bottom flask, concentrated H_2SO_4 was added dropwise to ~100g of NaCl to produce gaseous hydrochloric acid. This was then bubbled into the reaction solution via das diffuser and the solution was subsequently heated at reflux (70 °C) for 72 hrs. The reaction solution was then extracted with dichloromethane twice, washed once with saturated $NaHCO_3$, once with saturated NaCl, dried over $MgSO_4$ and the solvent removed *in vacuo*. The crude product was purified via fractional vacuum distillation, which removed starting material at 35 - 45 °C, and a mixture of *para* and *ortho* products (3:1 ratio) at 80 - 110 °C (500 mTorr). A recrystallization from hexanes produced pure **1** (31.76 g, 0.168 moles) to give an overall reaction yield of 23%. Colorless crystals. ^{1}H NMR ($CDCl_3$, 400 MHz) δ 7.36-7.21 (m, 4H), 4.58 (s, 2H), 3.71 (t, J=7.4, 2H), 3.07 (t, J=7.2, 2H). m/z = 188.0161 (calc. = 188.0160).

diethyl-4-*β*-chloroethyl-benzylphosphonate (2). Compound **1** (31.76 g, 0.168 moles) and triethyl phosphite (41.87 g, 0.252 moles) were loaded into a 100 mL round bottom flask equipped with a reflux condenser and were purged under argon. The reaction solution was then heated to 140 °C for 28 hrs. The flask was then cooled to room temperature and equipped with a distillation head. A fractional vacuum distillation was then performed, removing triethyl phosphite from 20 - 50 °C, **1** from 60 - 100 °C, and **2** from 110 - 170 °C (500 mTorr). This final fraction contained pure **2** (36.65 g, 0.126 moles) for a reaction yield of 75% as a colorless oil. ^{1}H NMR ($CDCl_3$, 400 MHz) δ 7.26-7.16 (m, 4H), 4.01 (m, 4H), 3.65 (t, J=7.4, 2H), 3.13 (d, J=21.6, 2H), 3.04 (t, J=7.2, 2H), 1.24 (t, J=7.2, 6H). m/z = 290.0839 (calc. = 290.0839)

diethyl-4-vinyl-benzylphosphonate (3). A solution of KOH (5.65 g, 0.100 moles), 3,5-di-tert-butylcatechol (25.6 mg, 0.115 mmol), and ethanol (115 mL) was prepared and added to a 250 mL round bottom flask containing **2** (26.60 g, 0.092 moles). A reflux condenser was affixed and the reaction solution was heated to reflux at 90 °C for 14 hrs. The reaction was then cooled to room temperature and added to ~300 mL of water and dilute HCl was added until precipitated KOH dissolved. The product was extracted from the aqueous layer with dichloromethane (3x, 100 ml), dried over $MgSO_4$, and solvent was removed *in vacuo*. 21.7 g, 0.085 moles, 93% yield. Yellow oil. ^{1}H NMR ($CDCl_3$, 400 MHz) δ 7.36-7.24 (m, 4H), 6.72-6.65 (m, 1H), 5.72 (d, J=17.6, 2H), 5.22 (d, J=11.2, 2H), 4.01 (m, 4H), 3.07 (d, J=21.2, 2H).

anilinium 4-vinyl-benzylphosphonate (4). Compound **3** (15.66 g, 61.6 mmol) was added to a 100 mL round bottom flask, under argon. TMS-Br (19.8 g, 129.3 mmol) was added drop-wise to the reaction mixture. After 90 min, the reaction mixture was exposed to vacuum to remove bromoethane. Under argon pressure, 2.5 mL of water were added and the reaction was stirred for an additional 60 min. Reacted TMS species were then removed under vacuum at 70 °C to leave a white solid. The acid could be purified by conversion to anilinium salt by dissolution in aniline:water 1:1 and recrystallization by layering with diethyl ether. m/z (dimer, ESI) = 395.0821 predicted 395.0819 ($C_{18}H_{21}O_6P_2$).

Preparation of IrO_x nanoparticles-[136,137]

Briefly, 100 ml of a 2.4 mM K_2IrCl_6 solution in MilliQ water was prepared and its pH was adjusted to 13 with KOH and heated to 90°C for 20 minutes, yielding a clear blue solution. After heating the solution was rapidly cooled, filtered, pH adjusted to 11 and stored. TEM images are shown in figure S1. As a note, the particle sizing below is unreliable as the particles were readily coalescing under the electron beam.

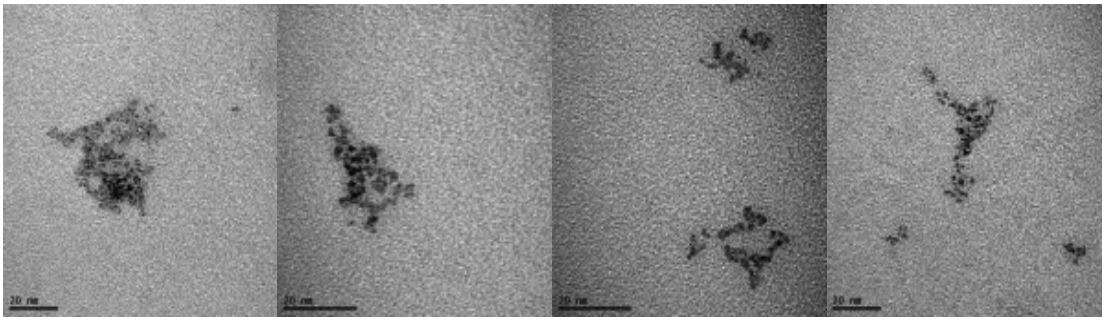

Figure S4.1. TEM images of IrOx nanoparticles prepared as described.

CdSe Quantum Dot 'Seed' Preparation, adapted from Flamee, et al.-[138]

100 mL 1-octadecene (ODE), 2.56 g CdO (20 mmol), and 16.9 g oleic acid (18.9 ml, 60 mmol) were charged to a three neck, round bottom flask fitted with a 20 cm distillation column and an oil bubbler release. The flask was degassed at 110°C until a stable line pressure was achieved. In separate Schlenk tube, 0.79 g Se and 10 mL ODE were mixed, degassed 3x and stored under Ar during the following steps. In the three neck flask, under Ar, $Cd(oleate)_2$ was formed at 250°C. A significant amount of water also condenses, so an intermediate drying step under vacuum at 100°C may be necessary to avoid flash boiling during complexation. Once a clear solution has formed, the solution was dried again under vacuum at 110°C until a stable line pressure is achieved. Under Ar, the flask temperature was raised to 260°C, and the entire Se:ODE heterogenous mixture was injected rapidly into the three neck flask. The growth proceeded for 10 minutes, after which, the external flask temperature is lowered rapidly with compressed air. At room temperature, the septum port is removed under vigorous Ar flow, and replaced with an air-free distillation head and flask. The distillation column is then removed similarly and replaced with a septum or glass plug. The flask is degassed at room temperature carefully to avoid bumping and 60 ml ODE may be distilled at 170-180°C. Following distillation, the flask is cooled under Ar, and the particles precipitated with methanol and isopropanol in a 1:1 mix. The pellet is brought up in hexanes, and precipitated with acetone. This cleaning step is repeated twice. The particles are degassed under flowing Ar for 30 minutes and pumped into an Ar filled glovebox for storage and use ([QD]= 4.47mM, $[Cd^{2+}]$=0.65M). Size control is afforded as described elsewhere.[138] For the synthesis reported, 0.2M Cd^{2+} starting concentration, we isolate 3 nm (±0.4 nm) nanoparticles. $\lambda_{max,\ abs}$=544 nm, $\lambda_{max,\ em}$=565 nm, QY =

10% relative to Rhodamine 3G (45% in EtOH).[139] Representative TEM images and an emission spectrum are shown in figure S2.

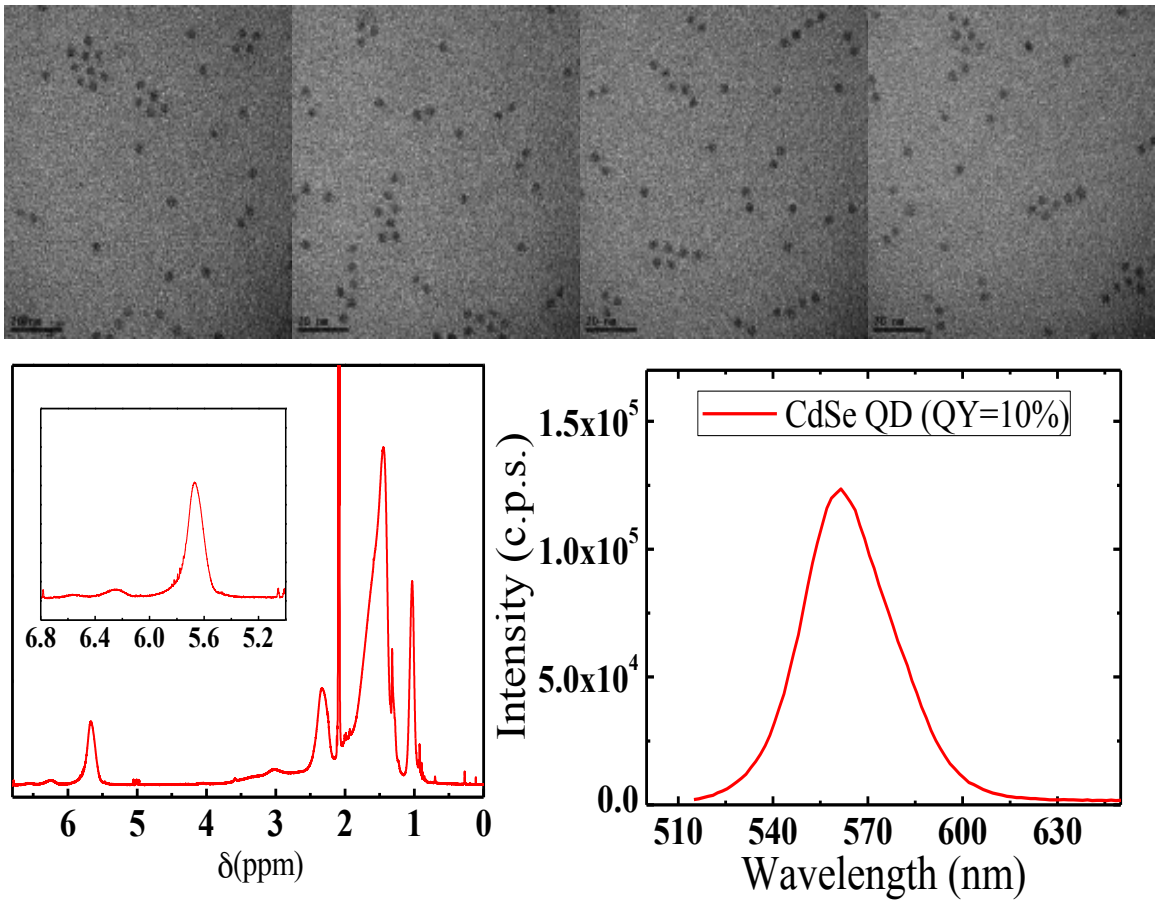

Figure S4.2. The upper panel shows several representative TEM images of CdSe QD seeds, the scale bars are 20 nm. Average size is 3.4 nm, ±0.4 nm. The lower left panel shows the ^{1}H NMR spectrum with an inset focusing on the vinylic proton of the oleate surface ligands. The two higher field resonances are unassigned, but may be reaction byproducts from the Se – octadecene reaction, tetradecyl-selenophene.[140] Lower right is a visible emission spectrum.

CdS shelling of CdSe Seeds, **adapted from Cirillo, et al.-**[127]

In general, shell thickness may be controlled with reaction time and initial seed concentration, though at longer reaction times (>1 min) Ostwald ripening becomes problematic leading to bimodal size distributions in the large core-shell particles. For thinner shells, 6 g tri-n-octylphosphine oxide, 138 mg CdO (1 mmol) and 5.81 g oleic acid (21 mmol, 6.5 ml) were charged to a three neck flask, degassed and heated at 110°C until a stable line pressure occurred. We complexed Cd(oleate)$_2$ at 250°C until a clear solution formed. The solution was cooled to 110°C and dried under vacuum there until a stable line pressure occurred. The solution was then heated to 300°C and 3 ml tri-n-octylphosphine was injected under Ar. The solution was then re-heated to 300°C, and 3 ml tri-n-butylphosphine, 112 mg S and 114 µl stock CdSe seeds (0.51 µmol seeds) were injected under argon, rapidly. After 30s, the solution temperature was lowered

quickly with compressed air and a water spray. For large shells, tri-n-octylphospine was substituted for tri-n-butyl phosphine and number of seeds lowered to 0.45 µmol. The reaction proceeded for 90 seconds instead of 30 and the injection temperature was raised to 330°C. All other conditions were the same. Once the reaction reached room temperature, 5 ml toluene was added and the nanoparticles were precipitated with 1:1 methanol:isopropanol. The particles were re-suspended in toluene and precipitated with acetone then resuspended in hexanes, dried thoroughly under vacuum and transferred into a glovebox for storage in dry d8-toluene. Representative TEM images, NMR and an emission spectra of the thinly (figure S3) and thickly (figure S4) shelled CdSeCdS core-shell QDs are shown on the following page. Scale bars for the thinly shell TEM images are 20 nm, in the thickly shelled, they are 50 nm.

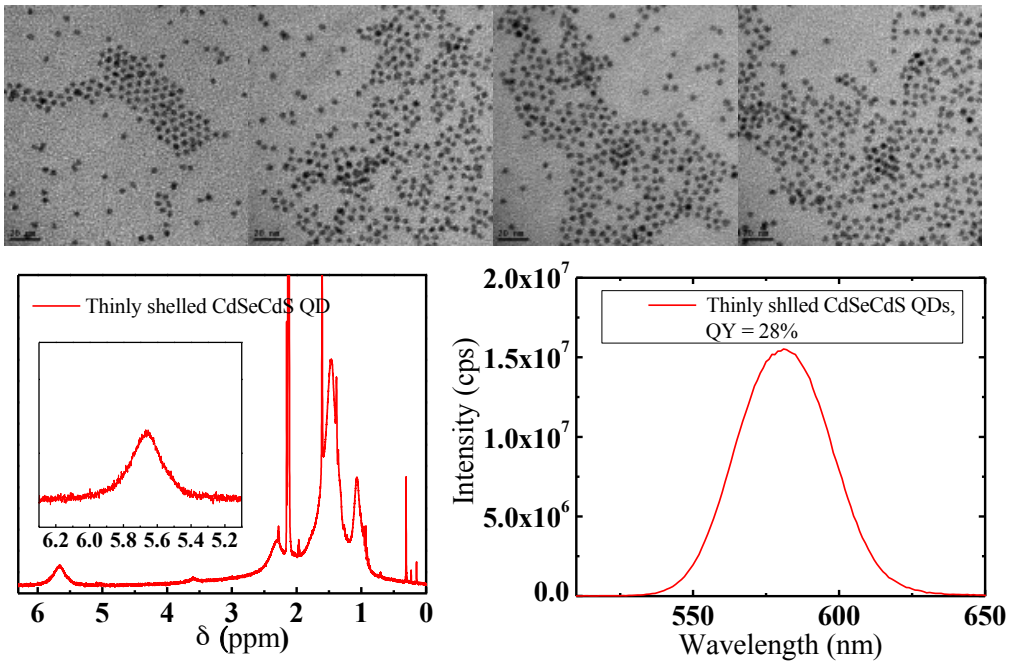

Figure 4.3. The top panel shows a set of typical TEM images of thinly shelled CdSeCdS core-shell QDs. Average diameter = 5.0 nm, ± 0.7 nm. The lower panels show a ^{1}H NMR spectrum with an inset of the vinyl region on the left. The secondary resonances from the seed synthesis are no longer apparent. An emission spectrum is shown in the lower right panel.

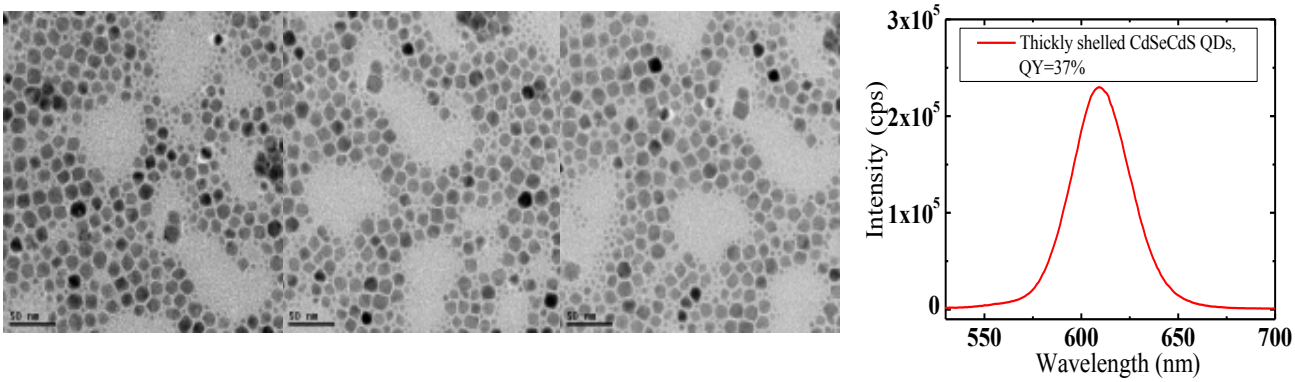

Figure 4.4. Thickly shelled CdSeCdS core-shell QDs used in the IrO_x NP – PL lifetime experiment. Note the large bi-modal size distribution in the TEM images (scale bar = 50 nm).

Ligand exchange of CdSe-CdS core-shell QDS with anilinium 4-vinyl-benzylphosponate- CdSeCdS core-shell QDs in 0.75 ml d8-toluene, typically the entire synthesis from above, were loaded into a J. Young NMR tube in a glove box. Anilinium 4-vinyl-benzylphosponate was added and the tube heated to 90ºC in a glovebox for 30 minutes. The olefinic resonance was monitored until no detectable bound signal was observed, in other words all the olefinic resonances were sharp and split. Typically 10-15 mg of the anilium phosphonate was necessary to afford complete exchange. During exchange, a white precipitate forms, possibly anilium oleate. The bound phosphonate appears as a very broad resonance in the 5-8 ppm range, with an extremely broad resonance from the benzylic protons between 2 and 4 ppm. Following exchange, the solution was filtered over Celite to remove the precipitate, concentrated to <1ml, then passed on a 30 cm gel permeation column (Bio-Rad SX-1) in toluene.[130] The particles were dried slowly under vacuum, taking care to dry as a film (large bits of nanoparticles often aggregated) and were then pumped into a glovebox. Pre- and post-exchange ^{1}H and ^{31}P NMR are shown below (black is pre, red is post, Figue S5). The extremely broad resonances from 5-8 ppm in the exchanged samples are the bound phosphonate's aromatic and vinyl protons. The benzylic protons are typically not resolvable during the exchange. The sharp resonances at 6.2 and 6.7 ppm are the liberated anilinium. In the two ^{31}P NMR spectra, the sharp resonances between 45 and 50 ppm are from residual tri-octylphosphine oxide, and trioctylphosphine. The sharp resonance at 35 ppm in the exchanged sample is from excess free 4-vinyl-benzylphosphonate while the broad resonance is the bound phosphonate. Cleaned nanoparticle spectra are shown following the exchange tracking. Note the lack of free ligand peaks. There was significant particle flocculation during the chromatography for this experiment.

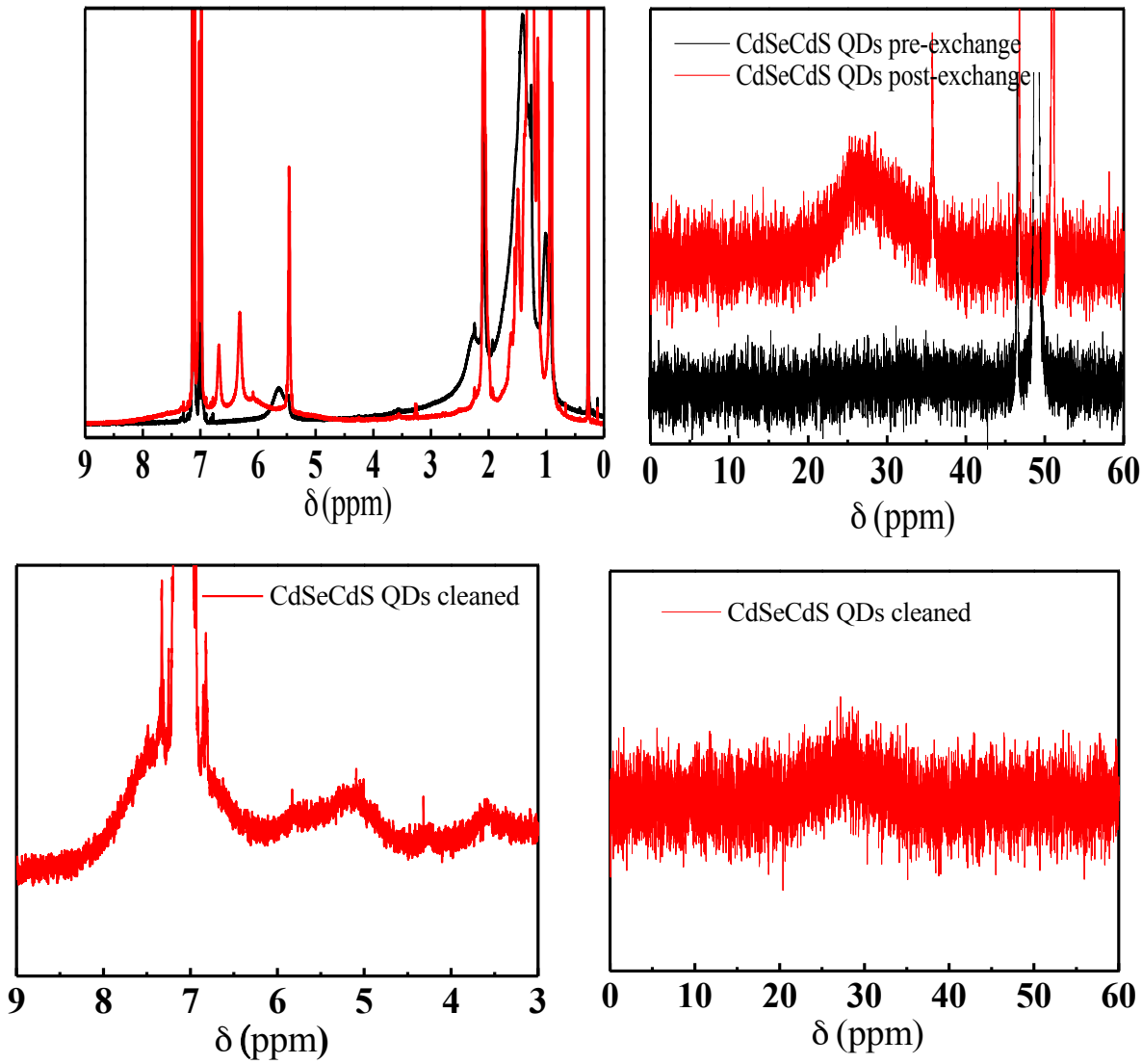

Figure S4.5. The top panels show ^{1}H and ^{31}P NMR spectra before (black) and after (red) the phosphonate ligand exchange. The lower panels show the same spectra following cleaning on a size exclusion column. Note the lack of sharp peaks from free ligand, either phosponate or oleate

Electrochemical Crosslinking-

Phosphonate exchanged CdSeCdS core-shell particles were dissolved in 0.1M tetrabutylammonium hexafluorophosphate (TBA-PF_6) in THF, [QD] ≈ 20μM. TiO_2 working, Pt mesh counter and Ag/Ag(NO_3) pseudo reference electrodes were inserted. The working electrode was cycled between -1 and –(1.8 - 2) V vs. Ag^+ 50 times at 25mV/s. A typical cyclic voltammagram is shown in figure S6, right. An equivalent CV experiment with benzyl phosphonate capped QDs (prepared equivalently to the 4-vinyl-benzyl phosphonate capped QDs) is shown as well. Note the increased cathodic current density in the phosphonate capped QD CV in red (CV of oleate capped QDs is shown in black) – we take this as an indication that vinyl

activation is proceeding. Despite attempts at acid digestion and extraction, we are unfortunately, we are not able to isolate the crosslinked ligand from the electrodes for MALDI-TOF analysis. Diffuse reflectance data is shown in figure S6, left. Cycled electrodes sensitize faster than when the electrode is simply soaked in the 4-vinyl-benzyl capped QD solution. SEM/EDX confirm penetration of the QDs throughout the TiO_2 layer (figure S7).

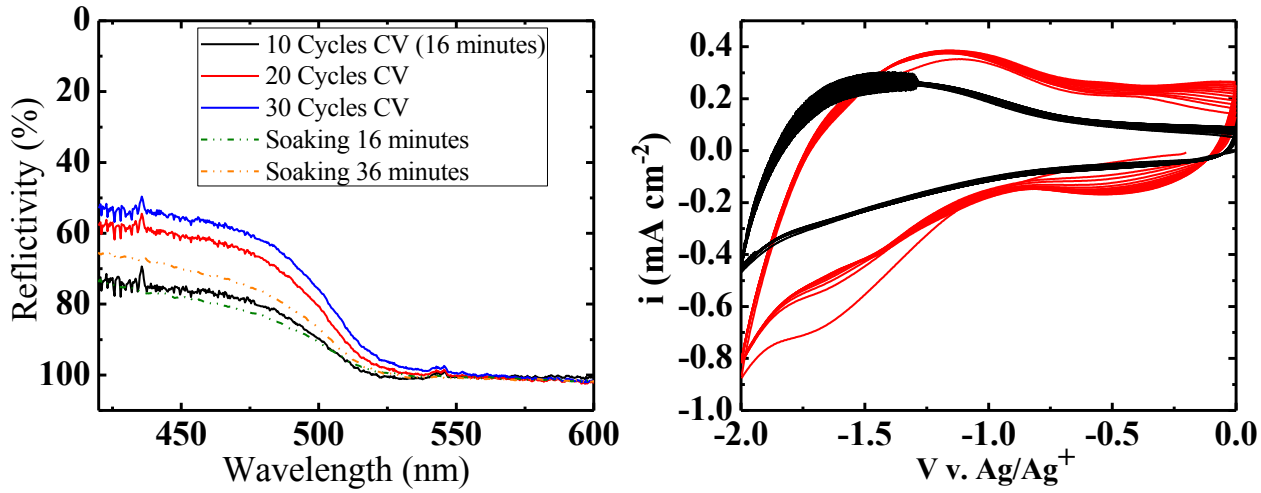

Figure S4.6. Diffuse reflectance spectra tracking TiO_2 sensitization is shown above left. CV crosslinking allows sensitization to proceed more rapidly than equivalent soaking times. Typical CVs are shown on the right. The red tracks a TiO_2 electrode cycling in a solution of phosphonate capped QDs while the black is done in a solution of oleate capped QDs. Note the larger current densities in the 4-vinyl-benzylphosphonate capped QDs, which we assign to vinyl crosslinking initiation.

IrO_x Nanoparticle Deposition-

As described, electrodes were removed from the glovebox following electropolymerization and soaked for the desired time, between 1 and 10 minutes, and washed with DI H_2O and stored in the dark before measurement. XPS showed that IrO_x was readily deposited. EDS indicates that through film IrO_x NP penetration through the film is significant

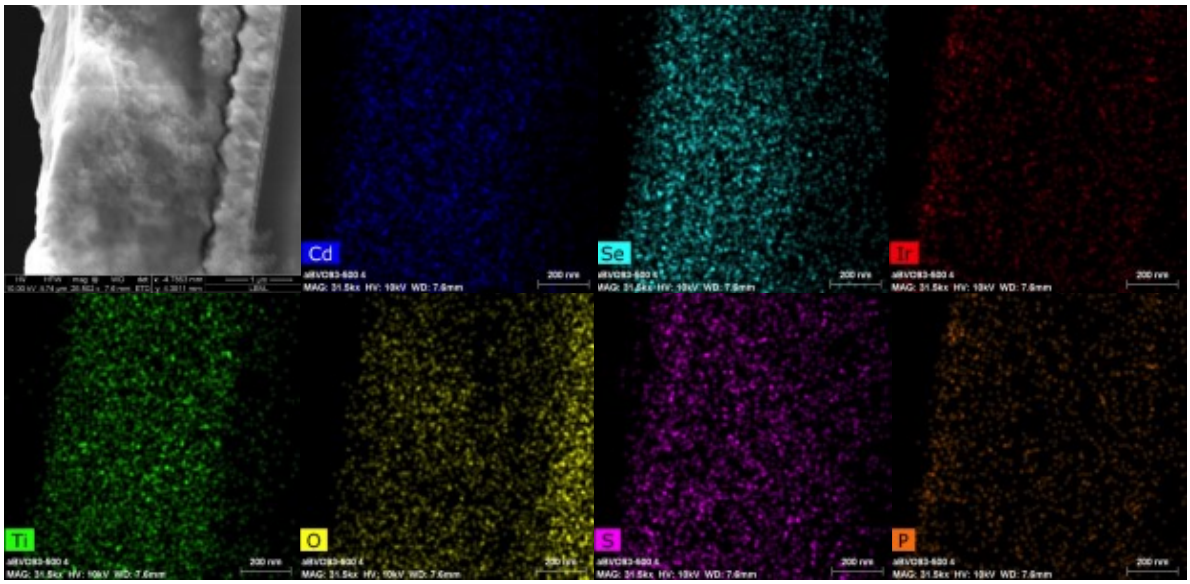

XPS for Lifetime Study-

The spectrum, shown in figure S8, was referenced to the TiO_2 $2p_{3/2}$ line at 458.5 eV. The Ir $4f_{7/2}$ at 62.4 eV corresponds relatively well with IrO_2 model compounds from the literature around 62 eV depending on preparation.[141] In the H_2O control, the feature at 61.9 eV may be assigned to TiO_2 Ti 3s which is obscured in by the Ir $4f_{7/2}$ in the PL run.[142]

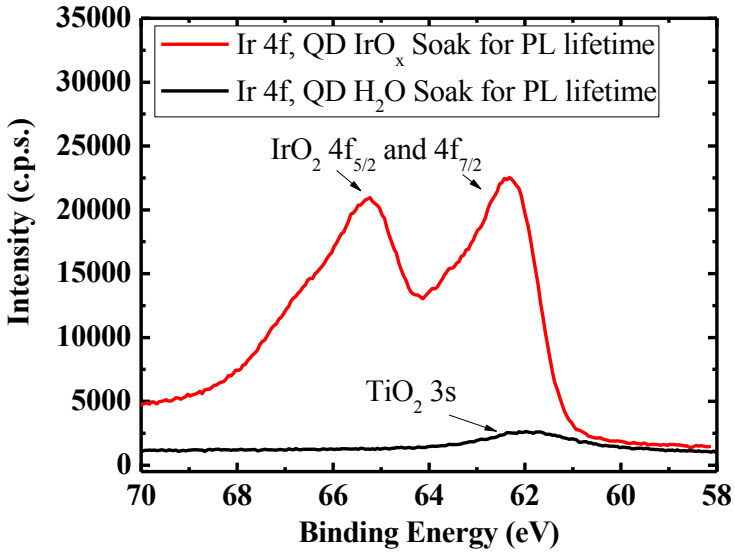

Figure S4.8. XPS of the Ir 4f region for the IrO_x PL liftetime experiment.

General Photoelectrochemical Behavior-

A stepped chronoamperometry experiment, figure S9 left, shows a V_{OC} = -450 mV vs. Ag/AgCl or 100 mV vs. RHE, with a saturating current density of 3.5μA/cm^2. An inset shows a typical

individual chronoamperometry experminent conducted in this case at -100 mV vs. Ag/AgCl. The right panel shows the long pass filter's (LPF) effectiveness at eliminating TiO_2 – IrO_x background current. This electrode was soaked in an IrO_x NP solution for 10 minutes. Upon LPF insertion, the residual current drops from 28 μA/cm^2 to 60 pA/cm^2 with a dark background, inset, of 40 pA/cm^2 indicating a residual TiO_2 photocurrent contribution of 20 pA/cm^2.

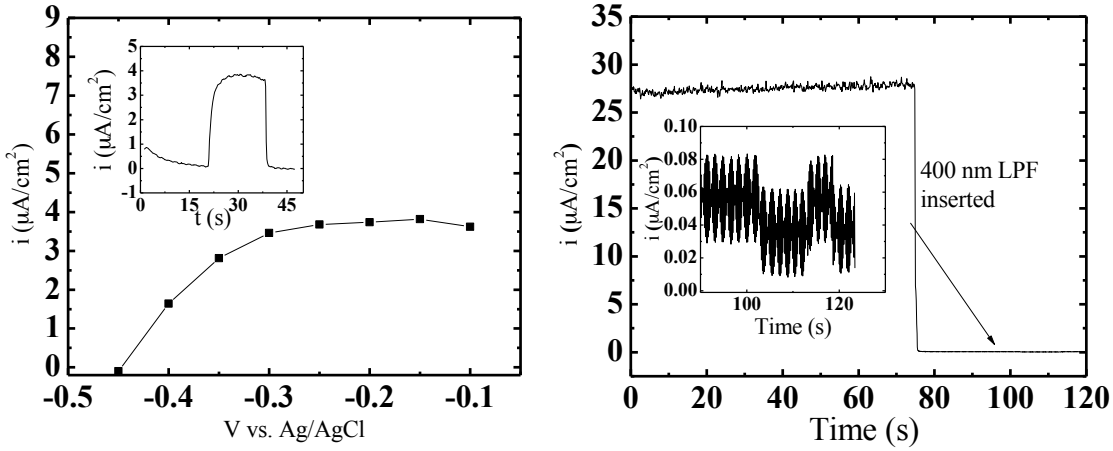

Figure S4.9. On the left is a stepped chronoamperometry experiment on a typical crosslinked QD-IrO_x-TiO_2 photoelectrode. Inset is an individual chronoamperometry experiment in which the lamp is chopped (-0.1 V vs. Ag/AgCl). Current is measured 10s into illumination. The experiments show a V_{OC} of -450 mV v. Ag/AgCl. On the right, we show the effectiveness of our long pass filter which cuts the TiO_2 photocurrent down to ~20 nA/cm^2.

O_2 Amperometry

Pt detecting electrodes were prepared from FTO coated glass electrodes by electroplating Pt films from 10 mM K_2PtCl_6 in H_2O, Pt was deposited at 1 mA/cm^2 for 15 seconds resulting in a mirror finish to the electrode. That electrode was contacted to a coated wire with silver paste then the contact and any exposed wire was sealed with Hysol-1C. Amperometry was performed as described previously.[132] Before each detection experiment, the Pt electrode was conditioned by cycling between -1.5 and 1.5 V in 1M H_2SO_4 at 25 mV/s 25 times. To test the system, a TiO_2 – IrO_x electrode and a Pt detecting electrode were sandwiched with parafilm and placed in a bulk electrolysis H-cell with a fritted glass separator between the working and reference electrodes and the counter. The cell was then sealed and purged with N_2 for ~1 hr, and the Pt electrode was cycled again between 1.5 and -1.5V v. Ag/AgCl until hydrogen adsorption and stripping waves became apparent. In the experiment below, the detecting electrode was held at -0.4 V v. Ag/AgCl while the generating TiO_2 photoanode was held at its dark V_{OC} until both electrodes equilibrated. In this test case, the dark cathodic current is high, at -14 μA, when the TiO_2 photoanode is illuminated without a 400 nm LPF, ~25μA photocurrent flows, and there is a step transient in the detecting Pt cathode (we believe this is an interfacial electric field effect). After approximately 45 seconds, detecting cathodic current begins to rise from 16.8μA as O_2 diffuses across the 2 mm gap, eventually equilibrating at 20 μA giving a detection efficiency of 12.8%.

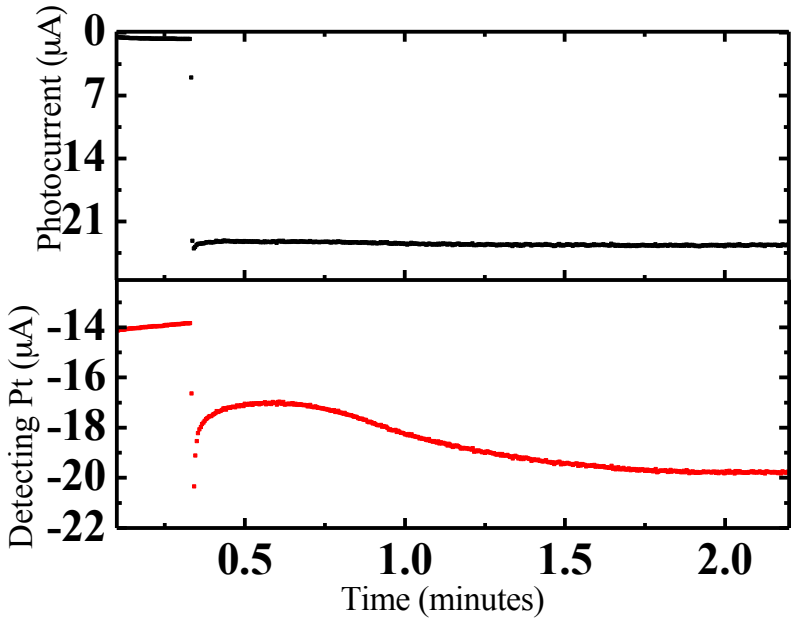

Figure S4.10. O_2 amperometry experiment on a TiO_2-IrO_x photoelectrode.

O_2 detection amperometry controls are shown below. On the left is a QD sensitized TiO_2 photoanode that has not had the IrO_x NP treatment. All photocurrent observed is corrosion current. Importantly there is no increase in detection cathodic current. There is, in fact, a decrease in background O_2 reduction current. This could be the result of Pt surface poisoning by SeO_x or Cd^{2+} species. The electrode on the right has been stripped of its ligands via a soaking in 0.1 M trimethylsilyl chloride in toluene at 40°C for 1 hr, washed with toluene and then methanol. It has then undergone an IrO_x NP soaking for 10 minutes. The photocurrent is oddly stable, for which we do not have an explanation, but we do not detect an increase in O_2 reduction current on the detecting Pt electrode which remains stable at 1.75 μA over the course of the experiment.

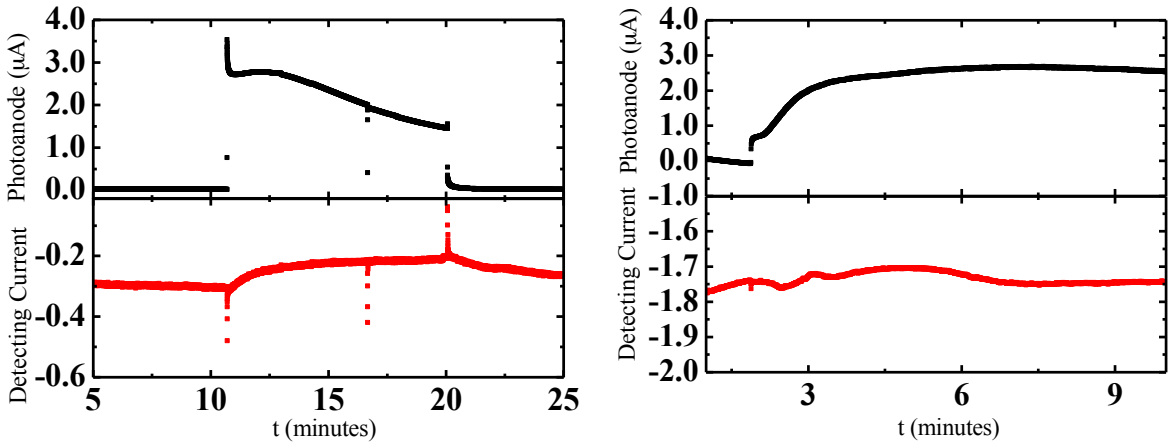

FigureS4.11. O_2 Amperometry experiments on a photoelectrode without IrO_x NPs (left) and without surface ligands (right). Neither produce O_2 detection current.

Shown below are healing experiments on a crosslinked CdSeCdS core-shell QD photoanode with phosphonate capping and IrO_x soaking. The initial O_2 detection experiment on the left once again shows the increase in cathodic detection current associated with O_2 production from the photoanode. The detection current is not particularly stable and decays after several minutes. After the experiment, the electrode is pumped into a glovebox (held under vacuum for ~3 hours to remove as much water as possible), cycled and then soaked in IrO_x NPs for 10 minutes as described previously. The panel on the right shows the second O_2 amperometry experiment. The photocurrent has returned to its initial level, as well as the O_2 production which appears more stable than the initial testing. These electrodes appear to have low detection efficiencies, ~2%.

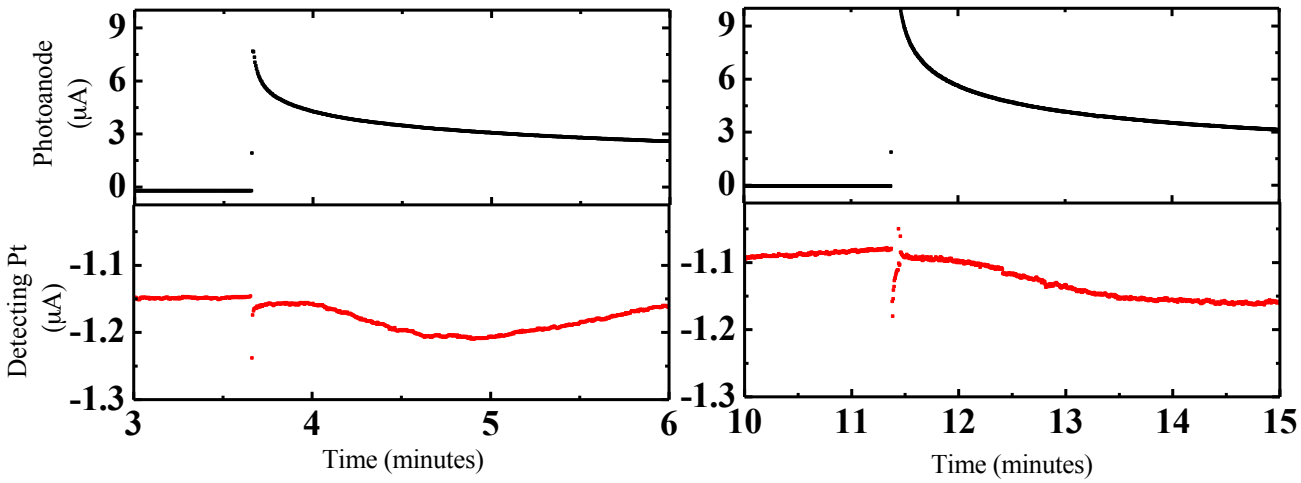

Figure S4.12. O_2 Amperometry on the same CV crosslinked QD-IrO_x-TiO_2 electrode illustrating healing and a return of O_2 production by resensitization and IrO_x NP deposition.

We examined the effect of electrochemical crosslinking on O_2 production and stability. Surprisingly, the uncrosslinked electrodes have similar O_2 production profiles to their crosslinked counterparts. Such similarity indicates that the observed surface stabilization comes from the strength of the ligand binding and not necessarily the extensiveness of the crosslinking. Unfortunately, we have not been able to determine the average M_W of the crosslinked surface ligands.

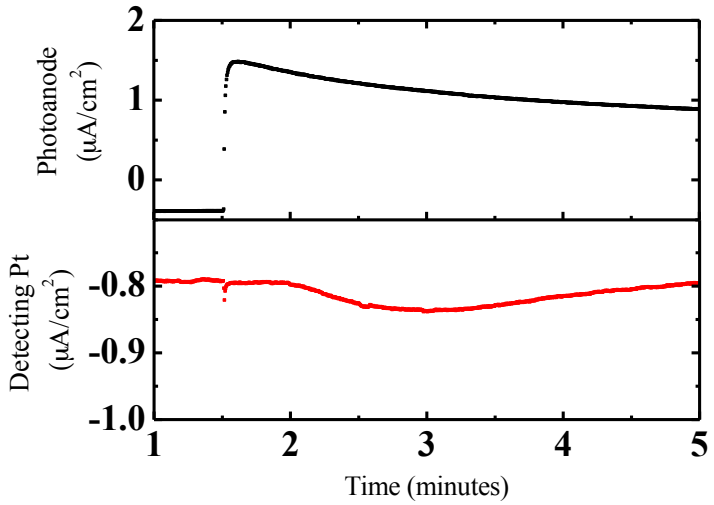

Figure S4.13. O_2 on an uncrosslinked photoelectrode. Like the crosslinked photoelectrodes, it also produces O_2.

References

(1) Alivisato, A. P. Perspectives on the Physical Chemistry of Semiconductor Nanocrystals. *J. Phys. Chem.* **1996**, *100*, 1–14.

(2) Choi, C. L.; Alivisatos, A. From Artificial Atoms to Nanocrystal Molecules: Preparation and Properties of More Complex Nanostructures. *Annu. Rev. Phys. Chem.* **2010**, *61*, 369–389.

(3) Brus, L. Electronic Wave Functions in Semiconductor Clusters : Experiment and Theory. *J. Phys. Chem.* **1986**, *90*, 2555–2560.

(4) Wannier, G. The Structure of Electronic Excitation Levels in Insulating Crystals. *Phys. Rev.* **1937**, *52*, 191–197.

(5) Grundmann, M. *The Physics of Semiconductors*; 1st ed.; Springer: Berlin, 2006.

(6) Cohen-Tannoudji, C., Diu, B. and Laloe, F. *Quantum Mechanics, Volume 1*; John Wiley and Sons: New York, 1977.

(7) Alivisatos, A. P.; Harris, A. L.; Levine, N. J.; Steigerwald, M. L.; Brus, L. E. Electronic States of Semiconductor Clusters: Homogeneous and Inhomogeneous Broadening of the Optical Spectrum. *J. Phys. Chem.* **1988**, *89*, 4001–4011.

(8) Talapin, D.; Lee, J.-S.; Kovalenko, M.; Shevchenko, E. Prospects of Colloidal Nanocrystals for Electronic and Optoelectronic Applications. *Chem. Rev.* **2010**, *110*, 389–458.

(9) Brennan, J. G.; Siegrist, T.; Carroll, P. J.; Stuczynski, S. M.; Reynders, P.; Brus, L. E.; Steigerwald, M. L. Bulk and Nanostructure Group 11-VI Compounds from Molecular Organometallic Precursors. *Chem. Mater.* **1990**, *2*, 403–409.

(10) La Mer, V. K.; Dinegar, R. H. Theory, Production and Mechanism of Formation of Monodispersed Hydrosols. *J. Am. Chem. Soc.* **1950**, *72*, 4847–4854.

(11) Murray, C. B.; Noms, D. J.; Bawendi, M. G. Synthesis and Characterization of Nearly Monodisperse CdE (E = S, Se, Te) Semiconductor Nanocrystallites. *J. Am. Chem. Soc.* **1993**, *115*, 8706–8715.

(12) Peng, X.; Schlamp, M. C.; Kadavanich, A. V; Alivisatos, A. P. Epitaxial Growth of Highly Luminescent CdSe / CdS Core / Shell Nanocrystals with Photostability and Electronic Accessibility. *J. Am. Chem. Soc.* **1997**, *119*, 7019–7029.

(13) Hines, M. A.; Guyot-sionnest, P. Synthesis and Characterization of Strongly Luminescing ZnS-Capped CdSe Nanocrystals. *J. Phys. Chem.* **1996**, *100*, 468–471.

(14) Dabbousi, B. O.; Mikulec, F. V; Heine, J. R.; Mattoussi, H.; Ober, R.; Jensen, K. F.; Bawendi, M. G. (CdSe) ZnS Core - Shell Quantum Dots : Synthesis and Characterization of a Size Series of Highly Luminescent Nanocrystallites. *J. Phys. Chem. B* **1997**, *101*, 9463–9475.

(15) Chen, O.; Zhao, J.; Chauhan, V. P.; Cui, J.; Wong, C.; Harris, D. K.; Wei, H.; Han, H.-S.; Fukumura, D.; Jain, R. K.; et al. Compact High-Quality CdSe-CdS Core-Shell Nanocrystals with Narrow Emission Linewidths and Suppressed Blinking. *Nat. Mater.* **2013**, *12*, 445–451.

(16) Manna, L.; Milliron, D.; Meisel, A.; Scher, E. C.; Alivisatos, A. Controlled Growth of Tetrapod-Branched Inorganic Nanocrystals. *Nat. Mater.* **2003**, *2*, 382–385.

(17) Carbone, L.; Nobile, C.; Giorgi, M.; Sala, F.; Morello, G.; Pompa, P.; Hytch, M.; Snoeck, E.; Fiore, A.; Franchini, I.; et al. Synthesis and Micrometer-Scale Assembly of Colloidal CdSe/CdS Nanorods Prepared by a Seeded Growth Approach. *Nano Lett.* **2007**, *7*, 2942–2950.

(18) Talapin, D. V; Nelson, J.; Shevchenko, E. V; Aloni, S.; Sadtler, B.; Alivisatos, A. Seeded Growth of Highly Luminescent CdSe/CdS Nanoheterostructures with Rod and Tetrapod Morphologies. *Nano Lett.* **2007**, *7*, 2951–2959.

(19) Sitt, A.; Sala, F.; Menagen, G.; Banin, U. Multiexciton Engineering in Seeded Core/Shell Nanorods: Transfer from Type-I to Quasi-Type-II Regimes. *Nano Lett.* **2009**, *9*, 3470–3476.

(20) Smith, E. R.; Luther, J. M.; Johnson, J. C. Ultrafast Electronic Delocalization in CdSe/CdS Quantum Rod Heterostructures. *Nano Lett.* **2011**, *11*, 4923–4931.

(21) Amirav, L.; Alivisatos, A. P. Photocatalytic Hydrogen Production with Tunable Nanorod Heterostructures. *J. Phys. Chem. Lett.* **2010**, *1*, 1051–1054.

(22) Habas, S.; Yang, P.; Mokari, T. Selective Growth of Metal and Binary Metal Tips on CdS Nanorods. *J. Am. Chem. Soc.* **2008**, *130*, 3294–3295.

(23) Marcus, R. A. Chemical and Electrochemical Electron-Transfer Theory. *Annu. Rev. Phys. Chem.* **1964**, *15*, 155–196.

(24) Miller, J. R., Calcaterra, L. T. and Closs, G. L. Intramolecular Long-Distance Electron Transfer in Radical Anions. The Effects of Free Energy and Solvent on the Reaction Rates'. *J. Am. Chem. Soc.* **1984**, *106*, 3047–3049.

(25) Bard, A. J. and L. F. *Electrochemical Methods: Fundamentals and Applications*; John Wiley and Sons: New York, 2001.

(26) Bockris, John O M, Reddy, A . and Gamboa-Aldeco, M. *Modern Electrochemistry 2A: Fundamentals of Electrodics*; Plenum Publishers: New York, 2000.

(27) Eckermann, A. L.; Feld, D. J.; Shaw, J. A.; Meade, T. J. Electrochemistry of Redox-Active Self-Assembled Monolayers. *Coord. Chem. Rev.* **2010**, *254*, 1769–1802.

(28) Anderson, N. A.; Lian, T. Ultrafast Electron Transfer at the Molecule-Semiconductor Nanoparticle Interface. *Annu. Rev. Phys. Chem.* **2005**, *56*, 491–519.

(29) Wilker, M. B.; Schnitzenbaumer, K. J.; Dukovic, G. Recent Progress in Photocatalysis Mediated by Colloidal II-VI Nanocrystals. *Isr. J. Chem.* **2012**, *52*, 1002–1015.

(30) Han, Z.; Qiu, F.; Eisenberg, R.; Holland, P. L.; Krauss, T. D. Robust Photogeneration of H2 in Water Using Semiconductor Nanocrystals and a Nickel Catalyst. *Science* **2012**, *338*, 1321–1324.

(31) Brown, K.; Dayal, S.; Ai, X.; Rumbles, G.; King, P. Controlled Assembly of Hydrogenase-CdTe Nanocrystal Hybrids for Solar Hydrogen Production. *J. Am. Chem. Soc.* **2010**, *132*, 9672–9680.

(32) Pernik, D. R.; Tvrdy, K.; Radich, J. G.; Kamat, P. V. Tracking the Adsorption and Electron Injection Rates of CdSe Quantum Dots on TiO 2 : Linked versus Direct Attachment. **2011**, 13511–13519.

(33) Das, A.; Han, Z.; Haghighi, M. G.; Eisenberg, R. Photogeneration of Hydrogen from Water Using CdSe Nanocrystals Demonstrating the Importance of Surface Exchange. *Proc. Natl. Acad. Sci. U. S. A.* **2013**, *110*, 16716–16723.

(34) Tan, M. X.; Laibinis, P. E.; Nguyen, S. T.; Kesselman, J. M.; Stanton, C. E.; Lewis, N. S. Principles and Applications of Semiconductor Photoelectrochemistry. In *Progress in Inorganic Chemistry*; John Wiley and Sons: New York, 1994; Vol. 41, pp. 21–144.

(35) O'Regan, B.; Grätzel, M. A Low-Cost, High-Efficiency Solar Cell Based on Dye-Sensitized Colloidal TiO2 Films. *Nature* **1991**, *353*, 737–740.

(36) Hagfeldt, A.; Boschloo, G.; Sun, L.; Kloo, L.; Pettersson, H. Dye-Sensitized Solar Cells. *Chem. Rev.* **2010**, *110*, 6595–6663.

(37) Kamat, P.; Tvrdy, K.; Baker, D.; Radich, J. Beyond Photovoltaics: Semiconductor Nanoarchitectures for Liquid-Junction Solar Cells. *Chem. Rev.* **2010**, *110*, 6664–6688.

(38) Robel, I.; Kuno, M.; Kamat, P. V. Size-Dependent Electron Injection from Excited CdSe Quantum Dots into TiO2 Nanoparticles. *J. Am. Chem. Soc.* **2007**, *129*, 4136–4137.

(39) Radich, J. G.; Peeples, N. R.; Santra, P. K.; Kamat, P. V. Charge Transfer Mediation Through CuxS. The Hole Story of CdSe in Polysulfide. **2014**.

(40) James, B. D.; Perez, G. N. B. J.; Baum, K. N. *Technoeconomic Analysis of Photoelectrochemical (PEC) Hydrogen Production*; Arlington, VA, 2009; Vol. 22201.

(41) Esswein, A. J.; Nocera, D. G. Hydrogen Production by Molecular Photocatalysis. *Chem. Rev.* **2007**, *107*, 4022–4047.

(42) Lewis, N.; Nocera, D. Powering the Planet: Chemical Challenges in Solar Energy Utilization. *Proc. Natl. Acad. Sci.* **2006**, *104*, 15729–15735.

(43) Walter, M.; Warren, E.; McKone, J.; Boettcher, S.; Mi, Q.; Santori, E.; Lewis, N. Solar Water Splitting Cells. *Chem. Rev.* **2010**, *110*, 6446–6473.

(44) Barber, J. Photosystem II: The Engine of Life. *Q. Rev. Biophys.* **2003**, *36*, 71–89.

(45) Brettel, K. Electron Transfer and Arrangement of the Redox Cofactors in Photosystem I. *Biochim. Biophys. Acta* **1997**, *1318*, 322–373.

(46) Grimes, C. *Light, Water, Hydrogen*; Springer, 2008.

(47) Chen, X.; Shen, S.; Guo, L.; Mao, S. Semiconductor-Based Photocatalytic Hydrogen Generation. *Chem. Rev.* **2010**, *110*, 6503–6570.

(48) Hori, Y. *Modern Aspects of Electrochemistry No. 42*; Vayenas, C. G.; White, R. E.; Gamboa-Aldeco, M. E., Eds.; Springer, 2008; pp. 82–102.

(49) Hu, S.; Xiang, C.; Haussener, S.; Berger, A. D.; Lewis, N. S. An Analysis of the Optimal Band Gaps of Light Absorbers in Integrated Tandem Photoelectrochemical Water-Splitting Systems. *Energy Environ. Sci.* **2013**.

(50) Gerischer, H. On the Stability of Semiconductor Electrodes against Photodecomposition. *J. Electroanal. Chem.* **1977**, *82*, 133–143.

(51) Chen, S.; Wang, L.-W. Thermodynamic Oxidation and Reduction Potentials of Photocatalytic Semiconductors in Aqueous Solution. *Chem. Mater.* **2012**, *24*, 3659–3666.

(52) Pourbaix, M. *Atlas of Electrochemical Equilibria in Aqueous Solutions*; National Association of Corrosion Engineers: Houston, TX, 1974.

(53) Park, S.; Barber, M. E. Thermodynamic Stabilities of Semiconductor Electrodes. *J. Electroanal. Chem.* **1979**, *99*, 67–75.

(54) Fujishima, A. and Honda, K. Electrochemical Photolysis of Water at a Semiconductor Electrode. *Nature* **1972**, *238*, 37–38.

(55) Hodes, G.; Cahen, D.; Manassen, J. Tungsten Trioxide as a Photoanode for a Photoelectrochemical Cell (PEC). *Nature* **1976**, *260*, 312–313.

(56) Chen, X.; Liu, L.; Yu, P. Y.; Mao, S. S. Increasing Solar Absorption for Photocatalysis with Black Hydrogenated Titanium Dioxide Nanocrystals. *Science (80-.).* **2012**, *331*, 746–750.

(57) Abdi, F. F.; Han, L.; Smets, A. H. M.; Zeman, M.; Dam, B.; van de Krol, R. Efficient Solar Water Splitting by Enhanced Charge Separation in a Bismuth Vanadate-Silicon Tandem Photoelectrode. *Nat. Commun.* **2013**, *4*, 2195.

(58) Campet, G., Puprichitkun, C. and Sun, Z. W. Protection of Photoanodes against Photocorrosion by Surface Deposition of Oxide Films: Criteria for Choosing the Protective Coating. *J. Electroanal. Chem.* **1989**, *269*, 435–445.

(59) Kainthla, R. C.; Zelenay, B.; Bockris, J. O. M. Significant Efficiency Increase in Self-Driven Photoelectrochemical Cell for Water Photoelectrolysis. **1985**, *134*, 4–8.

(60) Kainthla, R. C.; Zelenay, B.; Bockris, J. Protection of n-Si Photoanode against Photocorrosion in Photoelectrochemical Cell for Water Electrolysis. *J. Electrochem. Soc.* **1986**, *133*, 248.

(61) Hu, S.; Shaner, M. R.; Beardslee, J. a.; Lichterman, M.; Brunschwig, B. S.; Lewis, N. S. Amorphous TiO_2 Coatings Stabilize Si, GaAs, and GaP Photoanodes for Efficient Water Oxidation. *Science* **2014**, *344*, 1005–1009.

(62) Goodenough, J. Metallic Oxides. *Prog. Solid State Chem.* **1971**, *5*, 145–399.

(63) Noufi, R.; Tench, D.; Warren, L. Protection of Semiconductor Photoanodes with Photoelectrochemically Generated Polypyrrole Films. *J. Electrochem. Soc.* **1981**, *128*, 1–4.

(64) Chen, Y. W.; Prange, J. D.; Dühnen, S.; Park, Y.; Gunji, M.; Chidsey, C. E. D.; McIntyre, P. C. Atomic Layer-Deposited Tunnel Oxide Stabilizes Silicon Photoanodes for Water Oxidation. *Nat. Mater.* **2011**, *10*, 539–544.

(65) Kenney, M. J.; Gong, M.; Li, Y.; Wu, J. Z.; Feng, J.; Lanza, M.; Dai, H. High-Performance Silicon Photoanodes Passivated with Ultrathin Nickel Films for Water Oxidation. *Science* **2013**, *342*, 836–840.

(66) Tang, M.; Grauer, D.; Lassalle-Kaiser, B.; Yachandra, V.; Amirav, L.; Long, J. R.; Yano, J.; Alivisatos, A. Structural and Electronic Study of an Amorphous MoS3 Hydrogen-Generation Catalyst on a Quantum-Controlled Photosensitizer. *Angew. Chemie Int. Ed.* **2011**, *50*, 10203–10207.

(67) Dresselhaus, M. S.; Thomas, I. L. Alternative Energy Technologies. *Nature* **2001**, *414*, 332–337.

(68) Khaselev, O. A Monolithic Photovoltaic-Photoelectrochemical Device for Hydrogen Production via Water Splitting. *Science* **1998**, *280*, 425–427.

(69) Wang, Q.; Hisatomi, T.; Ma, S. S. K.; Li, Y.; Domen, K. Core/Shell Structured La-and Rh-Codoped SrTiO3 as a Hydrogen Evolution Photocatalyst in Z-Scheme Overall Water Splitting under Visible Light Irradiation. *Chem. Mater.* **2014**, *26*, 4144–4150.

(70) Wang, X.; Maeda, K.; Thomas, A.; Takanabe, K.; Xin, G.; Carlsson, J.; Domen, K.; Antonietti, M. A Metal-Free Polymeric Photocatalyst for Hydrogen Production from Water under Visible Light. *Nat. Mater.* **2008**, *8*, 76–80.

(71) Le Goff, A.; Artero, V.; Jousselme, B.; Tran, P. D.; Guillet, N.; Métayé, R.; Fihri, A.; Palacin, S.; Fontecave, M. From Hydrogenases to Noble Metal-Free Catalytic Nanomaterials for H2 Production and Uptake. *Science* **2009**, *326*, 1384–1387.

(72) Prins, R.; De Beer, V. H. J.; Somorjai, G. a. Structure and Function of the Catalyst and the Promoter in Co—Mo Hydrodesulfurization Catalysts. *Catal. Rev.* **1989**, *31*, 1–41.

(73) Nanoclusters, M.; Tuxen, A.; Kibsgaard, J.; Gøbel, H.; Lægsgaard, E.; Topsøe, H.; Lauritsen, J. V; Besenbacher, F. Size Threshold in the Dibenzothiophene. *ACS Nano* **2010**, *4*, 4677–4682.

(74) Taniguchi, M.; Imamura, D.; Ishige, H.; Youichi, I.; Murata, T.; Hidai, M.; Tatsumi, T. Hydrodesulfurization of Benzothiophene over Zeolite-Supported Catalysts Prepared from Mo and Mo–Ni Sulfide Clusters. *J. Catal.* **1999**, *187*, 139–150.

(75) Topsoe, H.; Clausen, B.; Massoth, F. E. *Hydrotreating Catalysis - Science and Technology*; Springer-Verlag: Berlin, 1996.

(76) Jaramillo, T. F.; Nanocatalysts, M.; Jørgensen, K. P.; Bonde, J.; Nielsen, J. H.; Horch, S.; Chorkendorff, I. Identification of Active Edge Sites for Electrochemical H 2 Evolution from MoS2 Nanocatalysts. *Science* **2007**, *317*, 100–102.

(77) Jaramillo, T.; Bonde, J.; Zhang, J.; Ooi, B.; Andersson, K.; Ulstrup, J.; Chorkendorff, I. Hydrogen Evolution on Supported Incomplete Cubane-Type [Mo3S4] 4+ Electrocatalysts. *J. Phys. Chem. C* **2008**, *112*, 17492–17498.

(78) Appel, A.; DuBois, D.; DuBois, M. Molybdenum−Sulfur Dimers as Electrocatalysts for the Production of Hydrogen at Low Overpotentials. *J. Am. Chem. Soc.* **2005**, *127*, 12717–12726.

(79) Karunadasa, H. I.; Chang, C. J.; Long, J. R. A Molecular Molybdenum-Oxo Catalyst for Generating Hydrogen from Water. *Nature* **2010**, *464*, 1329–1333.

(80) Merki, D.; Fierro, S.; Vrubel, H.; Hu, X. Amorphous Molybdenum Sulfide Films as Catalysts for Electrochemical Hydrogen Production in Water. *Chem. Sci.* **2011**, *2*, 1262.

(81) Hinnemann, B.; Moses, P.; Bonde, J.; Jørgensen, K.; Nielsen, J.; Horch, S.; Chorkendorff, I.; Nørskov, J. Biomimetic Hydrogen Evolution: MoS2 Nanoparticles as Catalyst for Hydrogen Evolution. *J. Am. Chem. Soc.* **2005**, *127*, 5308–5309.

(82) Kanan, M. W.; Nocera, D. G. In Situ Formation of an Oxygen-Evolving Catalyst in Neutral Water Containing Phosphate and Co2+. *Science* **2008**, *321*, 1072–1075.

(83) Kanan, M. W.; Yano, J.; Surendranath, Y.; Dincă, M.; Yachandra, V. K.; Nocera, D. G. Structure and Valency of a Cobalt-Phosphate Water Oxidation Catalyst Determined by in Situ X-Ray Spectroscopy. *J. Am. Chem. Soc.* **2010**, *132*, 13692–13701.

(84) Talapin, D. V; Koeppe, R.; Go, S.; Kornowski, A.; Lupton, J. M.; Rogach, A. L.; Benson, O.; Feldmann, J.; Weller, H. Highly Emissive Colloidal CdSe / CdS Heterostructures of Mixed Dimensionality. *Nano Lett.* **2003**, *3*, 1677–1681.

(85) Frame, F.; Osterloh, F. CdSe-MoS2: A Quantum Size-Confined Photocatalyst for Hydrogen Evolution from Water under Visible Light. *J. Phys. Chem. C* **2010**, *114*, 10628–10633.

(86) Zong, X.; Yan, H.; Wu, G.; Ma, G.; Wen, F.; Wang, L.; Li, C. Enhancement of Photocatalytic H Evolution on CdS by Loading MoS as Cocatalyst under Visible Light Irradiation. *J. Am. Chem. Soc.* **2008**, *130*, 7176–7177.

(87) Hédoire, C.-E.; Cadot, E.; Villain, F.; Davidson, A.; Louis, C.; Breysse, M. Preparation and Characterization of Molybdenum Sulfide Supported on B-Zeolites Obtained from [Mo3S4(H2O)9]4+ Precursor. *Appl. Catal. A Gen.* **2006**, *306*, 165–174.

(88) Mos, S.; Hibble, S. J.; Rice, D. A.; Pickup, D. M.; Beer, M. P.; Rg, R. Mo K-Edge EXAFS and S K-Edge Absorption Studies of the Amorphous Molybdenum Sulfides MoS4.7, MoS3, and MoS3-nH2O (n ~ 2). *Inorg. Chem.* **1995**, *34*, 5109–5113.

(89) Cramer, S. P.; Liang, K. S.; Jacobson, A. J.; Chang, C. H.; Chianelli, R. R. EXAFS Studies of Amorphous Molybdenum and Tungsten Trisulfides and Triselenides. *Inorg. Chem.* **1984**, *23*, 1215–1221.

(90) Newville, M. IFEFFIT : Interactive XAFS Analysis and FEFF Fitting. *J. Synchrotron Radiat.* **2001**, *8*, 322–324.

(91) Newville, M.; Ravel, B.; Haskel, D.; Rehr, J. J.; Stern, E. A.; Yacoby, Y. Analysis of Multiple-Scattering XAFS Data Using Theoretical Standards. *Phys. B Condens. Matter* **1995**, *208*, 154–156.

(92) Rehr, J. J.; Alber, R. C. Theoretical Approaches to X-Ray Absorption Fine Structure. *Rev. Mod. Phys.* **2000**, *72*, 621–654.

(93) Hibble, S.; Wood, G. Modeling the Structure of Amorphous MoS3: A Neutron Diffraction and Reverse Monte Carlo Study. *J. Am. Chem. Soc.* **2004**, *126*, 959–965.

(94) K. S. Liang, J. P. deNeufville, A. J. Jacobson, R. R. C. Structure of Amorphous Transition Metal Sulfides. *J. Non. Cryst. Solids* **1980**, *36*, 1249–1254.

(95) Walton, R.; Dent, A.; Hibble, S. In Situ Investigation of the Thermal Decomposition of Ammonium Tetrathiomolybdate Using Combined Time-Resolved X-Ray Absorption Spectroscopy and X-Ray Diffraction. *Chem. Mater.* **1998**, *10*, 3737–3745.

(96) Grauer, D. C.; Alivisatos, A. P. Ligand Dissociation Mediated Charge Transfer Observed at Colloidal W18O49 Nanoparticle Interfaces. *Langmuir* **2014**, *30*, 2325–2328.

(97) Kamat, P. Meeting the Clean Energy Demand: Nanostructure Architectures for Solar Energy Conversion. *J. Phys. Chem. C* **2007**, *111*, 2834–2860.

(98) Yin, Y.; Alivisatos, A. Colloidal Nanocrystal Synthesis and the Organic–inorganic Interface. *Nature* **2005**, *437*, 664–670.

(99) Greenham, N.; Peng, X.; Alivisatos, A. Charge Separation and Transport in Conjugated-Polymer/semiconductor-Nanocrystal Composites Studied by Photoluminescence Quenching and Photoconductivity. *Phys. Rev. B. Condens. Matter* **1996**, *54*, 17628–17637.

(100) Zhu, H.; Song, N.; Lian, T. Controlling Charge Separation and Recombination Rates in CdSe/ZnS Type I Core−Shell Quantum Dots by Shell Thicknesses. *J. Am. Chem. Soc.* **2010**, *132*, 15038–15045.

(101) Murray, R. W. Nanoelectrochemistry: Metal Nanoparticles, Nanoelectrodes, and Nanopores. *Chem. Rev.* **2008**, *108*, 2688–2720.

(102) Anderson, N. a; Lian, T. Ultrafast Electron Transfer at the Molecule-Semiconductor Nanoparticle Interface. *Annu. Rev. Phys. Chem.* **2005**, *56*, 491–519.

(103) Bakkers, E.; Roest, A.; Marsman, A.; Jenneskens, L.; Steensel, L.; Kelly, J.; Vanmaekelbergh, D. Characterization of Photoinduced Electron Tunneling in Gold/SAM/Q-CdSe Systems by Time-Resolved Photoelectrochemistry. *J. Phys. Chem. B* **2000**, *104*, 7266–7272.

(104) Liu, Y.; Gibbs, M.; Puthussery, J.; Gaik, S.; Ihly, R.; Hillhouse, H.; Law, M. Dependence of Carrier Mobility on Nanocrystal Size and Ligand Length in PbSe Nanocrystal Solids. *Nano Lett.* **2010**, *10*, 1960–1969.

(105) Moreels, I.; Martins, J. C.; Hens, Z. Ligand Adsorption/desorption on Sterically Stabilized InP Colloidal Nanocrystals: Observation and Thermodynamic Analysis. *Chemphyschem* **2006**, *7*, 1028–1031.

(106) Fritzinger, B.; Capek, R.; Lambert, K.; Martins, J. C.; Hens, Z. Utilizing Self-Exchange to Address the Binding of Carboxylic Acid Ligands to CdSe Quantum Dots. *J. Am. Chem. Soc.* **2010**, *132*, 10195–10201.

(107) Hens, Z. and J. C. M. A Solution NMR Toolbox for Characterizing the Surface Chemistry of Colloidal Nanocrystals. *Chem. Mater.* **2013**, *25*, 1211–1221.

(108) Hostetler, M.; Templeton, A.; Murray, R. Dynamics of Place-Exchange Reactions on Monolayer-Protected Gold Cluster Molecules. *Langmuir* **1999**, *15*, 3782–3789.

(109) Green, S.; Stokes, J.; Hostetler, M.; Pietron, J.; Murray, R. Three-Dimensional Monolayers: Nanometer-Sized Electrodes of Alkanethiolate-Stabilized Gold Cluster Molecules. *J. Phys. Chem. B* **1997**, *101*, 2663–2668.

(110) Mi, Q.; Ping, Y.; Li, Y.; Cao, B.; Brunschwig, B.; Khalifah, P.; Galli, G.; Gray, H. B.; Lewis, N. S. Thermally Stable N -Intercalated WO Photoanodes for Water Oxidation. *J. Am. Chem. Soc.* **2012**, *134*, 18318–18324.

(111) Manthiram, K.; Alivisatos, A. Tunable Localized Surface Plasmon Resonances in Tungsten Oxide Nanocrystals. *J. Am. Chem. Soc.* **2012**, *134*, 3995–3998.

(112) Dulz, G. and Sutin, N. The Kinetics of the Oxidation of Iron(II) and Its Substituted Tris-(1,10-Phenanthroline) Complexes by Cerium (IV). *Inorg. Chem.* **1963**, *2*, 917–921.

(113) Guo, W.; Li, J. J.; Wang, Y. A.; Peng, X. Luminescent CdSe/CdS Core/shell Nanocrystals in Dendron Boxes: Superior Chemical, Photochemical and Thermal Stability. *J. Am. Chem. Soc.* **2003**, *125*, 3901–3909.

(114) Kwon, S. G.; Krylova, G.; Sumer, A.; Schwartz, M. M.; Bunel, E. E.; Marshall, C. L.; Chattopadhyay, S.; Lee, B.; Jellinek, J.; Shevchenko, E. V. Capping Ligands as Selectivity Switchers in Hydrogenation Reactions. *Nano Lett.* **2012**, *12*, 5382–5388.

(115) Lee, K.; Seo, W.; Park, J. Synthesis and Optical Properties of Colloidal Tungsten Oxide Nanorods. *J. Am. Chem. Soc.* **2003**, *125*, 3408–3409.

(116) Nenadovie, M. T.; Rajh, T. Electron Transfer Reactions and Flat-Band Potentials of WO:, Colloids. **1984**, *424*, 5827–5830.

(117) Salje, E.; Güttler, B. Anderson Transition and Intermediate Polaron Formation in WO3-X Transport Properties and Optical Absorption. *Philos. Mag. Part B* **1984**, *50*, 607–620.

(118) Hammes, G. G. *Principles of Chemical Kinetics*; Academic Publishers: New York, 1978; pp. 1–19.

(119) Coppel, Y.; Spataro, G.; Pagès, C.; Chaudret, B.; Maisonnat, A.; Kahn, M. L. Full Characterization of Colloidal Solutions of Long-Alkyl-Chain-Amine-Stabilized ZnO Nanoparticles by NMR Spectroscopy: Surface State, Equilibria, and Affinity. *Chem. Eur. J.* **2012**, *18*, 5384–5393.

(120) Noufi, R.; Tench, D.; Warren, L. F. Protection of N-GaAs Photoanodes with Photoelectrochemically Generated Polypyrrole Films.

(121) Youngblood, W. J.; Lee, S.-H. A.; Maeda, K.; Mallouk, T. E. Visible Light Water Splitting Using Dye-Sensitized Oxide Semiconductors. *Acc. Chem. Res.* **2009**, *42*, 1966–1973.

(122) Youngblood, W.; Lee, S.-H.; Kobayashi, Y.; Hernandez-Pagan, E.; Hoertz, P.; Moore, T.; Moore, A.; Gust, D.; Mallouk, T. Photoassisted Overall Water Splitting in a Visible Light-Absorbing Dye-Sensitized Photoelectrochemical Cell. *J. Am. Chem. Soc.* **2009**, *131*, 926–927.

(123) Swierk, J. R.; McCool, N. S.; Saunders, T. P.; Barber, G. D.; Mallouk, T. E. Effects of Electron Trapping and Protonation on the Efficiency of Water-Splitting Dye-Sensitized Solar Cells. *J. Am. Chem. Soc.* **2014**, *136*, 10974–10982.

(124) Yang, H. Bin; Miao, J.; Hung, S.; Huo, F.; Chen, H. M.; Liu, B.; Engineering, B.; Drive, N.; Road, R.; Science, M.; et al. Stable Quantum Dot Photoelectrolysis Cell for Unassisted Visible Light Solar. **2014**.

(125) Abramo, J.; Garner, A.; Chapin, E. Ethylenically Unsaturated Aromatic Phosphorous Acid. 3,051,740, 1962.

(126) Gutierrez, A. J.; Prisbe, E. J.; Rohloff, J. C. DEALKYLATION OF PHOSPHONATE ESTERS WITH CHLOROTRIMEHTYLSILANE. *Nucleosides, Nucleotides and Nucleic Acids* **2001**, *20*, 1299–1302.

(127) Cirillo, M.; Aubert, T.; Gomes, R.; Van Deun, R.; Emplit, P.; Biermann, A.; Lange, H.; Thomsen, C.; Brainis, E.; Hens, Z. "Flash" Synthesis of CdSe/CdS Core–Shell Quantum Dots. *Chem. Mater.* **2014**, *26*, 1154–1160.

(128) Sachleben, J.; Wooten, E.; Emsley, L.; Pines, A.; Colvin, L.; Alivisatos, A. NMR Studies of the Surface Structure and Dynamics of Semiconductor Nanocrystals. *Chem. Phys. Lett.* **1992**, *198*, 431–436.

(129) Anderson, N. C.; Hendricks, M. P.; Choi, J. J.; Owen, J. S. Ligand Exchange and the Stoichiometry of Metal Chalcogenide Nanocrystals: Spectroscopic Observation of Facile Metal-Carboxylate Displacement and Binding. **2013**.

(130) Shen, Y.; Gee, M. Y.; Tan, R.; Pellechia, P. J.; Greytak, A. B. Purification of Quantum Dots by Gel Permeation Chromatography and the Effect of Excess Ligands on Shell Growth and Ligand Exchange. **2013**.

(131) Lapides, A. M.; Ashford, D. L.; Hanson, K.; Torelli, D. a; Templeton, J. L.; Meyer, T. J. Stabilization of a ruthenium(II) Polypyridyl Dye on Nanocrystalline TiO2 by an Electropolymerized Overlayer. *J. Am. Chem. Soc.* **2013**, *135*, 15450–15458.

(132) Lee, S.-H. A.; Zhao, Y.; Hernandez-Pagan, E. a.; Blasdel, L.; Youngblood, W. J.; Mallouk, T. E. Electron Transfer Kinetics in Water Splitting Dye-Sensitized Solar Cells Based on Core–shell Oxide Electrodes. *Faraday Discuss.* **2012**, *155*, 165.

(133) Yu, W.; Qu, L.; Guo, W.; Peng, X. Experimental Determination of the Extinction Coefficient of CdTe, CdSe, and CdS Nanocrystals. *Chem. Mater.* **2003**, *15*, 2854–2860.

(134) Lee, S.-H. A.; Abrams, N. M.; Hoertz, P. G.; Barber, G. D.; Halaoui, L. I.; Mallouk, T. E. Coupling of Titania Inverse Opals to Nanocrystalline Titania Layers in Dye-Sensitized Solar Cells. *J. Phys. Chem. B* **2008**, *112*, 14415–14421.

(135) ABRAMO, J.; CHAPIN, E. Chloromethylation of B-Chloroethylbenzene and the Preparation of P-Vinylbenzyl Alcohol1. *J. Org. Chem.* **1961**, *26*, 2671–2673.

(136) Wohler, L.; Witzmann, W. Die Oxyde Des Lridiums. *Z. Anorg. Chemie.* **1908**, *57*, 323–352.

(137) Nakagawa, T.; Beasley, C. A.; Murray, R. W. Efficient Electro-Oxidation of Water near Its Reversible Potential by a Mesoporous IrO X Nanoparticle Film. *J. Phys. Chem. Lett.* **2009**, 12958–12961.

(138) Flamee, S.; Cirillo, M.; Abe, S.; Nolf, K. De; Gomes, R.; Aubert, T. Fast, High Yield, and High Solid Loading Synthesis of Metal Selenide Nanocrystals. *Chem. Mater.* **2013**, *25*, 2476–2483.

(139) FLETCHER, R. F. K. and A. N. FLUORESCENCE QUANTUM YIELDS OF SOME RHODAMINE. *J. Lumin.* **1982**, *27*, 455–462.

(140) Li, Z.; Ji, Y.; Xie, R.; Grisham, S. Y.; Peng, X. Correlation of CdS Nanocrystal Formation with Elemental Sulfur Activation and Its Implication in Synthetic Development. *J. Am. Chem. Soc.* **2011**, *133*, 17248–17256.

(141) Rubel, M.; Haasch, R.; Mrozek, P.; Wieckowski, A.; De Pauli, C.; Trasatti, S. Characterization of IrO2 -SnO2 , Thin Layers by Electron and Ion Spectroscopies. *Vacuum* **1994**, *45*, 423–427.

(142) Silversmit, G.; De Doncker, G.; De Gryse, R. A Mineral TiO2 (001) Anatase Crystal Examined by XPS. *Surf. Sci. Spectra* **2002**, *9*, 21–29.